Slip/Jump Effects in Catalytic Reacting Flows in Microchannels

by

Azad Qazi Zade

A thesis
presented to the University of Waterloo
in fulfillment of the
thesis requirement for the degree of
Doctor of Philosophy
in
Mechanical Engineering

Waterloo, Ontario, Canada, 2012

AUTHOR'S DECLARATION

I hereby declare that I am the sole author of this thesis. This is a true copy of the thesis, including any required final revisions, as accepted by my examiners.

I understand that my thesis may be made electronically available to the public.

Abstract

In order to meet the increased power demand for micro–devices in almost every field of engineering, scaling down of conventional power supplies to micro–heat engines, micro fuel cells, micro–turbines and combustors has been proposed as an efficient, safe and reliable energy delivery method for Micro–Electro–Mechanical–Systems. Since homogeneous combustion cannot be sustained at a significant level in microchannels, catalytic walls are usually employed to enhance reactions. One of the complications in miniaturizing conventional power generators, however, is that the common continuum assumption can break down as the characteristic length scale of these devices approaches the molecular mean free path.

In this thesis, a general set of boundary conditions for reacting multicomponent gaseous flows is introduced to account for rarefaction effects in micro–reactors. These boundary conditions are derived from the kinetic theory of gases and are utilized to study non–equilibrium transport in reacting flows. A finite–volume code with detailed gas phase and surface reactions is developed to accommodate these boundary conditions. Next, the relative importance of the homogeneous reactions in microchannels is assessed by exploring the interaction between the gas phase and surface reactions under different operating conditions. Finally, the effects of velocity–slip, temperature–jump and concentration–jump on two different sets of catalytic reactive flows are explored; hydrogen oxidation on platinum and ammonia decomposition on ruthenium.

In order to identify the limiting values beyond which the gas phase reactions become negligible compared to surface reactions, the contribution of homogeneous reactions to hydrogen conversion in lean H_2/air mixtures has been investigated under three key operating parameters: different inlet mass fluxes, fuel–air equivalence ratios and channel heights.

Generally, as the channel height decreases, the relative importance of the homogeneous reactions compared to surface reactions becomes negligible. This effect become more pronounced in leaner mixtures. Numerical results also show that in catalytic reactive flows in microchannels, the thermal diffusion effects cannot be neglected especially in the entrance region where temperature gradients are strong. The velocity–slip, temperature–jump and concentration–jump boundary conditions have miscellaneous effects on flow, temperature and species concentration fields. It is shown that the velocity–slip boundary condition only slightly influences the species distribution at the edge of the Knudsen layer as well as inside the channel, while the temperature–jump boundary condition affects the heat and mass transfer characteristics the most. The concentration–jump effect, on the other hand, can counter balance the temperature–jump effects in some cases. Numerical results reveal that the presence of a temperature discontinuity at the wall is the main factor in defining the concentration jump at the edge of the Knudsen layer.

Acknowledgements

First and foremost I want to thank my advisors Professor Metin Renksizbulut and Professor Jacob Friedman, for their guidance and inspiration during my research and study. I appreciate all their contributions of time, ideas, and funding to make my PhD experience productive and stimulating. Metin has supported me academically and emotionally through the rough road to finish this thesis. And during the most difficult times when writing this thesis, he gave me the moral support and the freedom I needed to move on. Besides, I would also like to thank my defense committee, Professors Ioannis Chatzis, Cécile Devaud, and John Z. Wen, for their time, interest and insightful comments and suggestions which improved this thesis. I am grateful to Professor Nedjib Djilali who kindly accepted to be the external examiner of my thesis.

I would like to take this opportunity and thank my love, Sahba, whose kindness, patience and support enabled me to complete this work. Being with her makes me a better person and I certainly would have been a different person without her. My deepest gratitude goes to my family for their unflagging love and support throughout my life. They have cherished with me every great moment and supported me whenever I needed. This dissertation would simply be impossible without them. I cannot ask for more from my mother, Maryam, whom I have no suitable word that can fully describe her everlasting love to me. I love you mother. I feel lucky to have wonderful brothers, Shayan and Zaniar, who have been my closest friends in life. Their talent and accomplishments have always been a source of great pride and inspiration for me. Thanks to my father, whose memory has only increased after so many years of his death and was often in my thoughts on this journey – you are missed. This thesis is dedicated to his memory.

Getting through my dissertation required more than academic support, and I have

many friends to thank whom made my life enjoyable in Waterloo and became part of my life: Hamid Molavian, Samad Bazargan, Sattar Taheri-Araghi, Ahmad El Sayed, Pedram Hassanzadeh, Afshin Zamani, Amir Baserinia, Mohammad Niknam, Negar Ghahramani, Arash Tajik, and Poorya Ferdowsi. I am also thankful to Amir Ahmadzadegan for providing DSMC calculation results and also for the time we spent as officemates.

Finally, I would like to thank Natural Sciences and Engineering Research Council (NSERC) of Canada and Ontario Ministry of Education for their financial support.

Azad Qazi Zade
University of Waterloo
March 2012

Dedication

This thesis is dedicated to the memory of my father,
my love Sahba and my wonderful family for their constant support.

Table of Contents

List of Tables

List of Figures

Nomenclature

A_i	pre–exponential factor (Arrhenius parameter)
$a_{i0}, a_{i1}, b_{i0}, c_{i0}$	coefficients of expansion in Sonine polynomials
b_i	temperature exponent (Arrhenius parameter)
$c_{p,k}$	specific heat capacity of species k
D_h	hydraulic diameter
D_k^T	thermal diffusion coefficient
D_{kj}	tensor of ordinary diffusion coefficients
e^{int}	internal energy of molecule
E_a	activation energy
f_i	velocity distribution function of species i
H	channel height

h	mixture enthalpy
h_k	enthalpy of species k
$h^0_{f,k}$	standard enthalpy of formation
I	total number of gas phase reactions
$\mathbf{I}$	the identity tensor
$\mathbf{J}_k$	mass diffusion flux
k_B	Boltzmann constant
k_{fi}	forward reaction rate constant
k_{ri}	reverse reaction rate constant
Kn	Knudsen number
L	channel length
m_i	molecular mass of species i
$\dot{m}''_k$	total mass flux
N_g	total number of gas phase species
n_i	number density of species i
N_s	total number of surface species
$\hat{\mathbf{n}}$	normal vector
Nu	Nusselt number

p	pressure
Pe	Pećlet number
Pr	Prandtl number
$\mathbf{r}$	position vector
R	gas constant
$\dot{r}_k$	molar production rate of species k due to homogeneous reactions
Re	Reynolds number
$\dot{s}_k$	molar production rate of species k due to heterogeneous reactions
Sc	Schmidt number
T	temperature
$\mathbf{U}$	mass–averaged velocity vector
$\mathbf{V}$	total molecular velocity
$\mathbf{V}'$	peculiar (thermal) velocity
w_k	molar mass of species k
$\bar{w}$	mixture molar mass
x, y, z	cartesian coordinates
X_k	mole fraction of species k
$[X_k]$	molar concentration of species k

Y_k mass fraction of species k

Z_n surface site fraction of species n

Greek symbols

Γ total surface site density

γ_i sticking coefficient of the adsorption reaction "i"

$\bar{\gamma}$ specific heat ratio

λ thermal conductivity

μ viscosity

Φ viscous dissipation

φ equivalence ratio

ρ mixture density

σ_n number of surface sites occupied by surface species n

τ Newtonian stresses

θ_i accommodation coefficient

ξ number of terms in Sonine polynomials

ζ molecular mean free path

Subscripts and superscripts

c centerline

in	inlet conditions
out	outlet conditions
r	reference values
s	edge of the Knudsen layer
w	wall

Chapter 1

Introduction

Micro devices have gained significant popularity due to their applicability in various fields from cooling devices to drug delivery systems. In recent years there has been a push for miniaturizing the available mechanical and chemical processes in order to meet the increased demand for micro–devices in almost every field of engineering. Efficient delivery of sustainable, safe and cheap energy to Micro-Electro-Mechanical-Systems (MEMS) has become one of the most important and challenging issues as the current portable power sources fail to keep up with the rapid growth in the number of MEMS devices and their evolution into more capable, complex and power–hungry devices. Scaling down the conventional power supplies such as micro–heat engines, micro fuel cells, micro–turbines and combustors has been proposed to replace batteries due to their much higher energy density. Micro–power generating devices convert the stored chemical energy in fuels to mechanical or electrical power through electro/chemical reactions. Microreactors benefit from a range of inherent advantages. Due to their smaller size and high surface area to volume ratio, the rate of heat and mass transfer is much higher. They are also safer and due to their high

selectivity in chemical reactions, they generally can be designed to be more efficient and environmentally friendly. Miniaturizing these conventional power generators, however, is not simply achieved by reducing the physical size of their macro counterparts. Difficulties arise from modeling to manufacturing of these devices. Modeling such systems usually require special attention since new physical phenomena should be taken into account in sub–millimeter range. The current research is motivated by the challenges in modeling such systems as these microreactors become smaller and smaller. Basic flow, heat and mass transfer characteristics of such systems are yet to be explored to achieve reliable and efficient modeling of competent microreactor designs. The main objective of this research is to develop a numerical model for the simulation of rarefied catalytic reacting flows in microreactors. This work is a fundamental study and as such is relevant to almost all types of micro–devices which involve chemical reactions and the methodology can be adapted to the design process of a range of applications, such as chemical synthesis, micro–reformers, micro fuel cells, micro–propulsion and micro–Total–Analysis–Systems, to name a few.

One of the complications in dealing with micro–scale devices is that the common continuum assumption can break down as the characteristic length scale of these devices approaches the mean molecular free path. In such a case, the number of inter–molecular collisions decreases and eventually there comes a stage in which the number of collisions between molecules are rare compared to the number of collisions with the surrounding walls, in which case each molecule acts independently to bring forth the gas properties [49]. This makes the gas lose its intimate contact with solid bodies such that the gas slips over the surface, and in the case of heat or mass transfer, a temperature or concentration jump is observed between the surface and the adjacent gas layer. The continuum equations for mass, momentum and energy conservation are usually employed to study the motion of a fluid, in which the properties of the fluid at each point can be defined as an average of mi-

croscopic characteristics of the neighbouring points. The Knudsen number Kn, defined as the ratio of molecular mean–free–path to the characteristic length scale of the problem, can be used to estimate the applicability of the continuum equations in dealing with problems that involve very small length scales or rarefied gases. For certain values of the Knudsen number, the continuum equations cannot be applied directly and either they should be modified or molecular models should be employed. In the case of rarefied gas flow, it is known that for $\mathrm{Kn} < 0.001$ the continuum models are valid, and for $\mathrm{Kn} > 10$ the free–molecular models should be employed. In the mid range, neither continuum models nor free–molecular models are satisfactory and another classification is needed: slip–flow for the range $0.001 < \mathrm{Kn} < 0.1$ and transition–flow for the range $0.1 < \mathrm{Kn} < 10$ are considered to be appropriate descriptions [49]. Experimental, analytical and numerical studies have confirmed the applicability of the continuum equations along with proper slip/jump boundary conditions in the slip–flow range of Knudsen numbers, e.g., [4, 6, 7, 36, 42, 63, 67, 69, 92].

1.1 Research objectives

One of the principal objectives of this research is to develop a numerical scheme for the simulation of rarefied catalytic reacting flows in microreactors. As the channel size is reduced the slip/jump effects on the wall will become important in controlling the flow, heat and mass transfer properties of microreactors. Very few results have been reported for non–isothermal or reacting flows considering the slip/jump effects. The very few available numerical simulations of the reacting flows have either ignored the concentration–jump on the wall, or have used incomplete/inconsistent concentration–jump boundary conditions.

In the current work, first the concentration–jump, velocity–slip and temperature–jump boundary conditions for multicomponent reacting/non–reacting mixtures are derived based

on the kinetic theory of gases presenting a clear picture of the underlying principles [107]. In order for the model to be applicable to practical problems (i.e., polyatomic gas flows) correction terms are added to the temperature–jump boundary condition as well. A numerical scheme for the simulation of surface reactions with proper slip/jump boundary conditions coupled with homogeneous reactions in the gas phase is developed. It is usually assumed that below the so–called quenching distance, the homogeneous combustion cannot be sustained. In order to assess the interaction between the gas phase and catalytic reactions, contribution of the gas phase reactions to the overall hydrogen consumption in catalytic sub-millimetre channels is also investigated under different operating conditions [109]. The proposed set of boundary conditions are then verified for binary and multicomponent mixtures in a planar geometry by comparing different field variables with the predictions of the DSMC method [106]. Finally, the rarefaction effects on the catalytic reactive flows in microchannels are studied for two sets of reactions: oxidation of hydrogen on platinum and ammonia decomposition on ruthenium [110].

The developed numerical code is verified in different stages. A 3D extension of the code for compressible non–reacting flows in rectangular channels with first–order velocity–slip and temperature–jump boundary conditions is initially verified against the available analytical and numerical results [108]. In order to verify the numerical code for reacting flows a well–established reaction is chosen for the numerical validation, i.e. the catalytic oxidation of hydrogen on platinum. Hydrogen oxidation on platinum is a well–known reaction with reliable chemical kinetics data for numerical simulations. The experimental and numerical results of Appel *et* al. [3] are utilized as the benchmark for catalytic and homogeneous hydrogen combustion simulations. In their work, a range of chemical mechanisms for the surface and gas phase reactions are compared to their experimental results in a 7 mm high channel under different working conditions. Finally, the accuracy of the proposed

set of slip/jump boundary conditions for multicomponent gaseous flows are assessed by comparing the simulation results to the Direct Simulation Monte Carlo (DSMC) method predictions.

1.2 Review of the previous work

In this section, the previous works on catalytic microreactors, catalytic combustion of H_2/O_2 over platinum, catalytic ammonia decomposition, and rarefaction effects are briefly reviewed. A more comprehensive literature review is provided in the corresponding chapters. First, a general overview on microburners is presented followed by a brief summary of the catalytic combustion of H_2/O_2. Then the decomposition of ammonia on ruthenium in microchannels is discussed. Finally the slip/jump effects in reacting/non–reacting environments are examined.

1.2.1 Catalytic microburners

Due to high energy density of hydrocarbons compared to Lithium batteries and higher operational cycles, microburners have been studied in recent years as heat and energy sources for portable devices [2, 26, 61, 65, 66, 104]. The energy is either utilized by thermoelectrics for electric power generation or through endothermic reactions such as fossil fuel steam reforming or ammonia decomposition for hydrogen production for fuel cells. Scaling down the conventional combustion devices for creating microburners is one approach for creating microcombustors. However, due to thermal and radical quenching at the wall, flames will extinguish in gaps smaller than $1 \sim 2$ millimeters [26]. In order to reduce heat losses at the walls, some solutions have been proposed and tested such as

Swiss–Roll and Heat–Recirculating burners [2, 50]. Catalytic–wall burners could also be employed to enhance reactions. Catalytic combustion has been used as an efficient way to stabilize the combustion of fuels at lower temperatures in order to reduce NO_x emissions. Also, lower operating temperature increases the burner life and allows for a wider range of possible construction materials [3]. In catalytic burners, since the reactions mostly occur at the surface, the location of the heat source is fixed. Hence, combustor heat transfer design is simpler compared to gas phase combustion in which reaction zone locations may change in undesirable ways. Besides, microburners also benefit from increased transport rates due to small length scales which results in faster catalytic reactions compared to conventional large–scale devices. Understanding the surface phenomena and the interaction between homogeneous (gas phase) and heterogeneous (surface) reactions can be useful in the improvement of the catalytic combustion processes.

The catalytic combustion of fuels has been studied extensively in the past for different fuels to be utilized in monoliths as post–treatment devices [24, 32], but little work has been reported on catalytic microreactors. Recently, with rapid developments in micro–fabrication methods, researchers have studied the combustion of fuels in sub–millimeter structures. Veser et al. [96, 97] studied the high temperature catalytic combustion of hydrogen in microchannels with platinum catalyst introduced in the form of a wire. The homogeneous flame and explosion was reported to be effectively suppressed mainly due to radical quenching at the wall over a wide range of feed and reaction conditions. Norton et al. [75] proposed a simple fabrication protocol for the fabrication of a metal/ceramic microreactor with embedded thermocouples for catalytic combustion of hydrogen/oxygen mixtures over platinum. Although homogeneous flames have been observed in large conduits, no explosions were reported. In 250 μm gaps, no flames were observed. They also reported the effect of gap size on the contribution of gas and surface chemistries and

subsequently transport rates to arrive at the desired operation condition. Maruta et al. [60] numerically studied the extinction limits of methane/oxygen mixture over platinum in a non–adiabatic microtube of 1 mm in diameter, neglecting the gas phase reaction. In order to minimize the flame temperature in catalytic microcombustors, they suggest near–stoichiometric mixtures with exhaust gas recirculation rather than using lean mixtures. Norton and Vlachos [73, 74] conducted a two–dimensional CFD analysis to study the effects of channel dimension, wall thickness and thermal conductivity, operating conditions and external heat losses on the flame stability and combustion characteristics of methane/air and propane/air mixtures between two parallel plates. Hua et al. [43] simulated the gas phase reaction of premixed hydrogen/air mixture in a series of chambers ranging in dimension from millimeter to micrometer.

1.2.2 Catalytic combustion of H_2/O_2 over platinum

Catalytic combustion of several fuels such as CO, H_2 and CH_4 has been investigated experimentally and numerically for different purposes [3, 23]. Among those, hydrogen has gained popularity due to a number of reasons such as relatively simple chemical kinetics and hydrogen–assisted catalytically stabilized combustion. Also, the study of hydrogen oxidation is useful for fundamental research on the interaction of gas–phase and surface reactions since it has a fast reaction rate and reliable detailed chemical mechanisms are available. Catalytic combustion of hydrogen/oxygen mixtures over platinum in different geometries has been investigated by many researchers, both numerically and experimentally, such as Warnatz et al. [101], Deutschmann et al. [22, 23], Behrendt et al. [5], Appel et al. [3], Rinnemo et al. [83], to name a few.

The catalytic combustion of hydrogen in micro–structured openings has also been in-

vestigated. Aghalayam et al. [1] numerically investigated the role of wall quenching of radicals on the extinction behavior of hydrogen/air mixtures in a stagnation–point geometry. It was proposed that in general, radical quenching on the wall hinders homogeneous reactions; However, the heat release due to the catalytic surface reactions can reduce this effect. Boyarko et al. [12] studied the catalyzed combustion of hydrogen in 0.8 mm and 0.4 mm tubes both numerically and experimentally. The diameters of microtubes in their studies are reported to be below the quenching diameter for rich H_2/O_2 mixtures. They have used a plug–flow model in their simulations and have reported the critical values of imposed wall heat flux, minimum temperature and mixture ratios to initiate catalytic ignition. Gorke et al. [34] proposed a microreactor for hydrogen oxidation with integrated cooling passages in order to control the temperature and conversion rate. Norton et al. [75] experimentally studied the effect of confinement on the combustion of hydrogen and dominant chemistry mechanisms in microchannels. In the case of near–stoichiometric mixtures of hydrogen/air, they found evidence of homogeneous combustion in the 1000 μm channel but not in the 250 μm channel.

1.2.3 Ammonia decomposition

The push towards reducing emission levels from hydrocarbon combustion has resulted in an interest in hydrogen production to power fuel cells. To avoid anode catalyst poisoning in Proton Exchange Membrane Fuel Cells (PEMFC), the hydrogen feed should be carbon monoxide free (less than 50 ppm). Conventional steam reforming and water gas-shift reactions could be employed to produce carbon-monoxide-free hydrogen from hydrocarbons in industrial scales. However, the process costs as well as transportation and storage costs make the on–site production of hydrogen an attractive option for hydrogen supply

of fuel cells. Also, CO and CO_2 are known greenhouse gases and this approach to hydrogen production would undermine the greenhouse–free emission of fuel cells. The on–board production of hydrogen from hydrocarbons basically requires a scale–down of a chemical plant which involves a lot of processes for production of a carbon monoxide–free hydrogen feed. Therefore, hydrogen production from a single step process such as ammonia decomposition, which is carbon free (not considering the production process), is quite attractive for hydrogen production especially in small scale devices. Ammonia has been produced and stored in liquid form for a long time and issues about production, transportation, handling and storage are well established. Although even small traces (as low as 13 ppm) of ammonia can degrade PEM fuel cell performance, it is shown that the platinum catalyst of the fuel cell is not poisoned by ammonia; but rather the decrease in performance is because H^+ ions are replaced by NH_4^+ within the fuel cell anode catalyst layer. Other experiments show that poisoning and recovery rates with NH_3 are much slower than with CO [93]. Also, higher purity of available commercial ammonia makes it a better candidate for hydrogen production compared to methanol [19]. Therefore, the availability, relatively easy decomposition with no need for added oxygen or steam and narrow explosion limits make ammonia a good candidate as a hydrogen carrier especially for portable devices.

Different metals have been used as catalyst for ammonia decomposition. Papapolymerou et al. [77] compared ammonia decomposition activity for different metal wires. It was shown that iridium wires are more active than platinum and palladium. The most active catalyst for ammonia decomposition, however, is reported to be ruthenium [30, 28, 64, 91]. However, since Ru is expensive, nickel–based catalysts prove to be attractive alternatives as far as the cost is concerned and have received much attention in the past [104, 99]. The activation energy of the ammonia decomposition reaction depends highly on catalyst material and whether there is a metal support or the catalyst is pure

(in the form of single crystal, thin film or wire), with generally higher activities (lower activation energy) reported for catalysts on metal supports [18].

Catalytic decomposition of ammonia has been studied mainly for enhancing the understanding of the ammonia synthesis process. But recently, the hydrogen production from ammonia decomposition has been investigated. Chellappa et al. [17] studied ammonia decomposition kinetics at high temperatures and high ammonia concentration, and reported different kinetics compared to those reported for low concentration ammonia. They proposed a first–order rate expression for ammonia decomposition on Ni–Pt/Al_2O_3. Chein et al. [16] numerically simulated the ammonia decomposition in a cylindrical 2D reactor packed with Ni–Pt/Al_2O_3 particles, studying mainly the effects of volumetric ammonia feed rate and reaction temperature. Di Carlo et al. [14] proposed the utilization of Catalytic Membrane Reactors (CMR) for hydrogen production from ammonia and numerically studied the effect of different operating conditions. In these reactors, the membrane improves ammonia decomposition by immediately removing the produced hydrogen as well as providing hydrogen with high purity, suitable for fuel cell applications. In order to increase the hydrogen permeation through the membrane the reactor is operated at high pressure (10 bar), despite the favourable ammonia decomposition at lower pressures.

Small hydrogen generating devices have been developed and tested in recent years to meet the needs for on–site production of hydrogen for portable devices [28, 29, 88]. Different catalysts and metal supports have been proposed and examined for hydrogen production. In these experiments the ammonia conversion rate has been measured for different geometries and operational conditions. The underlying detailed chemical kinetics of ammonia decomposition on different catalytic surfaces, however, is not well documented yet. Few studies have reported elementary reactions for ammonia decomposition and usually the global rate of reaction (one step) is presented for ammonia decomposition. Deshmukh et

al. [21] presented a detailed microkinetic model for describing surface chemistry of ammonia decomposition on Ru. Based on the microkinetic model, they used a reduced rate expression for numerical simulation of the experiment carried out by Ganley et al. [29]. In the current research this set of elementary reactions will be used for numerical simulation of ammonia decomposition on ruthenium.

1.3 Slip/Jump boundary conditions

As indicated earlier, as the characteristic length scale of the problem approaches the mean molecular free path, i.e., micro flows, fluid flow cannot be described by the Navier–Stokes equations within the Knudsen layer at the vicinity of the wall, which is of the order of 1 molecular mean–free–path in thickness. The presence of gradients coupled with rarefied conditions causes the velocity distribution function to deviate from the equilibrium distribution significantly. Ideally, the Boltzmann equation, which is computationally very expensive to solve, should be solved in the Knudsen layer and matched with the solution of the Navier-Stokes equations in the bulk flow region. However, without solving the Boltzmann equation, it is possible to find an approximate Navier-Stokes solution by using suitable slip conditions [27, 35, 41, 87]. The first velocity–slip model to address this issue was proposed by Maxwell, who derived a velocity–slip equation based on a Taylor series expansion retaining terms up to first order. Some other arbitrary extensions to this model have been proposed by others involving higher order or non–linear Kn terms [46].

The effects of velocity–slip and temperature–jump on flow and heat transfer characteristics of non–reacting flows have been extensively studied [68, 81, 95, 105]. However, there exists very limited work on non–equilibrium transport in reacting flows and it still remains to be studied in–depth. In the case of multi–species transport, another important effect

analogous to the temperature–jump should be taken into account, i.e., the concentration–jump. The investigation of the concentration–jump was initially performed by Kramers et al. [51] based on the work of Maxwell on velocity–slip and temperature–jump. The concentration-jump not only affects the rate of reaction and local species concentration, but also the velocity–slip and temperature–jump in both reacting and non–reacting systems. The catalytic surface reaction is also affected by the temperature discontinuity at the wall due to strong temperature dependence of the chemical kinetics rates. Many rate–limiting adsorption/desorption reactions are very sensitive to local temperatures and hence the proper modeling and computation of temperature along with the local species concentration is vital for an accurate prediction of the behavior of such systems. Therefore, all of these non–equilibrium effects should be considered simultaneously in the simulation of microreactors. The coupling is even more pronounced in catalytic reactions since all the reactions take place on the wall. The effect of temperature–jump on the performance of reactive systems was investigated and verified experimentally by Shankar and Glumac [85] using low–pressure catalytic combustion systems. The concentration–jump phenomenon has been detected in simulations of reacting gas mixtures by Bird [10] and Papadopoulos and Rosner [76].

There is very limited work on the concentration jump and its effects on catalytic reactions and the available literature has mainly focused on the temperature jump and velocity slip effects. Raimondeau et al. [79] employed a parabolic numerical scheme to study the flame propagation of methane/air mixtures in tubular microchannels with no wall reactions. The effects of radical quenching and temperature discontinuity on the gas phase reactions were mainly emphasized in their work. Xu and Ju [102, 103] derived a concentration slip model and investigated the rarefaction effects on the rate of catalytic reactions in the numerical modeling of hydrogen and methane oxidation. In their work, they considered

the combustion of premixed stoichiometric mixtures at very low pressures ranging from 100 Pa to 0.2 atm. The velocity slip and temperature discontinuity at the wall were modeled using the conventional mixture–averaged boundary conditions. Li *et* al. [56, 57] compared the effects of different operating conditions on the flame temperature of methane/air and hydrogen/air mixtures. They also studied the effects of first order velocity slip and temperature jump boundary conditions on the flame temperature. They reported negligible slip/jump effects at low velocities and large channels ($d = 1$ mm) and a considerable temperature discontinuity at the wall close to the flame region due to high radial gradients. More recently, Rahaghi et al. [78] numerically studied the effect of different operating conditions on the performance of micro–combustors down to 600 μm. They also studied the velocity slip effect (first order) on the temperature and species mass fraction profiles and reported its impact to be negligible for these channel heights. In the current thesis, the concentration–jump, velocity–slip and temperature–jump boundary conditions, derived by Qazi Zade et al. [107], for multi–component gaseous reacting mixtures will be employed.

1.4 Outline of the thesis

The first chapter of this thesis is an introduction detailing the motivation and the goals of this work. The Introduction chapter includes a brief overview on the microreactor technology, its importance in the MEMS industry and challenges in modelling such systems.

In the second chapter, a mathematical description for modeling 2D micro–reactors is presented. The general Navier–Stokes, energy and species continuity equations are employed to represent the flow, temperature and species concentration fields within the channel. Chemical kinetics of the catalytic wall reactions and their interaction with the field variables are discussed in this section. The derivation of multicomponent velocity–slip,

temperature–jump and concentration–jump boundary conditions on catalytically reacting surfaces based on the kinetic theory of gases is also presented in this chapter.

The third chapter is devoted to the numerical implementation of the problem in hand. The details on the numerical treatment as well as code verification in three different stages are discussed in this chapter. A 3D extension of the code is also utilized to study the compressibility effects in rectangular microchannels in the slip regime. A general colocated finite volume formulation for the solution of mass, momentum and transport equations is presented in Appendix A.

In the fourth chapter, a parametric study is carried out to identify the relative importance of homogeneous reactions in sub–millimetre channels. To this end, the effects of different inlet mass fluxes, equivalence ratios and channel heights are studied to analyze the relative importance of gas phase and surface reactions for lean H_2/air mixtures in planar microchannels. Detailed gas phase and surface reaction mechanism are employed in the simulations.

In chapter five, the effects of velocity–slip, temperature–jump and concentration–jump on catalytic reactions are examined. Two distinct sets of reactions are analyzed in this chapter; hydrogen oxidation on platinum, and ammonia decomposition on ruthenium. Following the findings in chapter four, the gas phase reactions are ignored due to very small channel heights. The rarefaction effects are studied under different operating conditions: wall temperature, channel height, inlet mass flux and surface accommodation coefficients are varied to examine their individual effects.

In the last chapter, conclusions are presented and potential projects are proposed for future consideration.

Chapter 2

Mathematical description

In this chapter, the governing equations for steady laminar flow, heat and mass transfer in reacting gaseous flows are presented. Based on the kinetic theory of gases, a complete set of slip/jump boundary conditions for reacting gaseous flows are also derived. These conservation equations along with proper slip/jump boundary equations are solved numerically considering detailed gas phase and surface reaction mechanisms.

2.1 Governing equations

The governing mass, momentum, energy, and species continuity equations for a steady, laminar, reacting gas flow are:

$$\nabla \cdot (\rho \mathbf{U}) = 0 \tag{2.1}$$

$$\nabla \cdot (\rho \mathbf{U}\mathbf{U}) = -\nabla p + \nabla \cdot \left[\mu \left(\nabla \mathbf{U} + \nabla \mathbf{U}^T \right) - \frac{2}{3} \mu \left(\nabla \cdot \mathbf{U} \right) \mathbf{I} \right] \tag{2.2}$$

$$\nabla \cdot (\rho \mathbf{U} h) = -\nabla \cdot \left(-\lambda \nabla T + \sum_{k=1}^{N_g} h_k \mathbf{J}_k \right) + \Phi \tag{2.3}$$

$$\nabla \cdot (\rho \mathbf{U} Y_k) = -\nabla \cdot \mathbf{J}_k + w_k \dot{r_k} \tag{2.4}$$

Here, ρ is the mixture density, $\mathbf{U}$ is the mass–averaged velocity vector, p and μ are pressure and viscosity, $\mathbf{I}$ is the identity tensor, λ is the thermal conductivity, Φ is the viscous dissipation term, N_g is the total number of gas phase species, $\mathbf{J}_k$ is the mass diffusion flux, Y_k is the mass fraction, $c_{p,k}$ is the specific heat capacity, $\dot{r_k}$ is the molar production rate due to homogeneous reaction and w_k is the molar mass of species k. In this formulation the enthalpy of the k^{th} species h_k and the mixture enthalpy h are defined as:

$$h_k = h_{f,k}^0 + \int_{T_0}^{T} c_{p,k} \, dT \qquad ; \qquad h = \sum_{k=1}^{N_g} h_k Y_k \tag{2.5}$$

in which $h_{f,k}^0$ is the standard enthalpy of formation. The mass fractions and diffusion fluxes of all species are governed by:

$$\sum_{k=1}^{N_g} Y_k = 1 \qquad ; \qquad \sum_{k=1}^{N_g} \mathbf{J}_k \cdot \hat{\mathbf{n}} = 0 \tag{2.6}$$

The species diffusion mass flux $\mathbf{J}_k$ is determined using the multi–component diffusion equation as [11, 41]:

$$\mathbf{J}_k = \frac{\rho w_k}{\bar{w}^2} \sum_{j=1}^{N_g} w_j D_{kj} \nabla X_j - D_k^T \frac{1}{T} \nabla T \tag{2.7}$$

In this equation, X_k is the mole fraction of species k, $\bar{w}$ is the mixture molar mass, D_{kj} is the tensor of ordinary diffusion coefficients, and D_k^T are the thermal diffusion coefficients.

2.1.1 Chemical kinetics

The homogeneous production rates in the conservation equations are modeled using detailed gas phase reaction mechanisms. Depending on the problem in hand, appropriate reaction mechanisms will be adopted in the following sections.

The molar production rate of each species in the gas phase can be written in terms of the summation of progress rates of all reactions involving species k as:

$$\dot{r}_k = \sum_{i=1}^{I} v_{ki} \dot{q}_i \qquad\qquad k = 1, 2, \ldots, N_g \tag{2.8}$$

where I is the total number of gas phase reactions, $v_{ki} = v''_{ki} - v'_{ki}$ with v'_{ki} and v''_{ki} being the left hand side and right hand side stoichiometric coefficients of the k^{th} species in reaction "i", respectively. The progress rate $\dot{q}_i$ of each reaction is given by:

$$\dot{q}_i = k_{fi} \prod_{j=1}^{N_g} [X_j]^{v'_{ji}} - k_{ri} \prod_{j=1}^{N_g} [X_j]^{v''_{ji}} \tag{2.9}$$

where k_{fi} and k_{ri} are the forward and reverse reaction rate constants, respectively, and $[X_k] = \rho X_k / \bar{w}$ is the molar concentration of the k^{th} species. Unless otherwise specified, the forward reaction rate constants are assumed to have the Arrhenius temperature dependence as:

$$k_{fi} = A_i T^{b_i} \exp\left(\frac{-E_i}{RT}\right) \tag{2.10}$$

where A_i is the pre–exponential factor, b_i is the temperature exponent, and E_i is the activation energy of reaction "i". For each reaction, the reverse rate constant is calculated using the equilibrium constant.

The production rate of both gas and surface species on the wall are governed by similar equations. It should be noted that, following Coltrin *et* al. [20], the molar concentration of surface species are defined as:

$$[X_n] = \frac{Z_n \Gamma}{\sigma_n} \qquad\qquad n = 1, 2, \ldots, N_s \tag{2.11}$$

where Z_n and σ_n are the surface species site fraction and the number of surface sites occupied by the n^{th} surface species, N_s is the total number of surface species, and Γ is the total surface site density. The site occupancy number of species "n" represents the number of sites that each species occupies, since large molecules might occupy more than one site. Consider, for instance, the deposition of SiH_2 and Si_2H_4 on a silicon surface as depicted in Fig. 2.1. The surface initially consists of 32 open sites. One of the sites is occupied by SiH_2 with occupancy number $\sigma_n = 1$ and two other sites are occupied by Si_2H_4 having an occupancy number of $\sigma_n = 2$. Therefore the site fraction of open sites in this example would be equal to $Z_{\text{Si}} = 29/32 = 0.906$.

In the case of gas phase species adsorption reactions on the wall (e.g., reactions S1–S6 in Table 4.2), the reaction rate constants are calculated using the sticking coefficients as [20]:

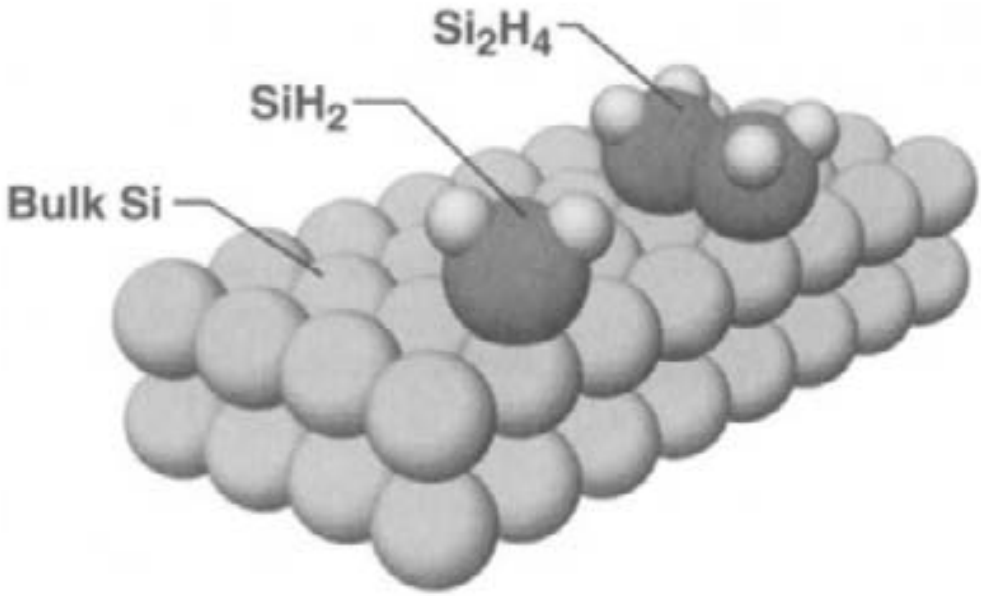

Figure 2.1: Schematic representation of surface species and open sites [48].

$$k_{ads,i} = \frac{\gamma_i}{1 - \gamma_i Z_{\mathrm{Pt}}/2} \left(\frac{1}{\Gamma^m}\right) \sqrt{\frac{RT}{2\pi w_k}} \tag{2.12}$$

where $k_{ads,i}$ and γ_i are the rate constant and sticking coefficient of the adsorption reaction "i" involving species "k", and m is the sum of surface species stoichiometric coefficients on the left hand side of adsorption reactions. The correction factor embedded in this equation in the form of the free platinum surface site fraction Z_{Pt} is important in reactions involving species with large sticking coefficients and surfaces with low free site availability [3].

2.2 Boundary conditions[1]

In this section, first a complete set of slip/jump boundary conditions, based on the kinetic theory of gases, are derived. Following the derivation of proper boundary conditions, their numerical implementation will also be discussed.

2.2.1 Slip/Jump boundary conditions

In this section, general slip/jump boundary conditions are derived for velocity, temperature and concentration in a multicomponent gas flow on a catalytic surface following Grads method [35]. In order for the model to be applicable to practical problems (i.e., polyatomic gas flows) correction terms are added to the temperature–jump boundary condition as well. A clear picture of the underlying principles and assumptions in the complex derivation of slip/jump boundary conditions are presented so that they can be well understood and properly simplified in practical engineering problems.

Slip Model

In order to avoid the complexity of solving the Boltzmann equation in rarefied gas flows, in the slip–flow regime one can assign imaginary velocity, temperature and concentration values (slip/jump values) at the boundary so that the standard continuum equations can still be employed safely outside the Knudsen layer [15, 27, 41, 49, 87]. The macroscopic properties of the gas can be obtained if the velocity distribution of the molecules f is known.

[1] A brief version of this section is published as an article in the International Journal of Heat and Mass Transfer, 2008, Vol. 51, No. 21-22, 5063-5071

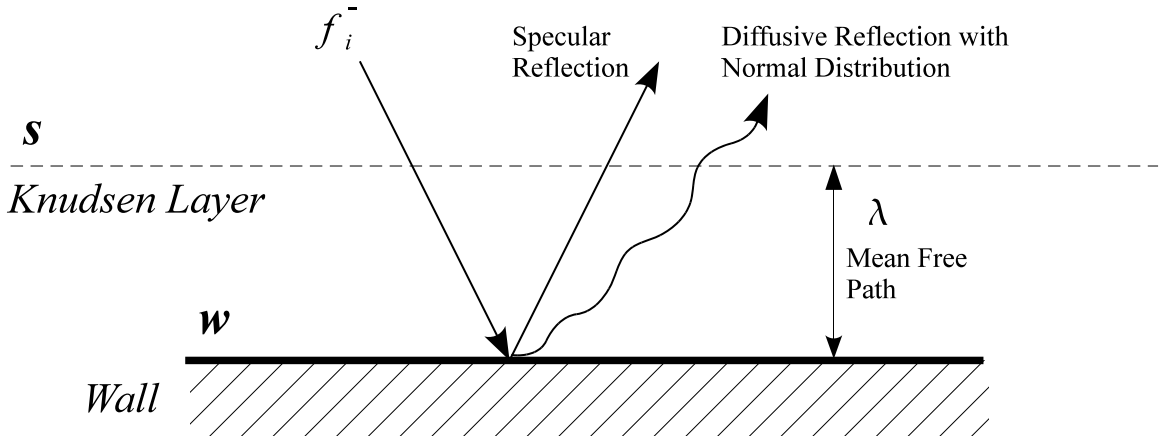

Figure 2.2: Schematic of a generic molecule impinging on the wall and possible velocity distribution before and after collision.

Consider a wall with gas molecules impinging on it where catalytic reactions could also take place, as shown in Fig. 2.2. In order to derive the slip boundary conditions, the velocity distribution function for wall–reflected molecules f^+ should be specified provided that the incident distribution f^- is given. The most commonly used reflection model is the so–called specular–diffusive model which, assuming the boundary is perpendicular to the y direction, can be written as [35]:

$$\begin{aligned} f_i^+\left(V_{ix}, V_{iy}, V_{iz}\right) &= \left(1-\theta_i\right) f_i^-\left(V_{ix}, -V_{iy}, V_{iz}\right) + \\ &\quad \left(\theta_i - \gamma_i\right) \frac{n_{i,w}}{\left(\dfrac{2\pi k_B T_w}{m_i}\right)^{3/2}} \exp\left(-\frac{V_i^2}{2k_B T_w/m_i}\right) \qquad V_{iy} > 0 \end{aligned} \tag{2.13}$$

where T_w is the wall temperature, θ_i is the accommodation coefficient and γ_i is the re-

combination (sticking) coefficient, which represents the probability of appearance ($\gamma_i < 0$) or disappearance ($\gamma_i > 0$) of species "i" at the surface due to chemical reactions. This expression states that a certain fraction $(1-\theta_i)$ of the incident molecules are specularly reflected by the wall (without reaching the equilibrium state), while the remaining molecules are captured by the wall and are either consumed (or produced) or re–emitted with an equilibrium distribution at the prevailing wall temperature. It is important to note that $n_{i,w}$ is defined as the wall number density *prior* to chemical reactions on the catalytic surface. Thus, double–accounting of the reaction effects through both γ_i and $n_{i,w}$ in Eq. (2.13) is avoided. This definition of number density is also appropriate for determining the rate of production (or consumption) of species at the wall, since it represents the reactant concentration required for a typical catalytic reaction rate expression, as will be shown later.

In order to be consistent with the approximation level associated with the Navier–Stokes equations, the velocity distribution function near the wall can be described by the first–order accurate Chapman–Enskog distribution function [15]. To this approximation, the velocity distribution function for each species "i" in a non–uniform multicomponent mixture can be written as:

$$f_i\left(V_{ix}, V_{iy}, V_{iz}\right) = f_i^M\left(1+\Phi_i\right) \tag{2.14a}$$

$$f_i^M\left(V_{ix}, V_{iy}, V_{iz}\right) = \frac{n_i}{\left(\dfrac{2\pi k_B T}{m_i}\right)^{3/2}} \exp\left(-\frac{V_i'^2}{\frac{2\pi k_B T}{m_i}}\right) \tag{2.14b}$$

where f_i^M is the Maxwellian distribution function, n_i and m_i are the number density and molecular mass of species "i", T is the temperature, k_B is the Boltzmann constant

and $\mathbf{V}_i^{'} = \mathbf{V}_i - \mathbf{U}$ is the peculiar (or thermal) velocity of the gas molecules with $\mathbf{V}_i$ and $\mathbf{U}$ being the molecular velocity and mass–averaged gas velocity, respectively. The normalized perturbation to the equilibrium distribution Φ_i corresponds to the Navier–Stokes approximation in the solution of the Boltzmann equation. Using the Chapman–Enskog method to first–order approximation, Φ_i is given by [15]:

$$\begin{aligned}\Phi_i &= -\left[a_{i0} + a_{i1}\left(\frac{5}{2} - \frac{m_i V_i^{'2}}{2k_B T}\right)\right]\left(\mathbf{V}_i^{'} \cdot \frac{\partial \ln T}{\partial \mathbf{r}}\right) - \\ &\quad \frac{m_i}{2k_B T}\left[\left(\mathbf{V}_i^{'}\mathbf{V}_i^{'} - \frac{1}{3}V_i^{'2}\mathbf{I}\right) : \frac{\partial \mathbf{U}}{\partial \mathbf{r}}\right] b_{i0} + n\sqrt{\frac{m_i}{2k_B T}}\sum_{j=1}^{N_g} c_{i0}^{j}\mathbf{V}_i^{'} \cdot \mathbf{d}_j \qquad (2.15)\end{aligned}$$

where $a_{i0}, a_{i1}, b_{i0},$ and c_{i0}^{j} are coefficients of expansion in the Sonine polynomials which will be discussed later, $\mathbf{r}$ is the position vector, $\mathbf{I}$ is the identity tensor, and $\mathbf{d}_j$ is the diffusive mass flux of species j given by [41]:

$$\mathbf{d}_j = \nabla\left(\frac{n_j}{n}\right) + \left(\frac{n_j}{n} - \frac{n_j m_j}{\rho}\right)\nabla \ln p - \frac{n_j m_j}{p}\left(\mathbf{X}_j - \frac{1}{\rho}\sum_{k=1}^{N_g} n_k m_k \mathbf{X}_k\right) \qquad (2.16)$$

where $\mathbf{X}_j$ is the body force acting on species j.

Concentration–jump In order to derive the concentration–jump boundary condition, the net mass flux of each species normal to the boundary is determined as:

$$F_i = \int_{-\infty}^{+\infty}\int_{0}^{+\infty}\int_{-\infty}^{+\infty} m_i V_{iy}\left[f_i^{+}\left(V_{ix}, V_{iy}, V_{iz}\right) - f_i^{-}\left(V_{ix}, -V_{iy}, V_{iz}\right)\right] d\mathbf{V} \qquad (2.17)$$

On the other hand, the net mass flux of each species normal to the wall can be written in terms of macroscopic properties as [41]:

$$F_i = \frac{m_i n_{i,s}}{2}\left(\frac{2k_B T_s}{m_i}\right)^{1/2}\left(-a_{i0}\frac{\partial \ln T}{\partial y} + n\sum_{j=1}^{N_g} c_{i0}^{j} d_{jy}\right)_s \tag{2.18}$$

where d_{jy} is the y component of the diffusion flux of species j (see Eq. (2.16)). Equating these two equations and calculating the integrals involved results in the following concentration–jump boundary condition:

$$\begin{aligned}\frac{n_{i,w}}{n_{i,s}}\left(\frac{T_w}{T_s}\right)^{1/2} &= \frac{\theta_i}{\theta_i-\gamma_i}\left[1+\frac{b_{i0}}{6}\left(\frac{\partial U_x}{\partial x}+\frac{\partial U_z}{\partial z}-2\frac{\partial U_y}{\partial y}\right)\right]_s + \\ &\quad \frac{(2-\theta_i)\sqrt{\pi}}{2(\theta_i-\gamma_i)}\left(-a_{i0}\frac{\partial \ln T}{\partial y}+n\sum_{j=1}^{N_g} c_{i0}^{j} d_{jy}\right)_s\end{aligned} \tag{2.19}$$

It should be noted that the above equation is not an explicit expression for $n_{i,s}$ because the coefficients a_{i0} and c_{i0}^{j} are functions of $n_{i,s}$. Explicit expressions for $n_{i,s}$ can be obtained by specifying the surface reaction rate, which will be discussed for special cases in successive sections.

Velocity–slip In order to arrive at the velocity–slip boundary condition, one can multiply Eq. (2.13) by $m_i V_{ix}^{'} V_{iy}^{'} = m_i(V_{ix}-U_x)V_{iy}$ and integrate to obtain:

$$S_{i,xy}^{+} + (1-\theta_i)\, S_{i,xy}^{-} + (\theta_i-\gamma_i)\, U_x n_{i,w} m_i \sqrt{\frac{k_B T_w}{2\pi m_i}} = 0 \tag{2.20}$$

where

$$S_{i,xy}^{\pm} = \pm \int_{-\infty}^{+\infty} dV_{ix} \int_{-\infty}^{+\infty} dV_{iz} \int_{0}^{+\infty} m_i V_{ix}^{'} V_{iy}^{'} f_i^{\pm} \left(V_{ix}, \pm V_{iy}, V_{iz}\right) \, dV_{iy} \tag{2.21}$$

Integrating the above equation using Eqs. (2.14) and (2.15) yields:

$$\begin{aligned} S_{i,xy}^{\pm} &= \pm \frac{n_{i,s} k_B}{4\sqrt{\pi}} \left(a_{i1} - 2a_{i0}\right) \left(\frac{\partial T}{\partial x}\right)_s - \frac{n_{i,s} k_B T_s}{4} b_{i0} \left(\frac{\partial U_x}{\partial y} + \frac{\partial U_y}{\partial x}\right)_s \\ &\pm \left(\frac{n n_{i,s} k_B T_s}{2\sqrt{\pi}} \sum_{j=1}^{N_g} c_{i0}^{j} d_{jx}\right)_s \end{aligned} \tag{2.22}$$

Substituting this in Eq. (2.20) and summing over all species, the following velocity–slip expression is obtained:

$$U_x = \frac{\sum_{i=1}^{N_g} n_{i,s} \sqrt{\frac{k_B T_s}{2}} \left[\theta_i \left(\left(a_{i0} - \frac{a_{i1}}{2}\right) \frac{\partial \ln T}{\partial x} - \mathcal{A}_1\right) + \left(2 - \theta_i\right) \mathcal{A}_3\right]_s}{\sum_{i=1}^{N_g} n_{i,s} \sqrt{m_i} \left[\theta_i \left(1 + \mathcal{A}_4\right) + \frac{(2-\theta_i)\sqrt{\pi}}{2} \left(\mathcal{A}_2 - a_{i0} \frac{\partial \ln T}{\partial y}\right)\right]_s} \tag{2.23}$$

In this equation the wall number density $n_{i,w}$ is substituted from Eq. (2.19) and,

$$\mathcal{A}_1 = n \sum_{j=1}^{N_g} c_{i0}^{j} d_{jx} \tag{2.24a}$$

$$\mathcal{A}_2 = n \sum_{j=1}^{N_g} c_{i0}^{j} d_{jy} \tag{2.24b}$$

$$\mathcal{A}_3 = \sqrt{\pi} \frac{b_{i0}}{2} \left(\frac{\partial U_x}{\partial y} + \frac{\partial U_y}{\partial x}\right) \tag{2.24c}$$

$$\mathcal{A}_4 = \frac{b_{i0}}{6} \left(\frac{\partial U_x}{\partial x} + \frac{\partial U_z}{\partial z} - 2\frac{\partial U_y}{\partial y}\right) \tag{2.24d}$$

Note that in order to arrive at the above relation for velocity-slip in the x direction, Eq. (2.13) was multiplied by $m_i(V_{ix} - U_x)V_{iy}$. In the same manner, one can multiply Eq. (2.13) by $m_i(V_{iz} - U_z)V_{iy}$ and follow the same steps to arrive at a velocity-slip boundary condition U_z in the z direction

Temperature–jump In order to proceed with the temperature–jump boundary condition, Eq. (2.13) is multiplied by $m_i V_{iy}^{'} V_i^{'2} = m_i V_{iy}(V_i^2 - 2\mathbf{V}_i \cdot \mathbf{U} + U^2)$ and integrated to obtain:

$$h_{i,y}^{+} + (1 - \theta_i)\, h_{i,y}^{-} = (\theta_i - \gamma_i)\, h_{i,y}^{M} \tag{2.25}$$

where

$$h_{i,y}^{\pm} = \pm \int_{-\infty}^{+\infty} dV_{ix} \int_{-\infty}^{+\infty} dV_{iz} \int_{0}^{+\infty} m_i V_{iy}^{'} V_i^{'2} f_i^{\pm}\left(V_{ix}, \pm V_{iy}, V_{iz}\right)\, dV_{iy} \tag{2.26}$$

and

$$h_{i,y}^{M} = \pm \int_{-\infty}^{+\infty} dV_{ix} \int_{-\infty}^{+\infty} dV_{iz} \int_{0}^{+\infty} m_i V_{iy}^{'} V_i^{'2} f_i^{M}\left(V_{ix}, V_{iy}, V_{iz}\right)\, dV_{iy} \tag{2.27}$$

Performing the integrations in the above equations yields:

$$\begin{aligned} h_{i,y}^{\pm} = \;& \pm \frac{n_{i,s} m_i}{\sqrt{\pi}} \left(\frac{2k_B T_s}{m_i}\right)^{3/2} + 5 n_{i,s} m_i \left(\frac{k_B T_s}{2m_i}\right)^{3/2} (a_{i1} - a_{i0}) \frac{\partial \ln T}{\partial y} \\ & \pm \frac{n_{i,s} m_i}{4\sqrt{\pi}} \left(\frac{2k_B T_s}{m_i}\right) b_{i0} \left(\frac{\partial U_x}{\partial x} + \frac{\partial U_z}{\partial z} - 2\frac{\partial U_y}{\partial y}\right)_s \\ & + \left(5 n n_{i,s} m_i \left(\frac{k_B T_s}{2m_i}\right)^{3/2} \sum_{j=1}^{N_g} c_{i0}^{j} d_{jy}\right)_s \end{aligned} \tag{2.28}$$

and

$$h_{i,y}^{M} = n_{i,w} m_i U^2 \sqrt{\frac{k_B T_w}{2\pi m_i}} + \frac{n_{i,w} m_i}{\sqrt{\pi}} \left(\frac{2 k_B T_w}{m_i} \right)^{3/2} \tag{2.29}$$

These expressions account only for the translational energy of molecules and do not include the internal (rotational and vibrational) energy of the incident and reflected molecules, which becomes important in the case of polyatomic gases. In order to include the internal energy of molecules, one can simply multiply the number flux N_i of incident (or reflected) species by the average internal energy carried by each molecule. Thus, the above expressions are modified using:

$$H_{i,y}^{\pm} = h_{i,y}^{\pm} + N_i^{\pm} e_{i,s}^{\text{int}} \tag{2.30}$$

and

$$H_{i,y}^{M} = h_{i,y}^{M} + N_i^{M} e_{i,w}^{\text{int}} \tag{2.31}$$

in which $e_i^{\text{int}} = k_B T \, \Im$ is the internal energy of the molecule characterized by the number of internal degrees of freedom $\Im$. The internal number of degrees of freedom is related to the total degrees of freedom DOF through:

$$\text{DOF} = \Im + 3 \tag{2.32}$$

This way, the three degrees of freedom associated with the translational motion of molecules is excluded in the calculation of internal energy. The number density flux of the incident and reflected molecules can be determined as:

$$N_i^+ = \int_{-\infty}^{+\infty} dV_{ix} \int_{-\infty}^{+\infty} dV_{iz} \int_0^{+\infty} V_{iy} f_i \left(V_{ix}, V_{iy}, V_{iz}\right)\, dV_{iy} \tag{2.33a}$$

$$N_i^- = \int_{-\infty}^{+\infty} dV_{ix} \int_{-\infty}^{+\infty} dV_{iz} \int_{-\infty}^{0} V_{iy} f_i \left(V_{ix}, V_{iy}, V_{iz}\right)\, dV_{iy} \tag{2.33b}$$

$$N_i^M = \int_{-\infty}^{+\infty} dV_{ix} \int_{-\infty}^{+\infty} dV_{iz} \int_0^{+\infty} V_{iy} f_i^M \left(V_{ix}, V_{iy}, V_{iz}\right)\, dV_{iy} \tag{2.33c}$$

Next, Eqs. (2.33) are substituted into Eqs. (2.30) and (2.31) and incorporated in Eq. (2.25) with h_i replaced by H_i. Finally, summing over all species and rearranging, the following temperature–jump equation is obtained:

$$\left(\frac{T_s}{T_w}\right)^{3/2} = \frac{\sum_{i=1}^{N_g} \left(\theta_i - \gamma_i\right) \frac{n_{i,w}}{\sqrt{m_i}} \left(1 + \frac{U^2 m_i}{4 k_B T_w} + \frac{\Im}{4}\right)}{\sum_{i=1}^{N_g} \frac{n_{i,s}}{\sqrt{m_i}} \left[\left(2 - \theta_i\right) \frac{5\sqrt{\pi}}{8} \left(a_{i1} \frac{\partial \ln T}{\partial y} - \mathcal{B}_1\right) + \theta_i \left(\mathcal{B}_2 + \frac{\Im\sqrt{\pi}}{8} \mathcal{B}_1\right)\right]_s} \tag{2.34}$$

where

$$\mathcal{B}_1 = a_{i0} \frac{\partial \ln T}{\partial y} - n \sum_{j=1}^{N_g} c_{i0}^j d_{jy} \tag{2.35a}$$

$$\mathcal{B}_2 = \left(1 + \frac{\Im}{4}\right) + \frac{\mathcal{A}_4}{2} \left(3 + \frac{\Im}{2}\right) \tag{2.35b}$$

Considering Eq. (2.19), the temperature–jump boundary condition can also be written as:

$$\frac{T_s}{T_w} = \frac{\sum_{i=1}^{N_g} \frac{n_{i,s}}{\sqrt{m_i}} \left[\theta_i \left(1 + \mathcal{A}_4\right) - \frac{(2-\theta_i)\sqrt{\pi}}{2} \mathcal{B}_1\right]_s \left(1 + \frac{U^2 m_i}{4 k_B T_w} + \frac{\Im}{4}\right)}{\sum_{i=1}^{N_g} \frac{n_{i,s}}{\sqrt{m_i}} \left[\left(2 - \theta_i\right) \frac{5\sqrt{\pi}}{8} \left(a_{i1} \frac{\partial \ln T}{\partial y} - \mathcal{B}_1\right) + \theta_i \left(\mathcal{B}_2 + \frac{\Im\sqrt{\pi}}{8} \mathcal{B}_1\right)\right]_s} \tag{2.36}$$

Simplified boundary conditions

The previously obtained slip/jump conditions are for the general case and the coefficients in the Sonine polynomials need to be expressed in terms of usual transport properties in order to be applicable to practical engineering problems. The Sonine expansion coefficients $a_{i0}, a_{i1}, b_{i0},$ and c^j_{i0} are obtained using variational techniques and are expressed in terms of collision integrals. However, they can also be directly related to transport properties as follows [41]:

$$D_i^T(\xi) = \frac{n_i m_i}{2}\sqrt{\frac{2k_BT}{m_i}}a_{i0}(\xi) \tag{2.37a}$$

$$K(\xi) = -\frac{5}{4}k_B\sum_{i=1}^{N_g} n_i\sqrt{\frac{2k_BT}{m_i}}a_{i1}(\xi) \tag{2.37b}$$

$$\mu(\xi) = \frac{1}{2}k_BT\sum_{i=1}^{N_g} n_i b_{i0}(\xi) \tag{2.37c}$$

$$D_{ij}(\xi) = \frac{\rho n_i}{2nm_j}\sqrt{\frac{2k_BT}{m_i}}c^j_{i0}(\xi) \tag{2.37d}$$

where $D_i^T, K, \mu,$ and D_{ij} are the thermal diffusion coefficient, thermal conductivity, viscosity, and the ordinary diffusion coefficients, respectively. The parameter ξ in these expressions refers to the number of terms used in the Sonine polynomial expansion [41]. Usually $\xi = 1$ gives acceptable results in approximating the transport properties, except for the thermal diffusion D_i^T which vanishes for $\xi = 1$, and therefore, at least two terms should be considered in the Sonine expansion. It is apparent that a_{i1} and b_{i0} cannot be obtained explicitly from the above equations, and rather cumbersome equations given in reference [41] have to be solved to determine them exactly. However, the following approximations may be employed to obtain explicit expressions for these coefficients [11]:

$$\mu \approx \sum_{i=1}^{N_g} \frac{n_i}{n} \mu_i \tag{2.38a}$$

$$K \approx \sum_{i=1}^{N_g} \frac{n_i}{n} K_i \tag{2.38b}$$

Thus, Eqs. (2.37b) and (2.37c) yield:

$$a_{i1} \approx -\frac{4}{5} \frac{K_i}{n k_B} \sqrt{\frac{m_i}{2 k_B T}} \tag{2.39a}$$

$$b_{i0} \approx \frac{2}{n k_B T} \mu_i \tag{2.39b}$$

Having determined the Sonine expansion coefficients $a_{i0}, a_{i1}, b_{i0},$ and c_{i0}^j in terms of the usual transport properties, they can be employed to establish the slip/jump conditions at a solid boundary. The concentration–jump condition (Eq. (2.19)) can be re–written as:

$$\begin{aligned} \frac{n_{i,w}}{n_{i,s}} \left(\frac{T_w}{T_s} \right)^{1/2} &= \frac{\theta_i}{\theta_i - \gamma_i} \left[1 + \frac{\mu_i}{3 n k_B T_s} \left(\frac{\partial U_x}{\partial x} + \frac{\partial U_z}{\partial z} - 2 \frac{\partial U_y}{\partial y} \right) \right]_s + \\ & \frac{(2 - \theta_i)}{2 (\theta_i - \gamma_i)} \sqrt{\frac{\pi m_i}{2 k_B T_s}} \left[\frac{2 n^2}{\rho n_i} \sum_{j=1}^{N_g} m_j D_{ij} d_{jy} - \frac{2 D_i^T}{n_i m_i} \frac{\partial \ln T}{\partial y} \right]_s \end{aligned} \tag{2.40}$$

Following the same procedure as concentration–jump, the velocity–slip in the x direction (Eq. (2.23)) can be rewritten in terms of the usual transport properties as:

$$U_x = \frac{\sum_{i=1}^{N_g} n_{i,s} \sqrt{m_i} \left[\theta_i \left(\left(\frac{D_i^T}{n_i m_i} + \frac{K_i}{5 k_B n} \right) \frac{\partial \ln T}{\partial x} - \mathcal{S}_1 \right) + (2 - \theta_i) \mathcal{S}_3 \right]_s}{\sum_{i=1}^{N_g} n_{i,s} \sqrt{m_i} \left[\theta_i (1 + \mathcal{S}_4) + (2 - \theta_i) \mathcal{S}_2 \sqrt{\frac{\pi m_i}{2 k_B T}} \right]_s} \tag{2.41}$$

where

$$\mathcal{S}_1 = \frac{n^2}{\rho n_i} \sum_{j=1}^{N_g} m_j D_{ij} d_{jx} \tag{2.42a}$$

$$\mathcal{S}_2 = \frac{n^2}{\rho n_i} \sum_{j=1}^{N_g} m_j D_{ij} d_{jy} - \frac{D_i^T}{n_i m_i} \frac{\partial \ln T}{\partial y} \tag{2.42b}$$

$$\mathcal{S}_3 = \frac{\mu_i}{n m_i} \sqrt{\frac{\pi m_i}{2 k_B T}} \left(\frac{\partial U_x}{\partial y} + \frac{\partial U_y}{\partial x} \right) \tag{2.42c}$$

$$\mathcal{S}_4 = \frac{\mu_i}{3 n k_B T} \left(\frac{\partial U_x}{\partial x} + \frac{\partial U_z}{\partial z} - 2 \frac{\partial U_y}{\partial y} \right) \tag{2.42d}$$

In order to simplify the temperature–jump expression (Eq. (2.36)), one can first relate the number of internal degrees of freedom $\Im$ to the specific heat ratio $\bar{\gamma}$ as [86]:

$$\bar{\gamma} = \frac{\mathrm{DOF} + 2}{\mathrm{DOF}} = \frac{\Im + 5}{\Im + 3} \tag{2.43}$$

Thus, the temperature–jump boundary condition can be written as:

$$\frac{T_s}{T_w} = \frac{\sum_{i=1}^{N_g} \frac{n_{i,s}}{\sqrt{m_i}} \left[\frac{\bar{\gamma}+1}{4(\bar{\gamma}-1)} + \frac{U^2 m_i}{4 k_B T_w} \right] \left[\theta_i \left(1 + \mathcal{S}_4 \right) + \left(2 - \theta_i \right) \mathcal{S}_2 \sqrt{\frac{\pi m_i}{2 k_B T}} \right]_s}{\sum_{i=1}^{N_g} \frac{n_{i,s}}{\sqrt{m_i}} \left[\left(2 - \theta_i \right) \frac{5}{4} \sqrt{\frac{\pi m_i}{2 k_B T}} \mathcal{J}_1 + \theta_i \mathcal{J}_2 \right]_s} \tag{2.44}$$

where

$$\mathcal{J}_1 = \mathcal{S}_2 - \frac{2 K_i}{5 k_B n} \frac{\partial \ln T}{\partial y} \tag{2.45a}$$

$$\mathcal{J}_2 = \frac{\bar{\gamma} + 1}{4 \left(\bar{\gamma} - 1 \right)} + \frac{\mathcal{S}_4 \left(3\bar{\gamma} - 1 \right)}{4 \left(\bar{\gamma} - 1 \right)} + \frac{5 - 3\bar{\gamma}}{4 \left(\bar{\gamma} - 1 \right)} \sqrt{\frac{\pi m_i}{2 k_B T}} \, \mathcal{S}_2 \tag{2.45b}$$

It is also useful to rewrite these equations in terms of Newtonian viscous stresses and species mass fluxes given by:

$$\tau_i^{xy} = -\mu_i \left(\frac{\partial U_x}{\partial y} + \frac{\partial U_y}{\partial x} \right) \tag{2.46a}$$

$$\tau_i^{yy} = \frac{2\mu_i}{3} \left(\frac{\partial U_x}{\partial x} + \frac{\partial U_z}{\partial z} - 2\frac{\partial U_y}{\partial y} \right) \tag{2.46b}$$

$$J_{ix} = \frac{n^2 m_i}{\rho} \sum_{j=1}^{N_g} m_j D_{ij} d_{jx} - D_i^T \frac{\partial \ln T}{\partial x} \tag{2.46c}$$

$$J_{iy} = \frac{n^2 m_i}{\rho} \sum_{j=1}^{N_g} m_j D_{ij} d_{jy} - D_i^T \frac{\partial \ln T}{\partial y} \tag{2.46d}$$

Thereby, Eqs (2.40), (2.41) and (2.44) can be written as:

$$\frac{n_{i,w}}{n_{i,s}} \left(\frac{T_w}{T_s} \right)^{1/2} = \frac{\theta_i}{\theta_i - \gamma_i} \left(1 + \frac{\tau_i^{yy}}{2p} \right)_s + \frac{(2-\theta_i)}{(\theta_i - \gamma_i)} \frac{J_{iy}}{n_i m_i} \sqrt{\frac{\pi m_i}{2k_B T_s}} \tag{2.47}$$

$$U_x = \frac{\sum_{i=1}^{N_g} n_{i,s} \sqrt{m_i} \left[\theta_i \left(\frac{K_i}{5k_B n} \frac{\partial \ln T}{\partial x} - \frac{J_{ix}}{n_i m_i} \right) - (2-\theta_i) \frac{\tau_i^{xy}}{n m_i} \sqrt{\frac{\pi m_i}{2k_B T}} \right]_s}{\sum_{i=1}^{N_g} n_{i,s} \sqrt{m_i} \left[\theta_i \left(1 + \frac{\tau_i^{yy}}{2p} \right) + (2-\theta_i) \frac{J_{iy}}{n_i m_i} \sqrt{\frac{\pi m_i}{2k_B T}} \right]_s} \tag{2.48}$$

$$\frac{T_s}{T_w} = \frac{\sum_{i=1}^{N_g} \frac{n_{i,s}}{\sqrt{m_i}} \left[\frac{\bar{\gamma}+1}{4(\bar{\gamma}-1)} + \frac{U^2 m_i}{4k_B T_w} \right] \left[\theta_i \left(1 + \frac{\tau_i^{yy}}{2p} \right) + \frac{J_{iy}(2-\theta_i)}{n_i m_i} \sqrt{\frac{\pi m_i}{2k_B T}} \right]_s}{\sum_{i=1}^{N_g} \frac{n_{i,s}}{\sqrt{m_i}} \left[\frac{5(2-\theta_i)}{4} \sqrt{\frac{\pi m_i}{2k_B T}} \left(\frac{J_{iy}}{n_i m_i} - \frac{2K_i}{5k_B n} \frac{\partial \ln T}{\partial y} \right) + \theta_i \mathcal{J}_3 \right]_s} \tag{2.49}$$

where

$$\mathcal{J}_3 = \frac{\bar{\gamma}+1}{4(\bar{\gamma}-1)} + \frac{\tau_i^{yy}}{8p} \frac{(3\bar{\gamma}-1)}{(\bar{\gamma}-1)} + \frac{5-3\bar{\gamma}}{4(\bar{\gamma}-1)} \frac{J_{iy}}{n_i m_i} \sqrt{\frac{\pi m_i}{2k_B T}} \tag{2.50}$$

2.2.2 Boundary condition implementation

In the absence of mass accumulation (e.g., etching or deposition) on an impermeable wall, the conservation of mass requires the diffusion mass flux of each gas phase species to be balanced by its production/destruction rate due to heterogeneous reactions $\dot{s}_k$ on the wall as:

$$\dot{s}_k w_k = \mathbf{J}_k \cdot \hat{\mathbf{n}} \qquad\qquad k = 1, 2, \ldots, N_g \tag{2.51}$$

The rate of production/depletion of gas species $\dot{s}_k$ depends on the molar concentration of species on the catalytic wall, not at the edge of the Knudsen layer. The relation between these values is dictated by the concentration jump boundary condition, i.e. Eq. (2.47). On the other hand, the diffusion flux at the edge of the Knudsen layer into the gas-phase depends on the concentration gradients outside the Knudsen layer. This is shown schematically in Fig. 2.3 where a typical wall control volume is shown with respect to the Knudsen layer. Note that the right hand side of Eq. (2.51) only comprises the gas–phase species, while the left hand side involves all species, including the surface species.

The surface reaction effects are manifested through the wall boundary conditions. The production rate of *surface* species $\dot{s}_n$, on the other hand, is governed by:

$$\frac{\partial Z_n}{\partial t} = \frac{\dot{s}_n}{\Gamma}\sigma_n - \frac{Z_n}{\Gamma}\frac{\partial \Gamma}{\partial t} \qquad\qquad n = 1, 2, \ldots, N_s \tag{2.52}$$

The second term on the right hand side of the above equation represents the change in the total number of available sites. In the present work, this term is dropped since due to the employed surface reaction mechanism schemes, the total number of available sites remains conserved as the reaction takes place on the walls. At steady state the left hand

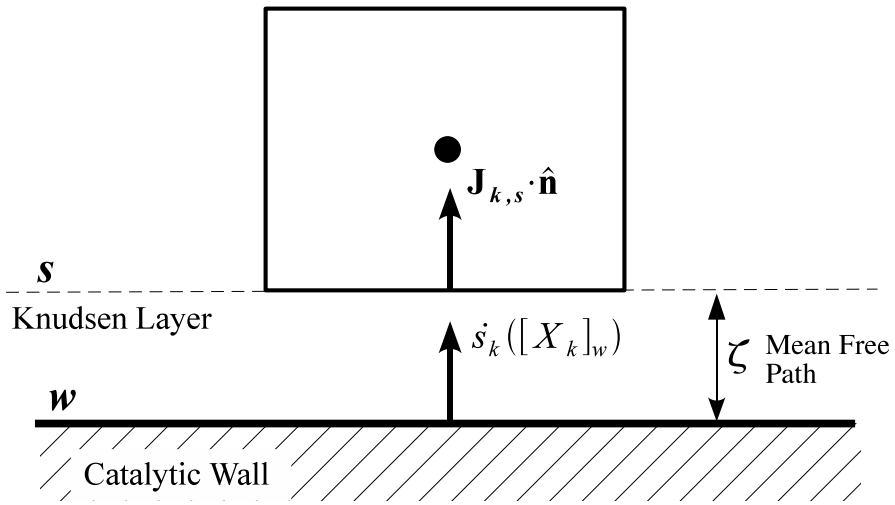

Figure 2.3: Schematic of a generic control volume next to the catalytic wall outside the Knudsen layer.

side of this equation will also be zero which makes the net production rate of surface species $\dot{s}_n$ equal to zero. However, this transient term in Eq. (2.52) is retained to facilitate the convergence of the system of equations [62]. For instance consider a very simple mechanism involving only two steps of reaction:

$$\begin{aligned} \mathrm{AB} + * &\longrightarrow \mathrm{A}^* + \mathrm{B} \\ \mathrm{A}^* &\longrightarrow \mathrm{A} + * \end{aligned} \tag{2.53}$$

in which $*$ denotes an open site on the catalytic surface and A^* is the surface–adsorbed species. The molar production rate of the open site $\dot{s}_*$ and surface–adsorbed species $\dot{s}_{\mathrm{A}^*}$ can be evaluated as:

$$\dot{s}_* = -k_1[X_{\mathrm{AB}}][X_*] + k_2[X_{\mathrm{A}^*}]$$
$$\dot{s}_{\mathrm{A}^*} = k_1[X_{\mathrm{AB}}][X_*] - k_2[X_{\mathrm{A}^*}] \tag{2.54}$$

in which k_1 and k_2 are forward rate constants of steps 1 and 2. If these equations are substituted in Eq. (2.52) with the unsteady term on its left hand side dropped, two identical equations are obtained which makes the whole system of equations ill–posed. Therefore, the transient term is retained in Eq. (2.52) to remove the ill–posedness of the problem during the numerical simulation. The steady nature of the problem makes this term zero as the solution progresses in time. This way, the surface coverage equation can be written as:

$$\frac{\partial[X_n]}{\partial t} = \dot{s}_n \qquad\qquad n = 1, 2, \ldots, N_s \tag{2.55}$$

Equations (2.51) and (2.52) form a closed set of stiff non–linear Differential Algebraic Equations (DAE) for $N_g + N_s$ unknowns which is generally handled using the Newton method. The details about the numerical treatment of these equations are discussed in [20, 54, 62, 90, 100].

Chapter 3

Numerical implementation

The governing equations are discretized using the finite volume method. A non–staggered (colocated) arrangement is employed for the solution of the flow field following the Rhie and Chow [82] formulation. Implementing the Pressure Weighted Interpolation Method (PWIM), the control volume face velocities are related to nodal pressure values. A linear deferred correction scheme is also used to improve the upwind approximation in descretizing the advection terms. The details about the finite volume formulation are given in Appendix A.

After each step in the solution of gas phase species, the flux matching boundary condition (2.51) and the surface species production rate (2.52) equations are solved on every wall element. The connection between the molar concentration of species on the wall and at the edge of the Knudsen layer is established utilizing the concentration jump boundary condition. In each iteration, the molar concentration of species at the wall required for the calculation of the heterogeneous production rate $\dot{s}_k$ in Eq. (2.51) are written in terms of the molar concentration of species at the edge of the Knudsen layer using Eq. (2.47). This

way, Eqs. (2.51) and (2.52) will form a closed set of $N_g + N_s$ equations to solve for molar concentration of species at the edge of the Knudsen layer and surface coverage of species at the wall. This set of non–linear DAEs are solved using the SUNDIALS code [40]. The solution to this set of equations yields the surface species site fractions on the *wall* and the mass fractions of gas phase species at the edge of the *Knudsen layer* which are employed as the proper boundary conditions for the next iteration. The mixture transport properties as well as the pure species properties are obtained using the CHEMKIN database [47].

The numerical code is validated at different stages. Initially, a 3D extension of the code is developed for non–reacting compressible flow of air within rectangular channels. Mixture–averaged properties of air along with first–order velocity slip and temperature jump boundary conditions are used in the simulations. Grid independence, validation against the available theoretical and numerical predictions and the results are presented in the following sections. The gas phase and catalytic reactions are validated afterwards by comparing the simulation results with the experimental and numerical data of Appel *et* al. [3] in a planar geometry. Finally, the proposed set of boundary conditions for multicomponent mixtures in section 2.2 are validated against the predictions of Direct Simulation Monte Carlo (DSMC) method for non–reacting H_2/N_2 and $H_2/N_2/CO_2$ mixtures. The DSMC simulations are carried out by Amir Ahmadzadegan (PhD candidate at the Department of Mechanical and Mechatronics Engineering, University of Waterloo).

3.1 Developing gaseous slip–flow in rectangular microchannels with variable physical properties[1]

Flow and heat transfer properties of rectangular microchannels with slip/jump boundary conditions have previously been studied. Reviewing the results of theoretical and experimental studies, Rostami et al. [84] concluded that the available conventional macro–channel theories are not adequate to predict the flow and heat transfer characteristics of gaseous flow in microchannels. Morini and Spiga [67] analytically determined the velocity field in fully developed incompressible laminar slip–flow in rectangular microchannels of arbitrary aspect ratio. Yu and Ameel [105] used an integral transform technique to solve the energy equation with no axial conduction assuming a fully developed incompressible slip–flow field. Renksizbulut et al. [81] studied the effect of rarefaction at the entrance region of rectangular microchannels numerically, for different channel aspect ratios with constant physical properties. Kuddusi and Ceten [53], Kuddusi [52] and Ghodoossi and Eğrican [33] conducted analytical studies on the heat transfer properties of thermally and hydrodynamically developed incompressible flows under different boundary condition combinations. More recently, Hettiarachchi et al. [39] studied slip–flow in rectangular microchannels with a constant wall temperature boundary condition numerically with developing velocity and temperature fields. In their simulations, they neglected viscous dissipation and assumed constant physical properties. Husain and Kim [44] used temperature dependent thermophysical property simulations to optimize the design of rectangular microchannel heat sinks without velocity slip or temperature jump at the wall. Nonino et al. [71, 72] studied the effect of temperature dependent viscosity on heat transfer characteristics of no–slip liquid

[1] A brief version of this section including some figures is published as an article in the International Journal of Heat and Fluid Flow, 2011, Vol. 32, 117-127 [108].

flow in 2D and 3D channels. Their results suggest that the temperature dependence of viscosity cannot be ignored within a considerable range of working conditions especially at the channel inlet. Van Rij et al. [94, 95] studied the effect of viscous dissipation and second order slip/jump boundary conditions on flow and heat transfer characteristics of rectangular microchannels. In order to avoid any considerable changes in physical properties, they chose a very small temperature difference between the inlet and the wall and employed constant physical properties in their simulations.

In this section, three dimensional gaseous slip–flow and heat transfer in rectangular microchannels of different aspect ratios are studied numerically for developing flow and temperature fields at different Knudsen numbers.

3.1.1 Problem statement

A schematic view of the microchannel and the coordinate system is depicted in Fig. 3.1. The aspect ratio of the channel is $\alpha = W/H$ with H and W being the channel height and width, respectively. The flow direction is along the x axis. For the low Péclet number values used in this study, a channel length of $L = 6D_h$ is sufficient for the flow and temperature field to develop [94], with $D_h = 2HW/(H+W)$ being the hydraulic diameter of the channel. Also, since the main scope of the present work is to examine the importance of property variations (mainly due to temperature change) on the flow and heat transfer characteristic, a short microchannel is chosen for the simulations. All the variables in this section are non–dimensionalized using the channel hydraulic diameter D_h, reference axial velocity u_r, and reference fluid properties ρ_r, μ_r, $c_{p,r}$ and λ_r. Pressure is normalized by $\rho_r u_r^2$. All other non–dimensional groups are defined based on the reference properties as:

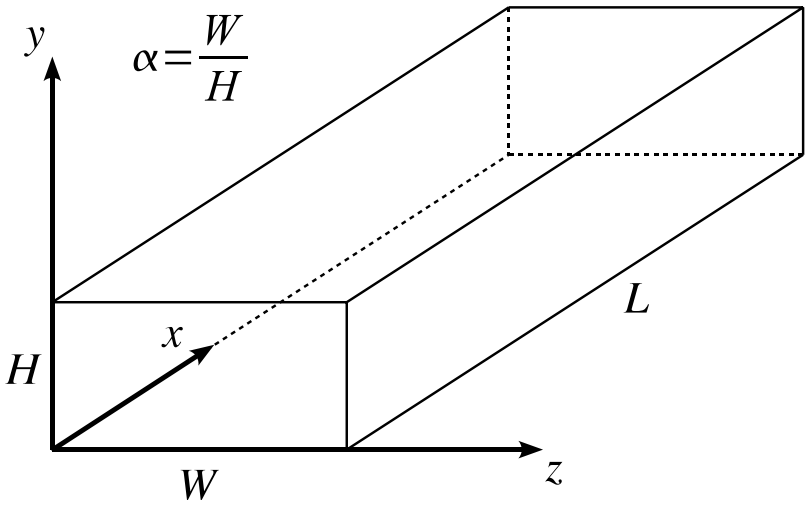

Figure 3.1: Channel geometry and the coordinate system.

$$\mathrm{Re} = \frac{\rho_r u_r D_h}{\mu_r} \quad ; \qquad \mathrm{Pr} = \frac{c_{p,r}\mu_r}{\lambda_r} \tag{3.1}$$

The flow is mass–driven, and the outlet pressure is specified based on the reference density and the wall temperature. Also, zero axial gradients at the outlet are specified for temperature and velocity. At the channel inlet uniform velocity and temperature profiles are specified such that $u = u_{\mathrm{in}}$, $v = w = 0$ and $T = T_{\mathrm{in}}$. When simulating the variable physical property cases, since the inlet pressure is not known *a priori*, the inlet density is calculated at each iteration and then used to update the inlet velocity for the next iteration. In the case of constant physical properties, the inlet density and velocity will remain constant throughout the solution. The Reynolds number is set constant while comparing the constant and variable–property simulations. Also, when different aspect ratios are studied, in order to make a meaningful comparison between different cases, the hydraulic diameter of the channel is assumed to be constant. This way, the mass flow rate per unit

area $\rho u = \mu_r \mathrm{Re}/D_h$ remains the same for different channel aspect ratios. The channel surfaces are assumed to be at constant temperature T_w with proper velocity–slip and temperature–jump boundary conditions applied at the wall. According to slip flow theory, slip/jump at the wall is proportional to the velocity and temperature gradients. Velocity–slip and temperature–jump boundary conditions for non–reacting single component flows can be expressed in a non–dimensional form as [107]:

$$u_s = \frac{5\pi \mathrm{Kn}}{16} \left(\frac{2 - \theta_v}{\theta_v} \right) \left(\frac{\partial u}{\partial n} + \frac{\partial u_n}{\partial x} \right)_w \tag{3.2a}$$

$$T - T_w = \frac{\mathrm{Kn}}{\mathrm{Pr}} \left(\frac{2 - \theta_T}{\theta_T} \right) \left(\frac{2\bar{\gamma}}{\bar{\gamma} + 1} \right) \left(\frac{\partial T}{\partial n} \right)_w \tag{3.2b}$$

where u_s is the normal velocity and n is the wall normal direction. The tangential momentum accommodation coefficient θ_v and energy accommodation coefficient θ_T are equal to zero for specular reflection at the wall and equal to 1 for diffuse reflection [15]. For most engineering applications they are close to unity and considering the approximate nature of the slip theory, they are assumed to be equal to 1 in this section.

3.1.2 Grid independence and validation

The solution domain is discretized using an orthogonal, non–uniform grid with linear expansion in the x, y and z directions. Grid point density is higher near the walls and channel inlet in order to better resolve the gradients at these regions. The effect of grid size on the key flow parameters was investigated and it was found that for a square channel, any grid density beyond $30 \times 30 \times 160$ (x, y, z) with grid expansion ratios of 1.15, 1.15, 1.035, respectively, yields grid–independent results. For channel aspect ratios other than 1, the number of grid points and expansion ratios were adjusted to maintain the same grid res-

olution. Also, based on the flow symmetry, only one quarter of the channel is used in the numerical simulations.

Ebert and Sparrow [25] analyzed the velocity and pressure drop effects in rarefied gaseous flow in rectangular ducts and proposed a series solution for the fully–developed velocity distribution within the channel. Their analysis is for incompressible constant–property flow, and considering the coordinate system and dimensionless parameters of the present study, can be expressed as:

$$\begin{aligned} u(y,z) &= \frac{WH}{4\Psi}\sum_{i=1}^{\infty}\frac{\cos\phi_i(y-\frac{1+\alpha}{4\alpha})}{\phi_i^3}\left[\frac{\sin(\phi_i W/2)}{W/2+\mathrm{Kn}\sin^2(\phi_i W/2)}\right] \\ &\times \left[1.0-\frac{\cosh\phi_i(z-\frac{1+\alpha}{4})}{\cosh(\phi_i H/2)+\mathrm{Kn}\phi_i\sinh(\phi_i H/2)}\right] \end{aligned} \tag{3.3}$$

$$\Psi=\sum_{i=1}^{\infty}\frac{1}{\phi_i^5}\left[\frac{\sin^2(\phi_i W/2)}{W/2+\mathrm{Kn}\sin^2(\phi_i W/2)}\right]\left[\frac{H}{2}\phi_i-\frac{\tanh(\phi_i H/2)}{1+\mathrm{Kn}\phi_i\tanh(\phi_i H/2)}\right] \tag{3.4}$$

where ϕ_i are calculated using the eigenfunction $\cot(\phi_i W/2)=\mathrm{Kn}\phi_i$. The velocity profile obtained from numerical simulation of incompressible flow in a square duct is compared to the analytical solution at different Knudsen numbers and is presented in Fig. 3.2. Very good agreement is observed between the numerical simulation and analytical results. The fully-developed friction factor can also be retrieved from the analytical solution by averaging the wall shear stress peripherally. The results for the case of $\mathrm{Kn}=0$ are presented in Table 3.1.

In order to verify the numerical treatment of the energy equation, the fully developed Nusselt number for constant–property flow is compared to previously published numerical

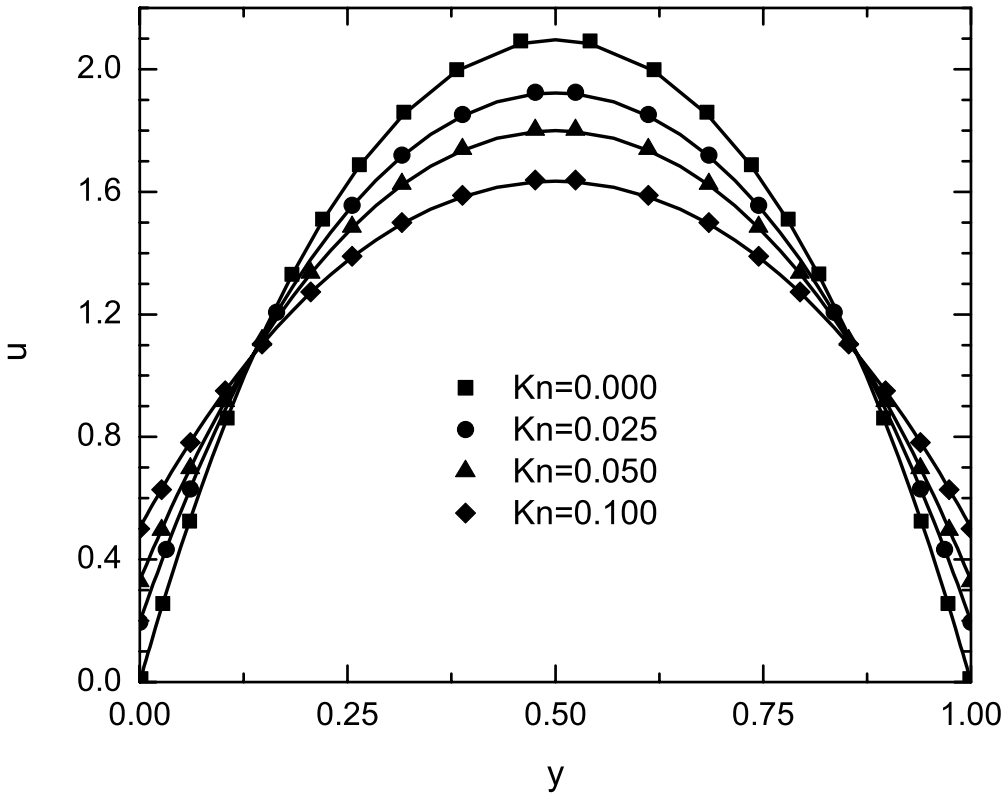

Figure 3.2: Fully–developed velocity profiles on the $z = 0.5$ plane of a square channel; solid lines: analytical solution; symbols: numerical results.

results at different Knudsen numbers and aspect ratios. These results are also presented in Table 3.1. The Nusselt number in the developing region along a rectangular channel is also compared to available analytical solutions of Yu and Ameel [105] as depicted in Fig. 3.3 with x^* being the dimensionless axial position $\tilde{x}/D_h\mathrm{RePr}$ (reciprocal Graetz number) and $\tilde{x}$ the dimensional axial position. Different mesh sizes in the x direction are tested to achieve grid independency in the longitudinal direction. In this comparison, the energy equation is solved using the fully–developed velocity profile with zero axial conduction at $\mathrm{Pr} = 0.7$. Comparison shows good agreement between the present study and the analytical

Table 3.1: Friction factor and Nusselt number for fully–developed no–slip flow in rectangular channels at Re = 1.

Cross–sectional grid		fRe		Nu	
		Present	Ebert and Sparrow [25]	Present	Renksizbulut et al. [81]
$\alpha = 1$	10×10	13.29	14.22	3.02	3.32
	25×25	14.03		3.21	
	30×30	14.14		3.26	
$\alpha = 2$	10×20	14.71	15.54	3.59	3.69
	25×50	15.40		3.64	
	30×60	15.46		3.66	

solution.

3.1.3 Results and discussion

In this section, the effects of compressibility and variable physical properties on the flow and heat transfer characteristics will be presented. Since a large number of variables can change in this type of problem, some parameters are kept constant in order to make a meaningful comparison between the constant and variable–property simulations. To this end, throughout this section the Reynolds number is set equal to 0.1 which is appropriate for microchannel flows. The inlet gas temperature in all simulations is specified to be $T_{\text{in}} = 300$ K, and the wall temperature is assumed to be $T_{\text{w}} = 350$ K. Obviously, the choice of a 50 K temperature difference between the inlet and the wall is arbitrary. A high temperature difference can drastically change the flow and heat transfer characteristics, as expected. On the other hand a relatively low temperature difference of 50 K is usually considered to have a negligible effect on flow characteristics. In the present study a low

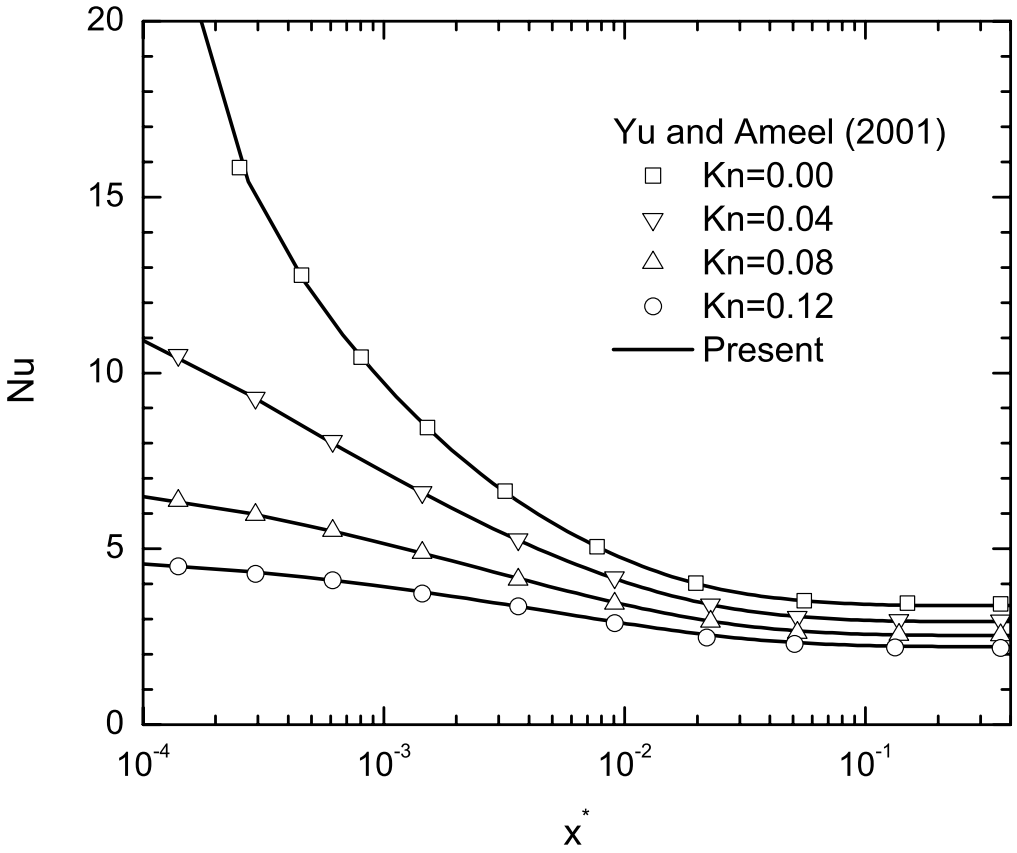

Figure 3.3: Nusselt number along a rectangular channel ($\alpha = 2$) compared to the analytical solution at different Knudsen numbers with negligible axial conduction.

temperature difference between the wall and the inlet is chosen in order to examine whether this is a good assumption for microchannel flows or not. Reference physical properties of the gas are summarized in Table 3.3. The reference properties of the gas are used in the constant–property simulations.

Initially, the system of equations is solved for the case where density changes both with pressure and temperature while keeping other physical properties constant. This will help identify the effect of density variation on flow characteristics independently. Then, all phys-

Table 3.2: Reference physical properties of the gas utilized in the simulations of rectangular microchannel.

Density (kg/m^3)	1.0
Viscosity (Pa s)	1.8522×10^{-5}
Conductivity (W/m K)	2.607×10^{-2}
Constant–pressure specific heat (J/kg K)	1004.5
Specific gas constant (J/kg K)	286.9
Specific heat ratio, γ (J/kg K)	1.4
Viscosity index, ϖ	0.7
Prandtl number, Pr	0.714
Hydraulic diameter, D_h (μm)	10.0

ical properties of the fluid are also allowed to change as temperature varies. This way, the relative importance of each set of parameters on the flow and heat transfer characteristics can be analyzed.

In the variable–density and variable–property simulations, the reported Knudsen numbers are those at the channel outlet and the Knudsen number elsewhere is related to the temperature and pressure of the gas as [49]:

$$\frac{\mathrm{Kn}}{\mathrm{Kn}_{\mathrm{out}}} = \left(\frac{p_{\mathrm{out}}}{p}\right)\left(\frac{T}{T_{\mathrm{out}}}\right)^{0.5+\varpi} \tag{3.5}$$

where ϖ is the viscosity index and can range from 0.6 to 0.9. In the present study, for air as the working fluid, ϖ is assumed to be equal to 0.7.

Density variation

An equation of state can be utilized to link the density of the gas to its pressure and temperature within the microchannel. The ideal gas assumption is accurate within the

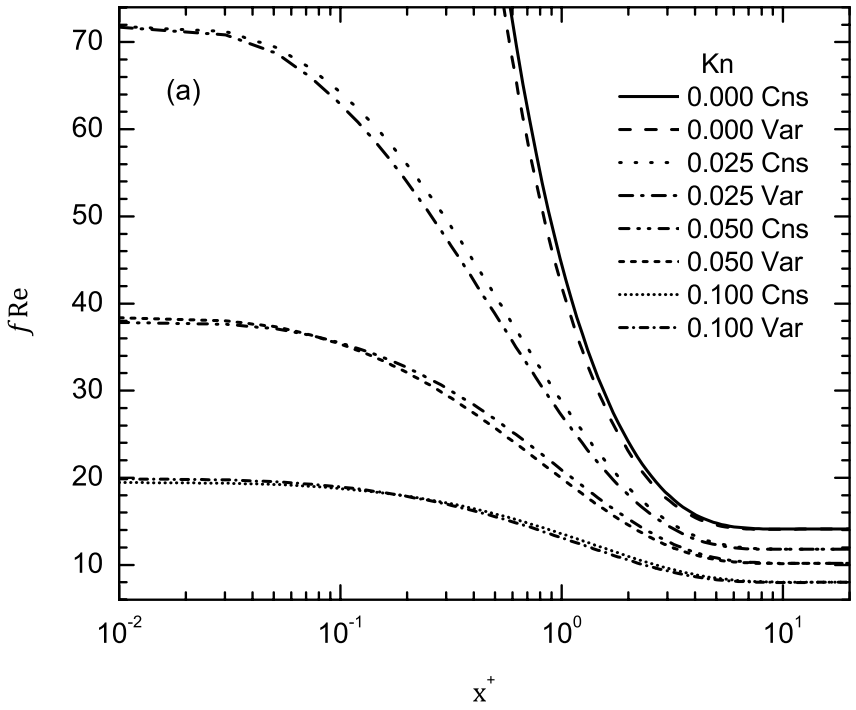

Figure 3.4: Friction coefficient distribution at Re = 0.1 along a square channel; constant (Cns) and variable–density (Var) simulations. All other physical properties are assumed to be constant.

range of pressures and temperatures considered in this study [46].

An interesting observation about the effect of variable–density simulation of the flow is the change in the local friction coefficient $f = 2\tau_w/\rho_{\text{in}}U_{\text{in}}^2$. In Fig. 3.4 the friction coefficient of the flow at the entrance region of the channel is shown. The velocity gradient in the entrance region of the channel is higher in constant–density simulations, while in the fully developed region, velocity profiles are similar. This should result in higher friction coefficients in the entrance region. This behaviour is confirmed in Fig. 3.4 for the no–slip flow with higher friction coefficients for the constant–density simulation in the entrance region, and equal friction coefficient in the fully–developed region. However, in

the slip flow regime, friction coefficient behaves differently. Right at the channel inlet, the friction coefficient of the variable–density simulation is higher. Further down the channel the constant–density friction takes over and finally the results of the two simulations merge together in the fully–developed region. The initial increase in the friction coefficient values of the variable–density simulation is due to variable Knudsen number. The Knudsen number at the channel inlet is lower in the variable–density simulations compared to constant–density as observed in Eq. (3.5). Previous studies have shown that the friction factor is generally higher for a lower Knudsen number under similar conditions [81]. Therefore, in the slip–flow simulations, the variable–density cases have lower Knudsen numbers compared to constant–density simulations which results in higher friction factors at the inlet. However, increase in temperature and decrease in pressure along the channel levels the Knudsen number of variable and constant–density cases. This way, after a certain point down the channel, the constant–density friction coefficient takes over. Finally in the fully–developed region, all parameters merge in both simulations, as expected. The maximum difference in the friction coefficient is observed in the case of no–slip flow where the relative difference is slightly higher than 10% at the channel inlet. As the Knudsen number increases, this difference diminishes due to the competing effects of density and Knudsen number variations.

Variable physical properties

In order to study the effects of variable physical properties on the flow and heat transfer characteristics of rarefied gaseous flow, viscosity, thermal conductivity and specific heat are determined by the following correlation:

$$\psi = a + bT + cT^2 + dT^3 \tag{3.6}$$

Table 3.3: Thermo–physical property coefficients for air.

ψ	a	b	c	d
μ (Pa s)	2.345×10^{-6}	6.203×10^{-8}	-2.920×10^{-11}	7.267×10^{-15}
k (W/m K)	-4.536×10^{-3}	1.234×10^{-4}	-7.945×10^{-8}	2.728×10^{-11}
c_p (W/m K)	1013	-0.1571	4.910×10^{-4}	-2.055×10^{-7}

in which ψ is any of the above–mentioned properties and a, b, c and d are constants given in Table 3.3 for air. This fitting is accurate for 300K $\leq T \leq$ 1000K with the maximum error being less than 1.5% in the temperature range of the present work [80]. Density is calculated using the ideal gas law.

The effect of variable physical properties on the mean velocity and average slip velocity along a square channel is shown in Fig. 3.5. As observed, the mean velocities in the variable–property simulations are almost the same for different Knudsen numbers at the channel inlet. The mean velocities converge to the constant–property case down the channel. Between the two ends, mean velocity is lower for higher Knudsen numbers. This behaviour is mainly due to the temperature distribution across the channel. Lower Knudsen number cases have higher heat transfer coefficients at every axial location of the channel (as will be shown shortly). This results in higher temperatures at every cross section compared to the higher Knudsen number case, which in turn translates to a lower density. Since the mass flow rate is constant in all cases, the mean velocity will be higher for lower Knudsen number cases. The normalized average slip velocity u_{slip}/u_m of constant and variable–property simulations at different Knudsen numbers is shown in Fig. 3.5 (b). Interestingly, the normalized slip velocities of constant and variable–property cases are very close. This implies that although the absolute numerical values are different, the velocity distributions have similar profiles.

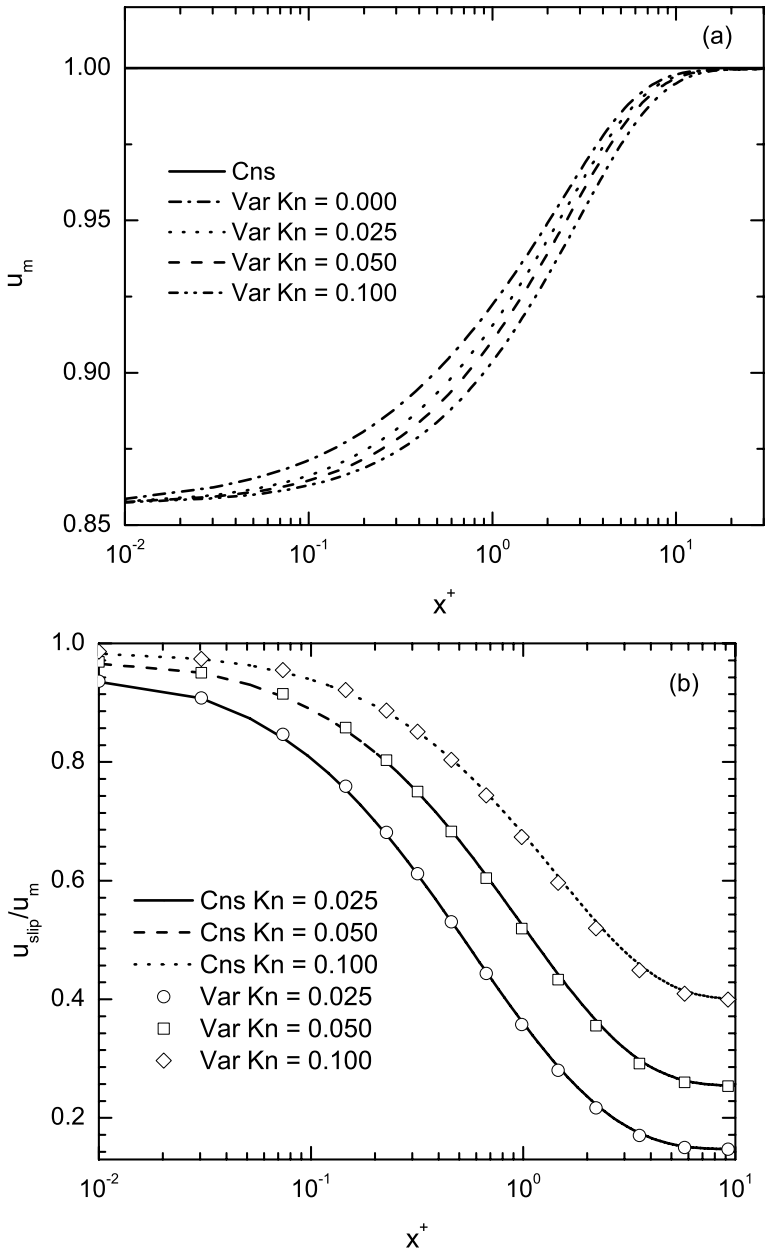

Figure 3.5: Mean velocity (a) and normalized average axial slip velocity (b) variation along a square channel; constant (Cns) and variable-property (Var) simulations at Re=0.1.

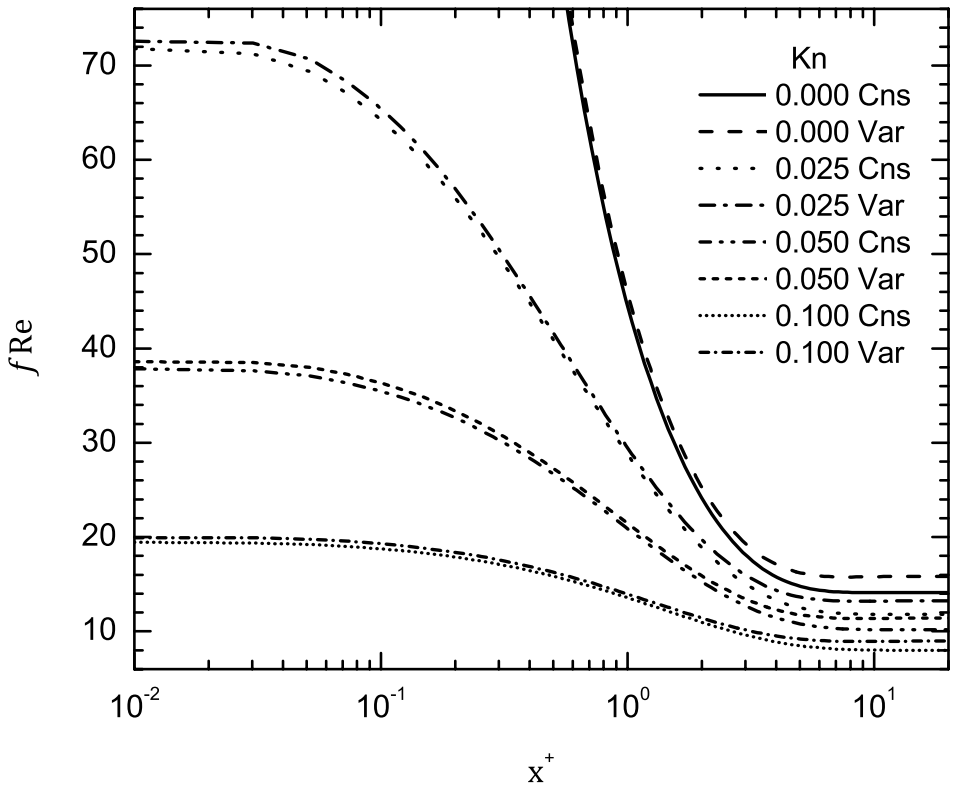

Figure 3.6: Axial variation of friction factor along a square channel at different Knudsen numbers of constant (Cns) and variable–property (Var) simulations at Re = 0.1.

For practical engineering purposes, the friction coefficient in the channel is of key importance. Figure 3.6 demonstrates the variation of friction coefficient along a square channel for different Knudsen numbers. In all cases, the variable–property simulations predict a higher friction factor compared to the constant–property cases. This can be attributed to a number of reasons. The change in gas density affects the friction coefficient predictions in the entrance region as discussed earlier. Also a higher gas viscosity next to the wall results in a higher shear stress and consequently higher pressure drop along the channel. In the no–slip flow, the effect of density variation is opposing the increased viscosity which results in

similar friction coefficient predictions for constant and variable–property simulations in the entrance region. Towards the fully–developed region, the density variation effect diminishes and the increased viscosity effect dominates, which results in higher friction coefficient in variable–property simulations. In the slip–flow cases, on the other hand, the density variation effect is opposing the viscosity effect in some regions and contributing to it in other regions, as observed in Fig. 3.6. As described earlier, initially the change in Knudsen number (due to the density variation) plays a pivotal role in determining the friction coefficient behaviour. A lower Knudsen number at the inlet in the variable–density/property simulations increases the local friction coefficient, contributing to the increased viscosity effect. However, further down the channel, the reduced velocity gradient due to change in density influences the friction coefficient distribution in variable–density simulations whereas in variable–property simulations the increased viscosity compensates for the drop in the velocity gradient. This behaviour is clearly displayed in Fig. 3.7 where the three different simulation types, namely constant–property, variable–density, and variable–property simulations are compared for the case of $\mathrm{Re} = 0.1$ and $\mathrm{Kn} = 0.05$. For the particular problem considered here, the friction coefficient is always higher in the variable–property simulations. However depending on the importance of viscosity effect as compared to density variation (which in turn depends on the gas properties and problem configuration), the friction factor can exhibit a mixed behaviour similar to the ones observed in Fig. 3.4.

The friction coefficients in the entrance region of the channel are compared to each other in Fig. 3.8 for different aspect ratios. The variable–property simulations predict a higher friction factor compared to the constant–property simulations in all cases, complying with Fig. 3.6. Also, the friction coefficient in the developing and fully–developed regions is generally higher as the aspect ratio increases. Another interesting observation is the asymptotic value of the friction coefficient at the channel inlet regardless of the channel

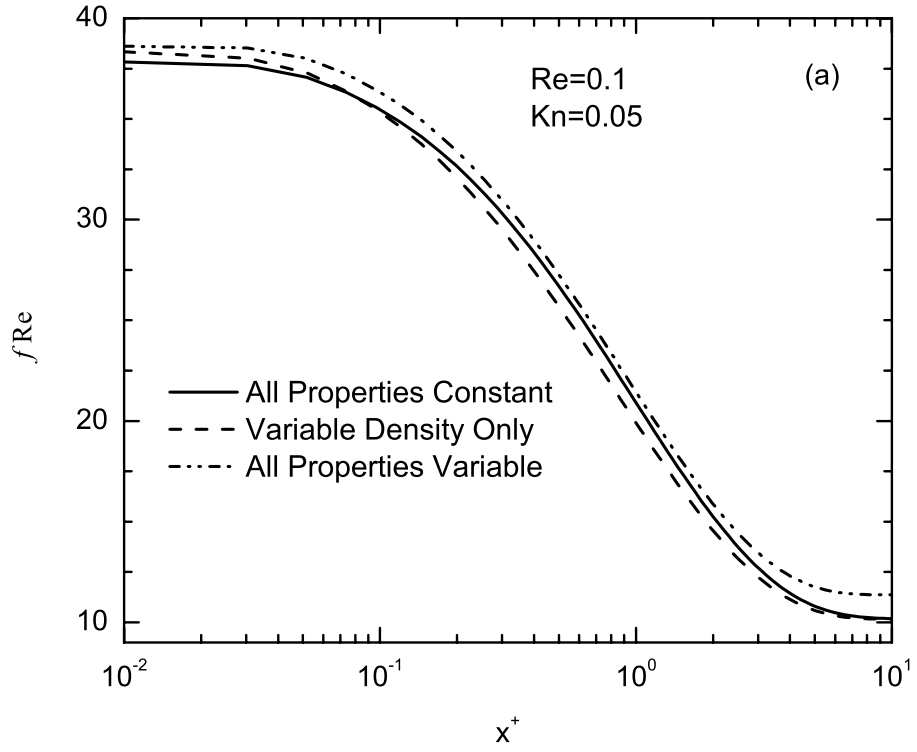

Figure 3.7: Effect of different type of simulations on friction factor variation along a square channel at Re = 0.1 and Kn = 0.05.

geometry. As pointed out by Niazmand et al. [70], at the channel inlet the fluid has not developed enough to recognize the geometry. This is true for the variable–property simulation as well.

The Nusselt number along the channel reveals a clear insight about the effect of variable properties on the heat transfer coefficient. To this end, the heat transfer rate is peripherally averaged in order to define the Nusselt number as:

$$\mathrm{Nu} = \frac{hD_h}{\lambda_r} = \frac{D_h\overline{\lambda(\partial T/\partial n)}}{\lambda_r(T_m - T_w)} \tag{3.7}$$

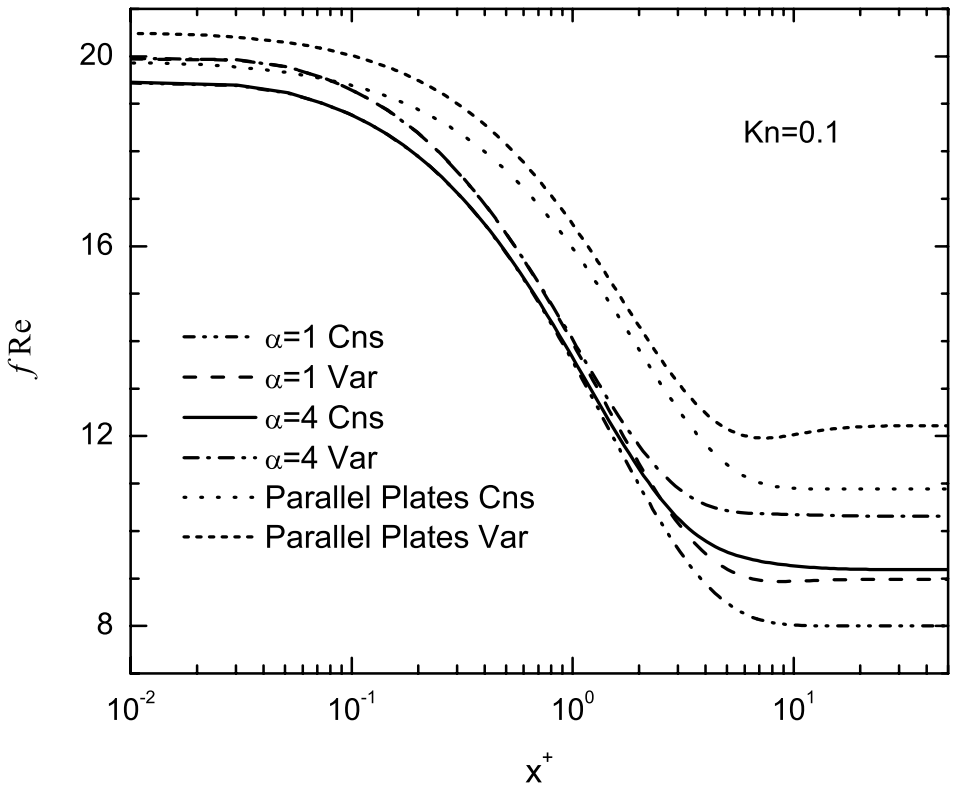

Figure 3.8: Variation of friction coefficient at Kn = 0.1 and Re = 0.1 for different channel aspect ratios; constant (Cns) and variable–property (Var) simulations.

where $\overline{\lambda(\partial T/\partial n)}$ is the peripherally averaged heat flux at the wall at any axial location, λ_r is the reference conductivity, and T_m is the bulk mean temperature for the variable–property simulations defined as:

$$T_m = \frac{\int_A \rho c_p T \vec{U} \cdot \vec{n}\, \mathrm{d}x}{\int_A \rho c_p \vec{U} \cdot \vec{n}\, \mathrm{d}x} \tag{3.8}$$

The Nusselt numbers calculated from constant and variable–property simulations along the channel are shown in Fig. 3.9 for different Knudsen numbers. As expected, the Nusselt number is higher for the variable–property simulations, consistent with the predictions by Liu et al. [58] for no–slip flows in planar microchannels. For example a relatively low

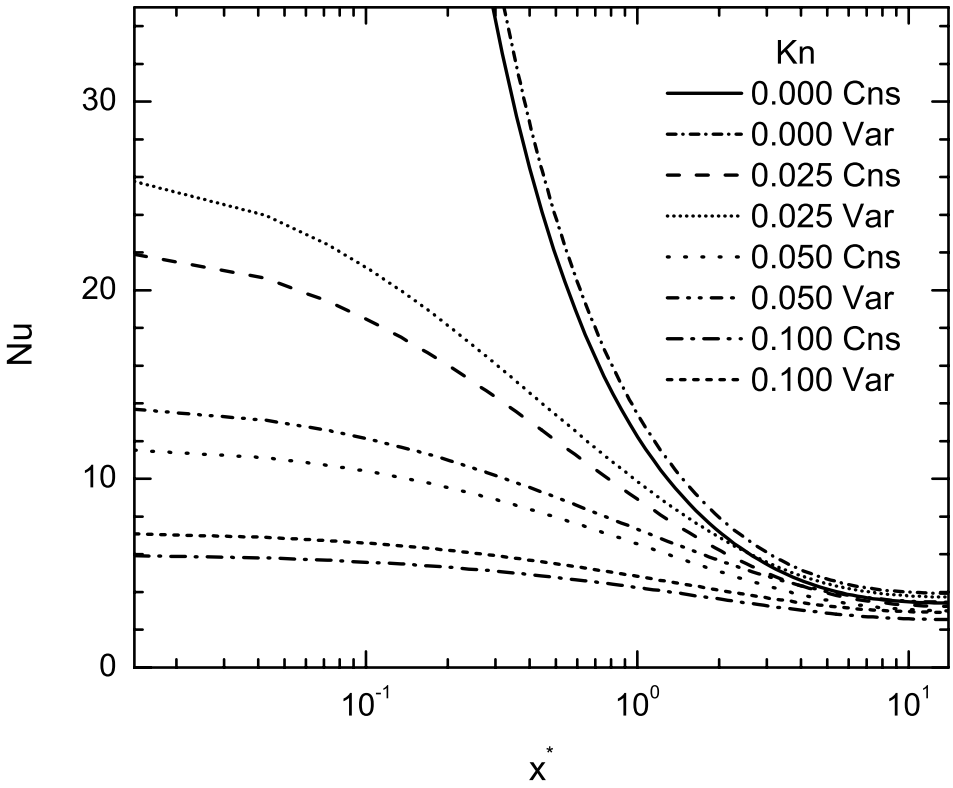

Figure 3.9: Axial variation of Nusselt number along a square channel at different Knudsen numbers of constant (Cns) and variable–property (Var) simulations at Re = 0.1.

temperature difference of 50K considered in the present study has increased the Nusselt number at the channel inlet by about 20% at Kn = 0.1. This is mainly due to Knudsen number variation and higher conductivity of the flowing gas at higher temperatures. At the channel entrance, the Knudsen number variation plays the dominant role in the increase in Nusselt number. In the fully–developed region, where the Knudsen number becomes closer to its outlet value, the difference between constant and variable–property simulations is only affected by the increase in the gas conductivity.

The effect of channel aspect ratio on the Nusselt number is shown in Fig. 3.10 where

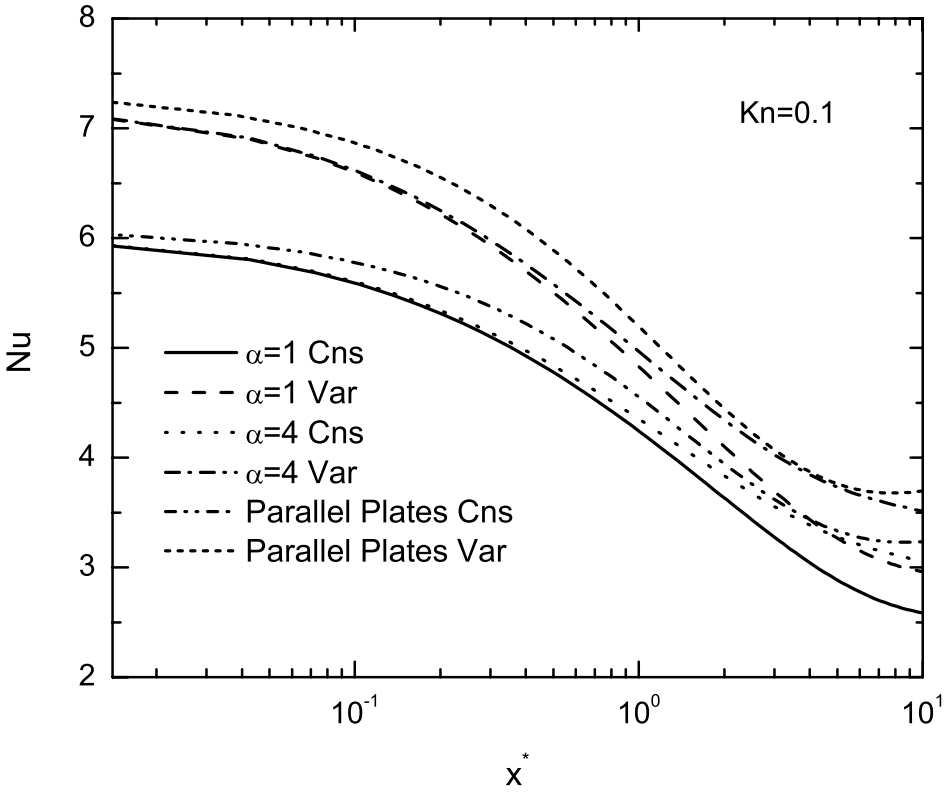

Figure 3.10: Axial variation of Nusselt number along a square channel at different Knudsen numbers of constant (Cns) and variable–property (Var) simulations at Re = 0.1.

the constant and variable–property simulations of a square channel, a rectangular channel and parallel plates at Kn = 0.1 are compared to each other. Variable–property simulations, as expected, predict a higher Nusselt number for all channels. Also as the channel aspect ratio increases, the Nusselt number in the developing and fully–developed regions increases. Similar to the friction coefficient at the channel inlet, the Nusselt number also demonstrates an asymptotic value at the inlet regardless of the channel geometry in both constant and variable–property simulations.

3.2 Lean hydrogen/air mixture oxidation

Combustion of lean H_2/air mixtures in Pt–coated microchannels is investigated numerically in planar geometry. The governing mass, momentum, energy, and species continuity equations are described in section 2.1. Detailed gas phase and surface reaction mechanisms along with a multi–component species diffusion model are used. These equations were discretized using the colocated finite volume method. After each step in the solution of gas phase species, the flux matching boundary condition (2.51) and the surface species production rate (2.52) equations are solved on every wall element. These equations form a set of non–linear DAEs and are solved using the SUNDIALS code [40]. The details about the numerical treatment of these equations are discussed in [20, 62]. The solution to this set of equations yields the surface species site fractions and the mass fractions of gas phase species on the wall which are employed as the wall boundary conditions for the next iteration. The mixture transport properties as well as the pure species properties are obtained using the CHEMKIN database [47].

3.2.1 Problem statement

A schematic view of channel geometry and the coordinate system are shown in Fig. 3.11. The channel height is H and the main flow is in the x direction. The numerical code is validated by comparing the results with experimental and numerical data. A lean hydrogen/air mixture with an equivalence ratio of $\varphi = 0.28$ is chosen corresponding to Case 3 of the experimental data of Appel *et* al. [3]. The inlet velocity is 2 m/s resulting in an inlet Reynolds number of $\mathrm{Re}_{in} = 1389$. The channel height and length are 7 mm and 250 mm, respectively. The gas inlet temperature is 312 K while the wall temperature T_w is a function of x and varies between 1150 K to 1250 K. The details of the test case are given

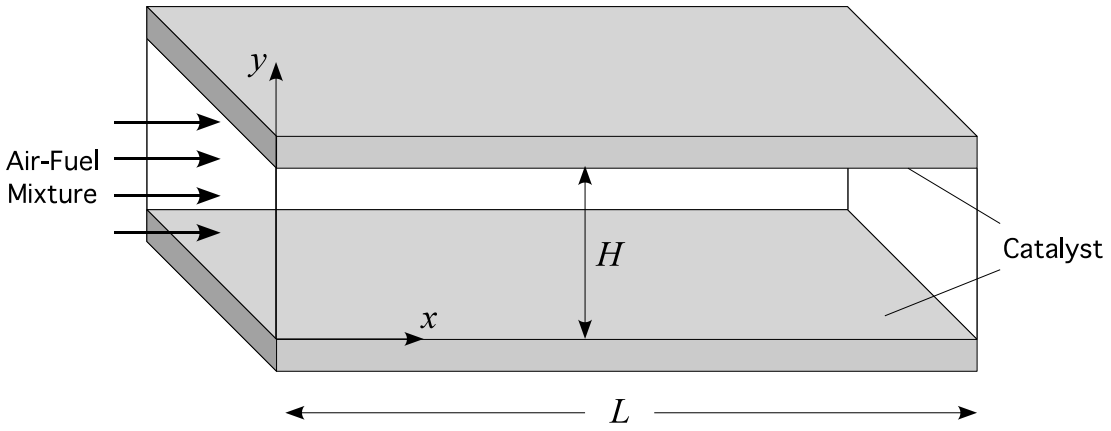

Figure 3.11: Planar 2D channel geometry and the coordinate system.

in [3]. For this comparison a numerical grid size of 260×36 was used.

The OH mole fraction distribution along the channel is compared to the experimental data in Fig. 3.12. The sudden rise in OH mole fraction is the initiation of gas phase combustion which is predicted accurately by the present numerical simulation. The difference in OH mole fraction values by a maximum of about 7% is well within the range of measurement uncertainties. Mole fractions of the fuel H_2 and the product H_2O across the channel at $x = 25$ mm are shown in Fig. 3.13. As observed, the numerical predictions are in good agreement with the experimental data. The minor differences between the numerical predictions of the current work and those reported by Appel *et* al. [3] are mainly due to the different treatment of the multi-component diffusion term in the calculation of the diffusion mass fluxes. In order to avoid the matrix inversion, an effective (mixture–averaged) diffusion coefficient has been employed in [3]. They have also included diffusion mass fluxes of other species to take into account the multicomponent diffusion effects, whereas in the present work Eq. (2.7) is used for the calculation of diffusion mass fluxes.

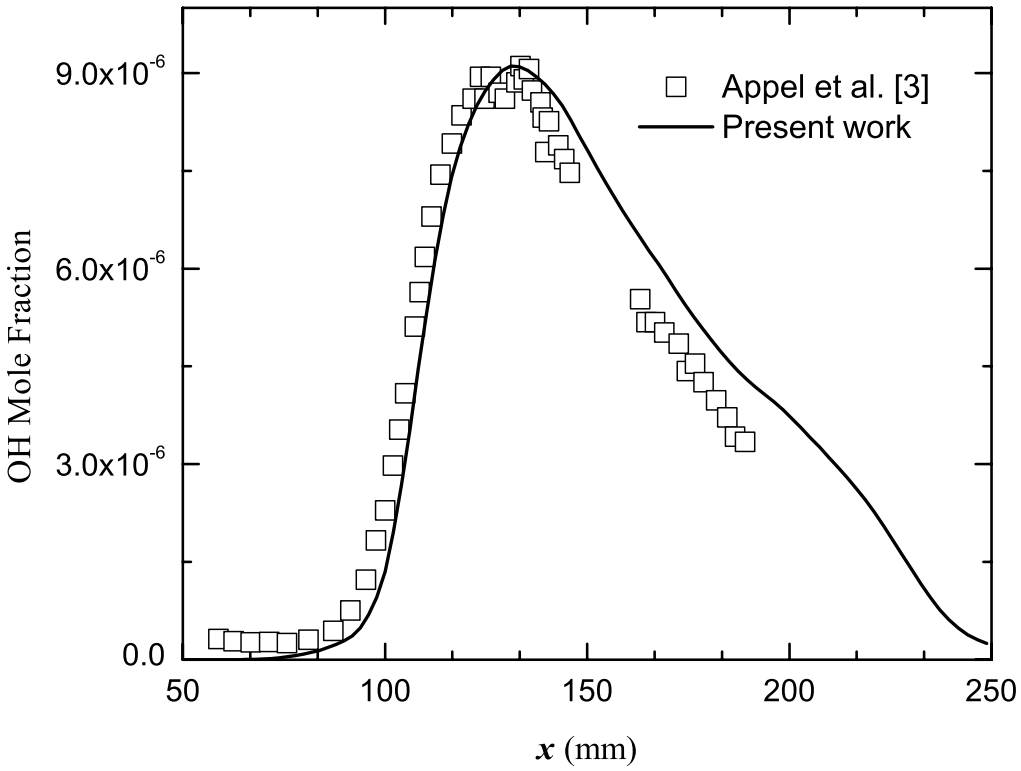

Figure 3.12: OH mole fraction along the channel compared to experimental data.

This can also affect the temperature distribution, which in turn alters the reaction rates due to their strong temperature dependence. The temperature field prediction, as observed in Fig. 3.14, is also in good agreement with the experimental results. The difference between the numerical results of [3] and the current work can again be traced backed to the coupling between the energy equation, diffusion mass fluxes and reaction rates.

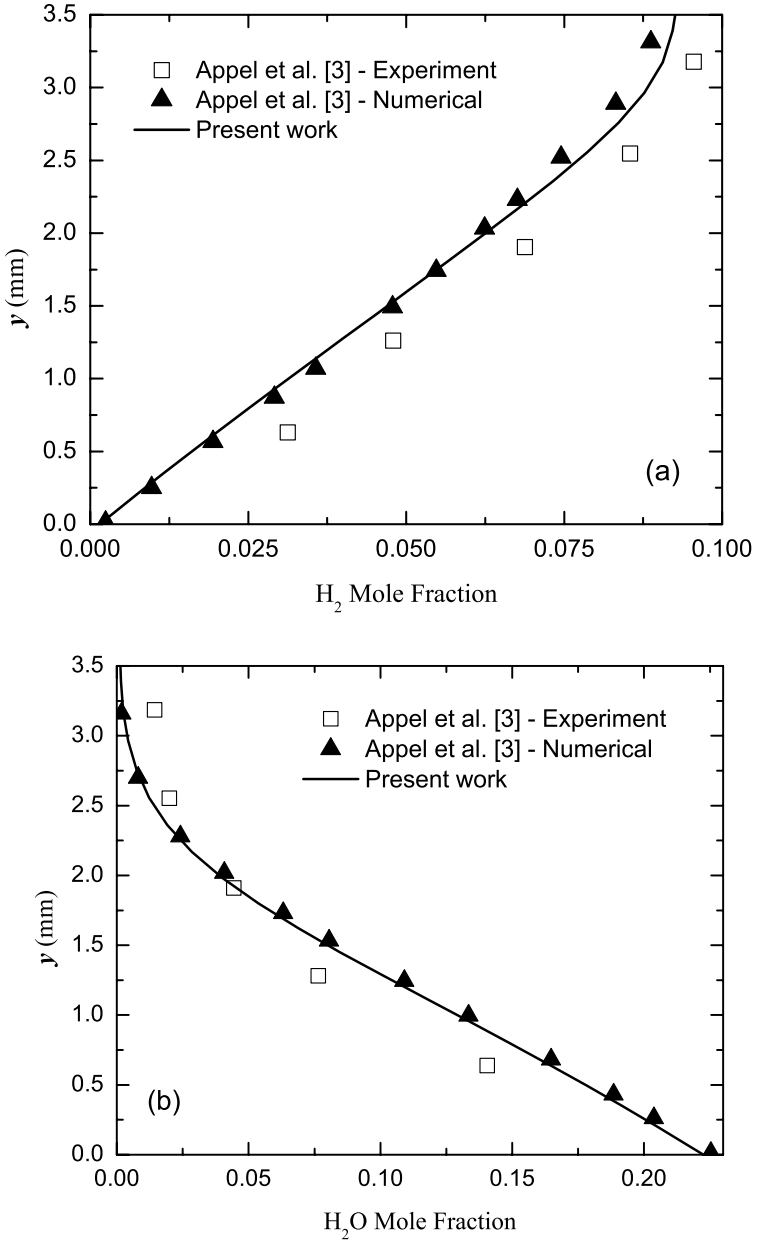

Figure 3.13: Comparison of (a) H_2 mole fraction, (b) H_2O mole fraction across the channel at $x = 25$ mm with experimental and numerical results; the channel height is 7 mm. For clarity only 12 data points are presented from the numerical work of [3].

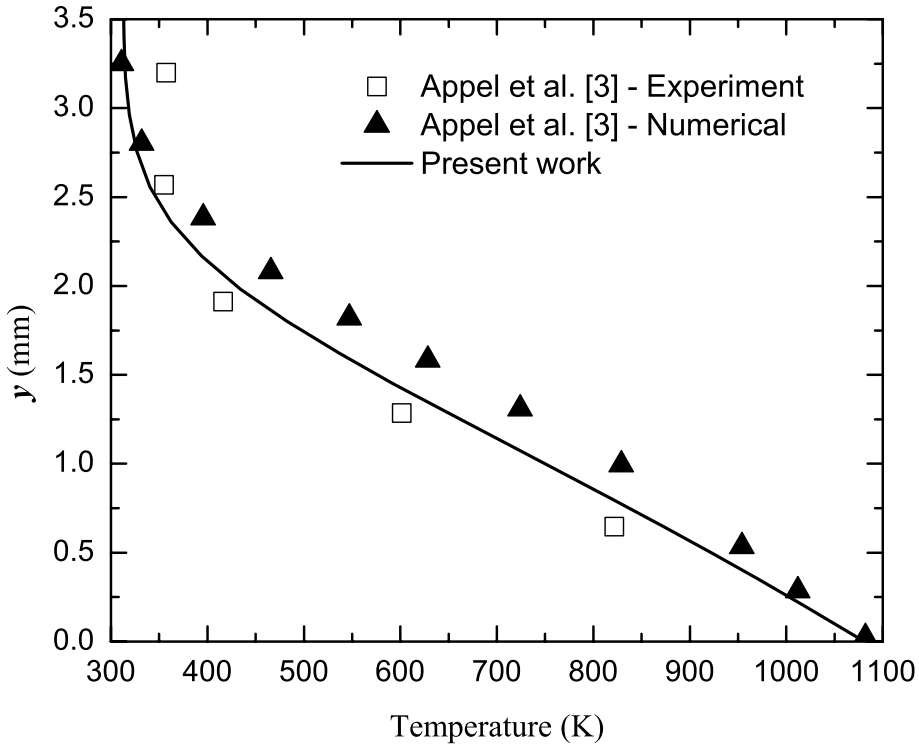

Figure 3.14: Temperature variation across the channel at $x = 25$ mm compared to experimental data and numerical simulations. For clarity only 11 data points are presented from the numerical work of [3].

3.3 Comparison between Navier–Stokes and DSMC simulations of multicomponent gaseous flow in microchannels

3.3.1 Introduction

DSMC simulation of rarefied gaseous flow in microchannels and nanochannels has been adopted by researchers due to its intrinsic ability to render physical phenomena such as

pressure and thermal diffusion which are difficult to capture by continuum transport models [9, 10]. Based on the current state of the literature, the multicomponent flows require further investigation and different schemes should be properly verified. Although the effects of velocity slip and temperature jump on flow and heat transfer characteristics of single–component gases have been extensively studied in microchannels [105, 68, 81, 95], non–equilibrium transport in multicomponent flows still remains to be studied in–depth. In this section, the gaseous flow of H_2/N_2 and $H_2/N_2/CO_2$ mixtures in a planar geometry is numerically investigated with two distinct methods: DSMC and Navier–Stokes with slip/jump boundary conditions (NSWS/J). The results from the two schemes are compared to each other for verification. A proper set of slip/jump boundary conditions introduced in section 2.2 which accounts for the effect of individual species is used along with a colocated finite volume method to consider possible velocity and temperature discontinuities at the wall. The DSMC method, being inherently capable of capturing these non–equilibrium phenomena at the wall, can be effectively utilized to verify the implementation and accuracy of the proposed multicomponent slip/jump boundary conditions.

3.3.2 Problem statement

The channel geometry and the coordinate system are the same as before shown in Fig. 3.11. The governing mass, momentum, energy, and species continuity equations are described in section 2.1. Detailed gas phase and surface reaction mechanisms along with a multi–component species diffusion model are used. These equations were discretized using the colocated finite volume method. The mixture transport properties as well as the pure species properties are obtained using the CHEMKIN database [47]. In the slip flow regime, the continuum equations for mass, momentum and energy conservation can

still be employed but proper slip/jump boundary conditions should be specified to account for non–equilibrium effects in the Knudsen layer. In this section, the set of velocity slip and temperature jump boundary conditions, described in section 2.2 for multicomponent mixtures, are employed at the wall. The accommodation coefficient θ is equal to zero for specular reflection at the wall and equal to 1 for diffuse reflection [15]. For most engineering applications they are close to unity and for comparison purposes, in the present work, they are assumed to be equal to 1 in both schemes.

In this problem, the flow is mass driven such that the mass flux of each species is constant at the channel inlet. For the low Péclet number flows considered here, the numerical simulations show that a channel length of about $4H$ is sufficient for for all the variables to fully develop. The treatment of the inlet boundary condition deserves more attention. Since the mass flux of each species is constant at the channel inlet, the overall inlet mass flux will also remain constant. This approach is especially useful when dealing with low Péclet number ($\mathrm{Pe}_k = \mathrm{ReSc}_k$, where Sc is the Schmidt number) flows in which the inlet diffusion mass flux can be significant. The inlet mass flux of each species, which is held constant, consists of the diffusion mass flux and the convective mass flux of that species. At low Péclet number flows, the diffusive mass transfer generally becomes more effective. If there is a positive diffusive flux of one species into the channel, in order to keep the mass flux constant, the inlet mass fraction of that species should be adjusted (lowered) accordingly. This way, the total mass flux of that species, $\vec{m}_k'' = \rho Y_k \mathbf{U} + \mathbf{J}_k$ remains constant. This procedure eliminates the inaccuracy in ignoring the incoming (or outgoing) inlet diffusive mass flux of species at low Péclet number flows. At each iteration, the inlet mass fraction of all species Y_k and the mass–averaged inlet velocity $\mathbf{U}$ are calculated using $\vec{m}_k'' = \rho Y_k \mathbf{U} + \mathbf{J}_k = \text{const}$ (N_g constraints) along with $\sum_{k=1}^{N_g} Y_k = 1$. The diffusive fluxes of species $\mathbf{J}_k$ are calculated from the previous iteration.

Table 3.4: Operating conditions and geometrical specification of different simulation cases.

	Mixture	H (μm)	L (μm)	$\dot{m}''_{\text{in}}$ (kg/m^{2}s)	T_w (K)	% Composition (by mass)		
						H_2	N_2	CO_2
Case 1	H_2/N_2	1.5	6.0	50.0	350	10.0	90.0	–
Case 2	H_2/N_2	1.5	6.0	50.0	300	10.0	90.0	–
Case 3	H_2/N_2	1.5	6.0	100.0	350	10.0	90.0	–
Case 4	H_2/N_2	1.5	6.0	50.0	400	10.0	90.0	–
Case 5	H_2/N_2	4.0	16.0	50.0	350	10.0	90.0	–
Case 6	$H_2/N_2/CO_2$	1.5	6.0	50.0	350	2.7	37.8	59.5

3.3.3 Results and discussion

In this section, different field variables derived from both schemes are compared to each other. Throughout the simulations, two channel heights of $H = 1.5$ μm and $H = 4$ μm are considered. The channel length is $L = 4H$. The inlet gas temperature is specified to be $T_{in} = 300$ K in all cases while the wall temperature T_w is maintained at 350 K, unless otherwise stated. The outlet pressure is assumed to be atmospheric. The reported velocities throughout this section are normalized by a reference velocity of $u_r = 50$ m/s. The details about the operating conditions of different cases studied here are summarized in Table 3.4. The specified inlet mass compositions listed in this table yields the same number of molecules from different species entering the channel.

Mass and Momentum Transfer

The velocity slip at the edge of the Knudsen layer is shown in Fig. 3.15 along the channel for case 1. As observed, the two schemes are in a very good agreement with a maximum difference of about 11% right at the channel inlet. The DSMC method predictions are

slightly lower than the NSWS/J method at the channel inlet, however, the predictions of the two methods quickly merge further downstream. In both methods, the velocity slip is the highest right at the channel inlet where the gradients are the strongest. In this region, the normal velocity gradient is the dominant term in the velocity slip boundary condition (see Eq. (2.48)). This can be easily observed in the "*No Thermal Creep*" case of Fig. 3.15 where the axial temperature gradient term in the velocity slip boundary condition is artificially set equal to zero. Except for the region very close to the inlet, the velocity slip on the wall remains intact with the exclusion of this term. As the mixture flows down the channel, these gradients quickly fade away due to strong diffusion effects at such small length scales. After this initial drop, the slip velocity increases progressively. The gradual increase in the velocity slip further down the channel is mainly due to the decrease in pressure which in turn increases the Knudsen number (mean free path) along the channel. In this part of the channel, the normal gradients in the viscous stress term τ^{xy} govern the velocity slip behavior.

The velocity field in slip flow regime can be obtained analytically with simplified assumptions. The solution of the Navier–Stokes equations with the velocity slip boundary condition in an isothermal flow yields [8]:

$$\frac{u_s}{u_c} = \frac{\mathrm{Kn}}{0.25 + \mathrm{Kn}} \tag{3.9a}$$

$$\frac{u_s}{u_c} = \frac{\mathrm{Kn}/\left(1.0 + \mathrm{Kn}\right)}{0.25 + \mathrm{Kn}/\left(1.0 + \mathrm{Kn}\right)} \tag{3.9b}$$

in which, u_c is the fluid velocity at the center of the channel and Kn may vary along the channel as the flow field develops. The first equation is obtained using the first–order (Maxwell) slip boundary condition while the second equation employs a higher order slip model [8]. In these equations, the Knudsen number is calculated based on the mixture–

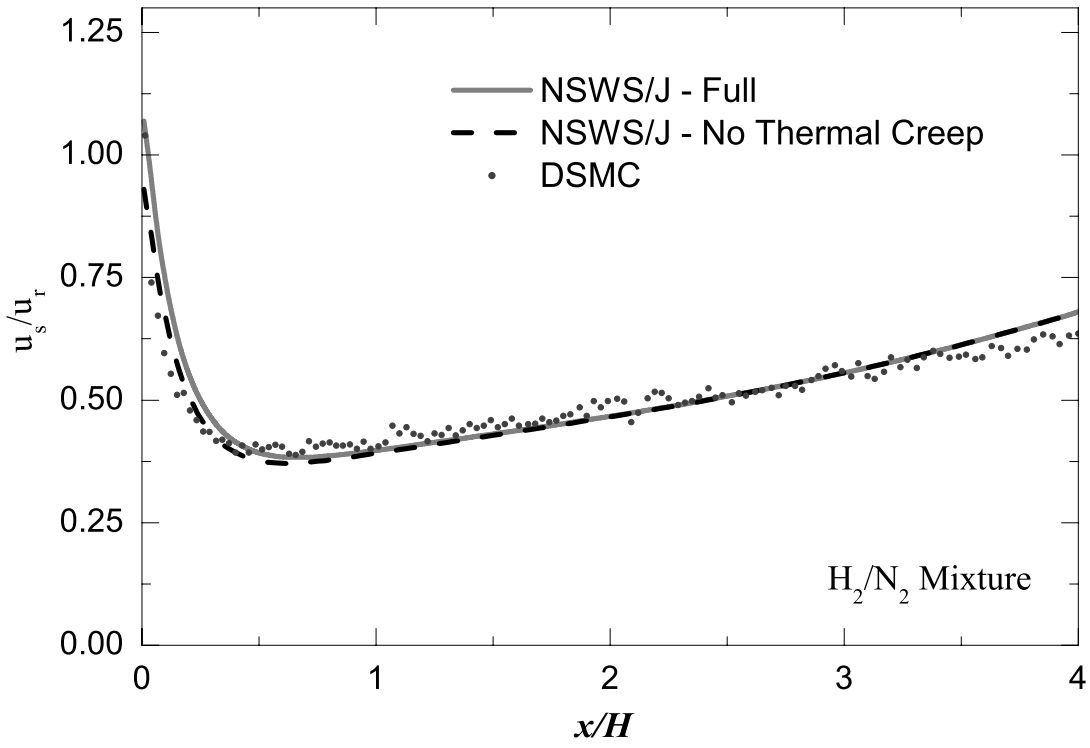

Figure 3.15: Velocity slip predictions of the NSWS/J and DSMC methods along the microchannel.

averaged mean free path as:

$$\zeta = \frac{16}{5} \frac{\mu}{\rho\sqrt{2\pi RT}} \tag{3.10}$$

where ζ is the mixture mean free path. All other properties are calculated at the edge of the Knudsen layer.

The normalized slip velocity derived from these theoretical estimates are compared to the numerical predictions of the NSWS/J model in Fig. 3.16 for an isothermal flow (case 2) with $T_w = 300$ K. The considerable differences between the results at the channel inlet are due to the assumptions made in derivation of the analytical forms. These equations

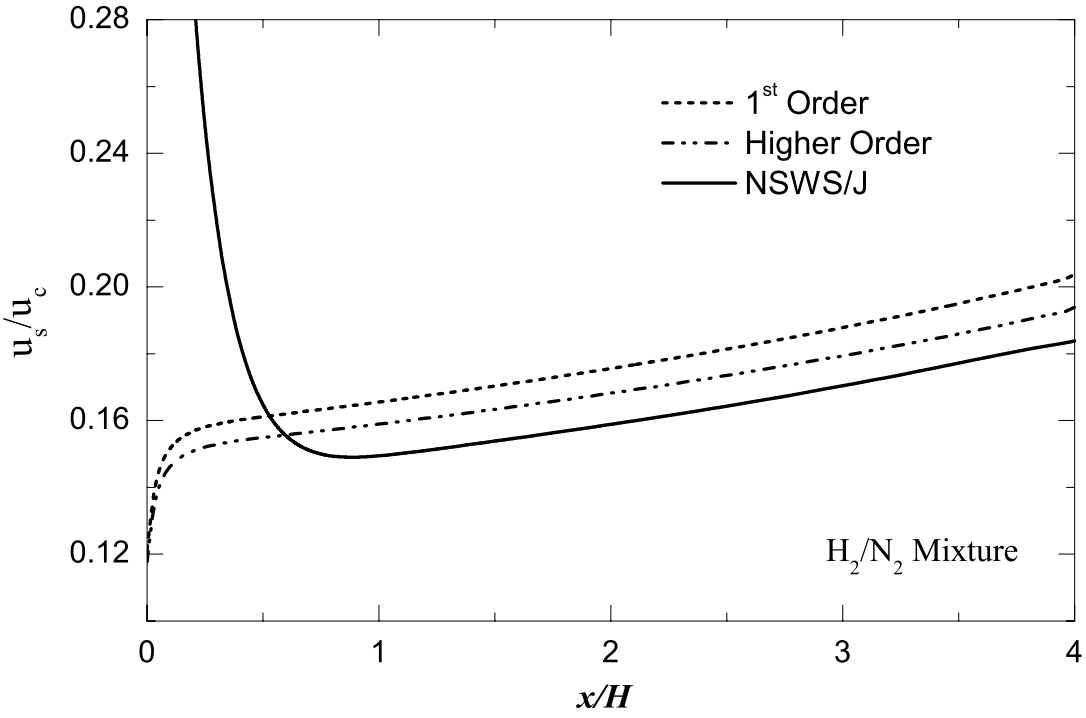

Figure 3.16: Comparison of the normalized slip velocity in different models in an isothermal flow (case 2) with $T_w = 300$ K.

basically neglect the entrance effects and the results are only comparable beyond $x/H = 1.0$. As the flow develops inside the channel, all methods show similar trends, although the first and higher order theoretical results generally over–predict the slip model simulations by about 11% and 6%, respectively. As expected, the higher order analytical prediction is closer to the slip model employed in the present work.

The velocity slip along the channel for cases 1–4 are shown in Fig. 3.17 to illustrate the effect of different operating conditions. For the isothermal channel (Case 2), the temperature gradients (due to viscous dissipation) are extremely small and the shear stresses τ_k^{xy} govern the slip velocity behavior as can be inferred from Eq. (2.48). As stated earlier,

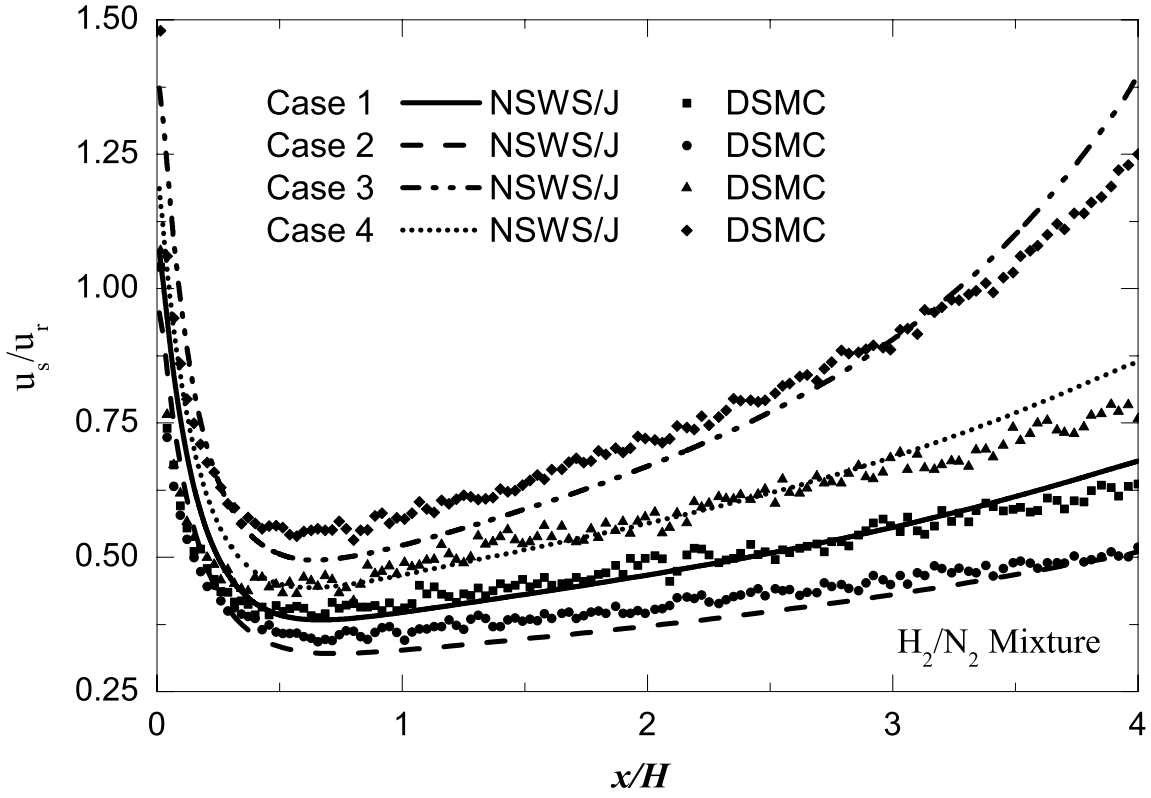

Figure 3.17: Normalized slip velocity under different operating conditions.

the thermal creep effect is limited to the channel inlet and the velocity gradients are the dominant factor in rendering the slip velocity. Therefore, as the inlet mass flux (and consequently the velocity gradients) increases in Case 3, the slip velocity escalates accordingly, as predicted closely by both methods. The increase in the wall temperature generally increases the slip velocity along the channel (Case 4). The difference between the slip velocity predictions of the two methods increases in the entrance region for Case 3 where the inlet mass flux is doubled. The presence of steep velocity and temperature gradients in this region aberrates the NSWS/J solution from the molecular simulation prediction. The same scenario applies to Case 4 with a higher wall temperature.

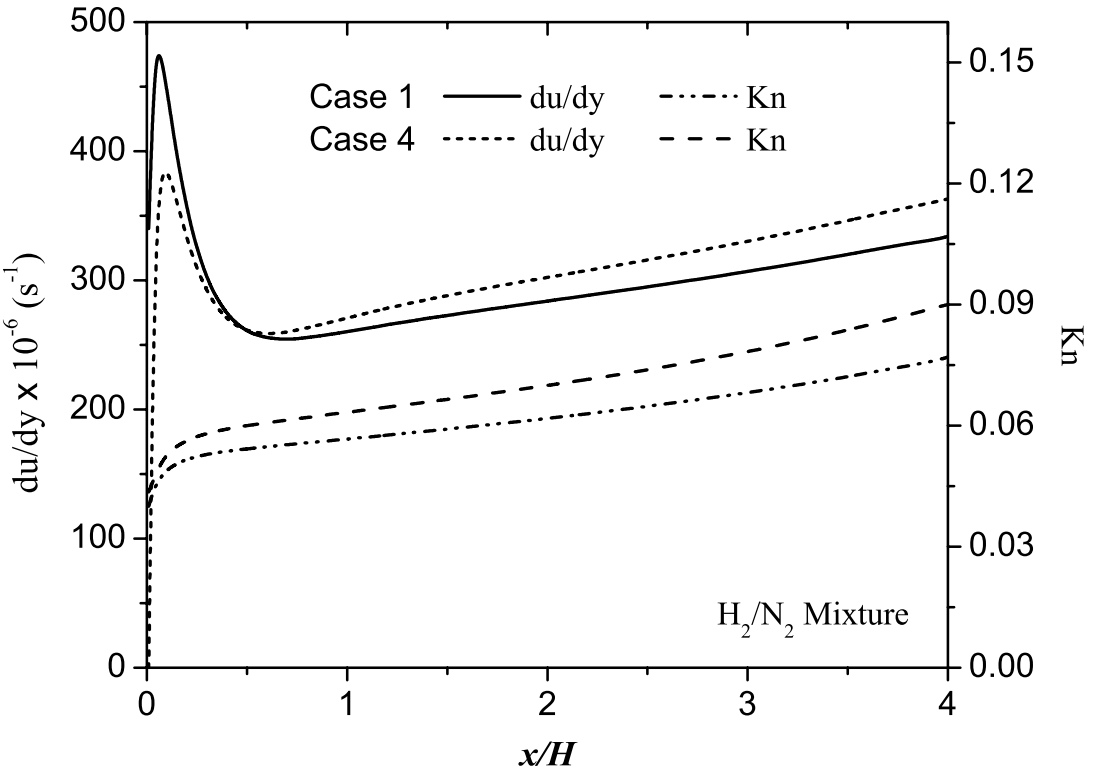

Figure 3.18: Velocity gradient and Knudsen number at the wall for cases 1 and 4 along the channel.

To investigate the effect of wall temperature in more detail, the normal velocity gradient and the Knudsen number are shown in Fig. 3.18 for Cases 1 and 4. An increase in the wall temperature increases the molecular mean free path which, as has been shown before, magnifies the velocity slip [81]. The increase in the molecular mean free path (and Knudsen number) occurs all along the channel as depicted in Fig. 3.18. The normal velocity gradient, on the other hand, generally decreases in the developing region (except very close to the inlet) which opposes the Knudsen number effect in this region. Very low normal velocity gradients right at the channel inlet are due to the high velocity slip caused by the strong

thermal creep in this region. As the flow develops along the channel, the normal velocity gradient takes over at elevated temperatures which contributes even further to the increase in velocity slip at the wall. Increased wall temperatures supplement the axial temperature gradients in the developing region where these gradients are the strongest which can counter balance the decrease in normal velocity gradients.

In order to compare the DSMC results with the slip model calculations, the velocity distribution across the channel at different axial locations are shown in Fig. 3.19 for Case 1. The velocity field predictions of the two methods are in good agreement across the channel at these axial locations. Interestingly, although the steepest gradients occur close to the wall, the maximum deviation between the simulation results of the axial velocity occurs at the channel mid–plane. The velocity component in the y–direction illustrates the same trend in both methods as the initial cross–stream velocity quickly fades away along the channel.

The two methods predict the same velocity slip in larger channels as shown in Fig. 3.20, although the numerical scattering is more pronounced in the 4 μm channel. The decrease in the Knudsen number due to increased channel height curtails the velocity slip at the wall. The difference in the predictions of the two methods in the entrance region also diminishes as the Knudsen number is decreased. This is mainly due to moderate velocity and temperature gradients at the inlet which brings the NSWS/J model predictions closer to the molecular simulation results.

The utilized set of slip/jump boundary conditions consider the individual effect of each species which allows precise simulation of multicomponent gaseous flows. As pointed out in previous sections, for a constant inlet mass flux boundary condition, the inlet gas composition can deviate from a uniform flat profile due to possible upstream diffusion of some species. Therefore, a non–uniform species profile is expected across the channel. For

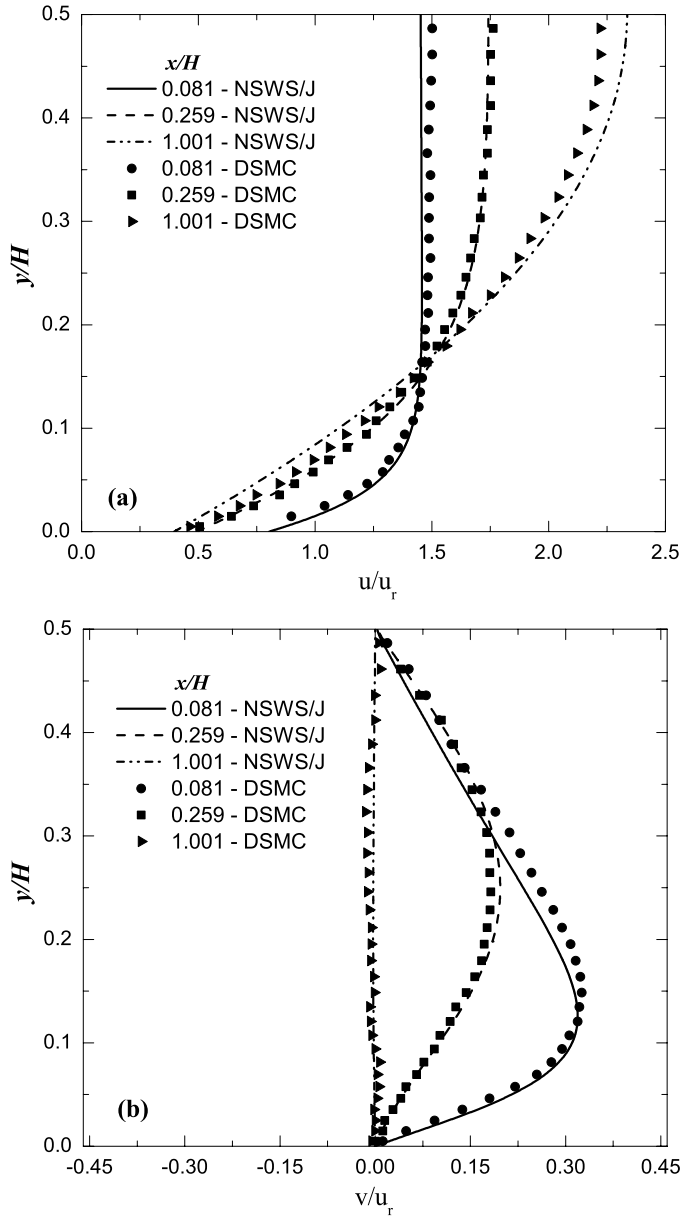

Figure 3.19: Axial (a) and cross–stream (b) velocity distributions across the channel at three axial locations for case 1.

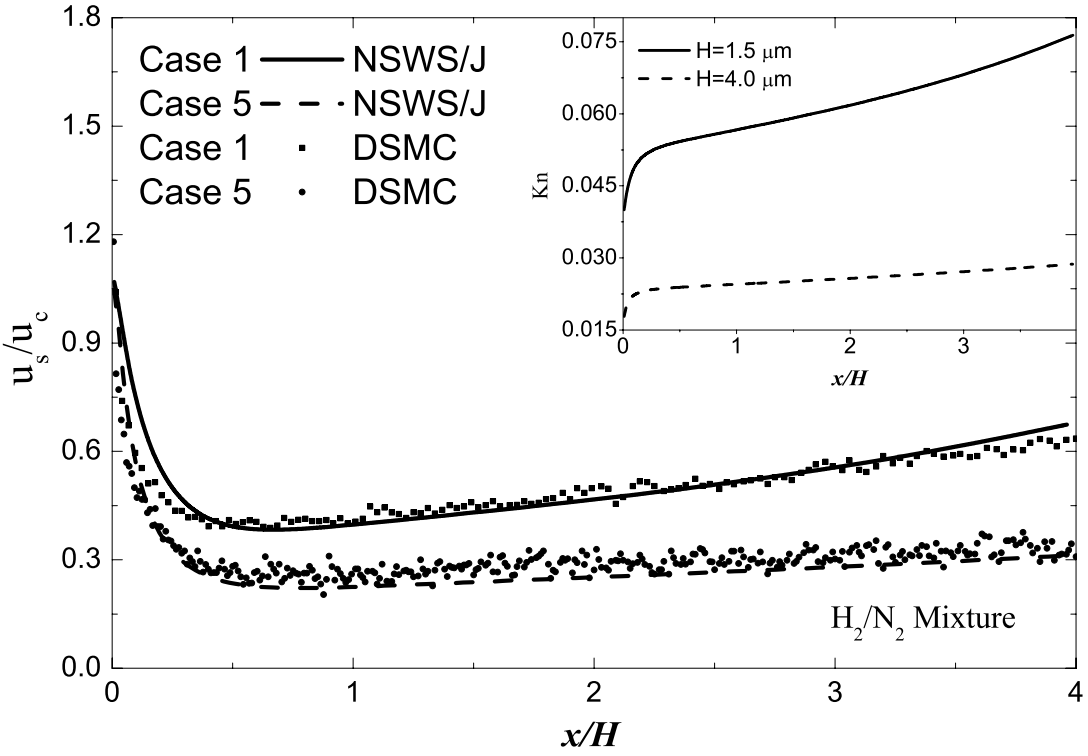

Figure 3.20: Normalized slip velocity and the wall Knudsen number in a $H = 4$ μm channel.

example, the hydrogen and nitrogen mass fractions across the channel are shown in Fig. 3.21 at $x/H = 0.259$ for Case 1. As observed, both methods predict very similar mass fractions across the channel with a maximum relative difference of about 8% and 0.9% for hydrogen and nitrogen mass fractions, respectively. Other axial locations also show similar behavior. A closer view of the nitrogen mass fraction is shown in Fig. 3.21 inset where the non–uniform profile of the nitrogen mass fraction across the channel is more evident. As observed, both methods predict the slightly lower nitrogen mass fraction close to the wall. The difference between the predictions of the two methods remains roughly the same along the channel.

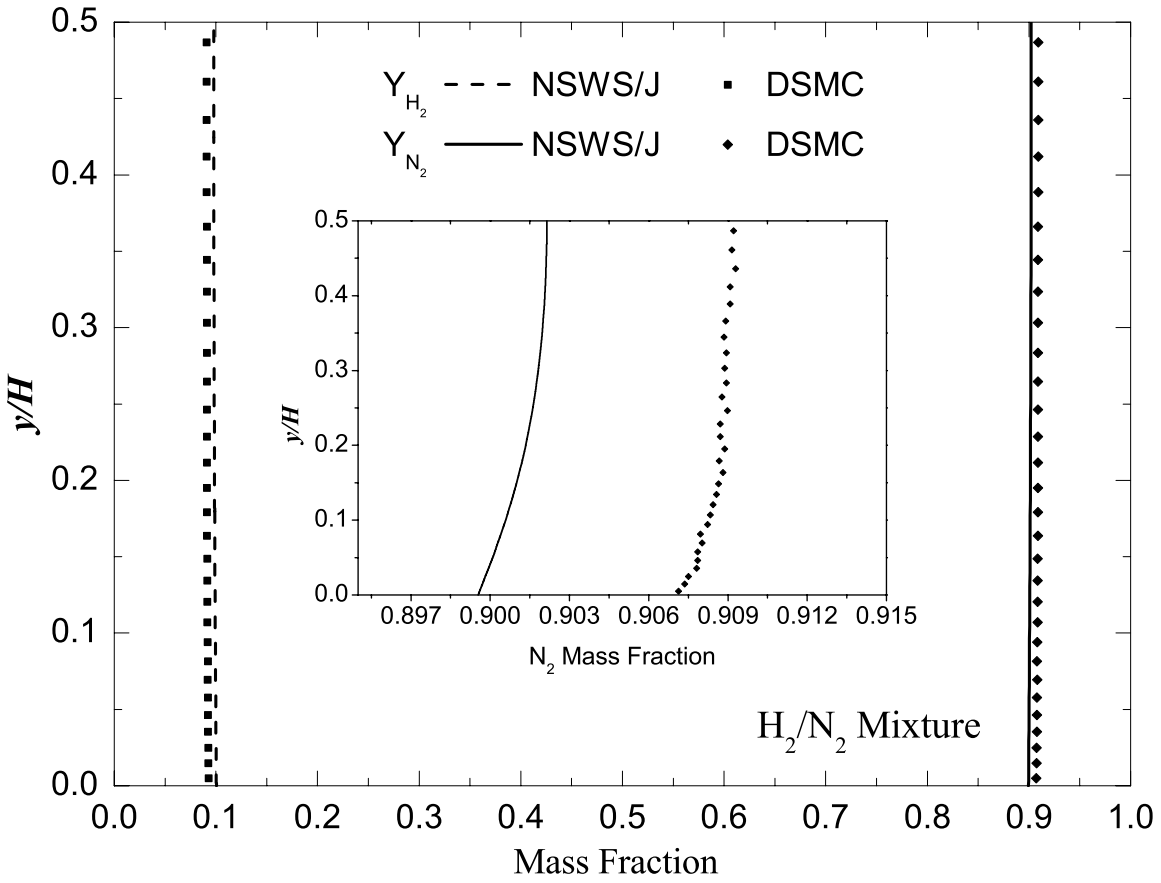

Figure 3.21: Hydrogen and nitrogen mass fractions across the channel at $x/H = 0.259$ for case 1.

This offset between the results is due to the slightly different inlet composition calculations which is carried over into the channel. In the CFD method, the prescribed inlet mass flux (diffusive + convective) can be directly implemented into the finite volume formulation on the inlet cell faces. The DSMC method, however, requires the calculation of inlet species differently. The iterative calculation of the inlet composition in the DSMC method and first order simplifications in the transport equations (compared to the Boltz-

mann equation) yield slightly different inlet values which then propagate into the solution domain [106].

The NSWS/J and DSMC simulation results are in good agreement in multicomponent mixtures as well. The velocity slip predictions of the two methods for the $H_2/N_2/CO_2$ mixture (Case 6) are shown in Fig. 3.22 (a). The species distribution predictions of the two methods across the channel also match at different cross sections. Figure 3.22 (b) shows the cross–stream mass fractions of different species at $x/H = 0.157$. The non–uniform hydrogen distribution close to the wall is also evident in the figure inset. The slight difference between the mass fraction predictions of the two methods is again due to different inlet composition calculations which propagates into the channel.

Heat Transfer

The predictions of temperature jump in both methods are very close along the channel as shown in Fig. 3.23 where the temperature discontinuity at the wall is depicted under different operating condition in a $H = 1.5$ μm channel. Due to steep gradients at the inlet, the temperature discontinuity is the highest in this region and diminishes along the channel. Both methods predict this trend closely with similar numerical values under the considered operating conditions. The maximum difference between the predictions of the two methods is about 6% right at the channel inlet for Case 4 where the wall temperature is the highest.

Figure 3.24 shows the wall heat flux predictions along the channel under the same operating conditions. The wall heat fluxes of Case 1 in both methods are shrunk by a factor of 2 for clarity. In the CFD method, the temperature gradient at the edge of the Knudsen layer and mixture–averaged properties are used to calculate the net heat flux. As

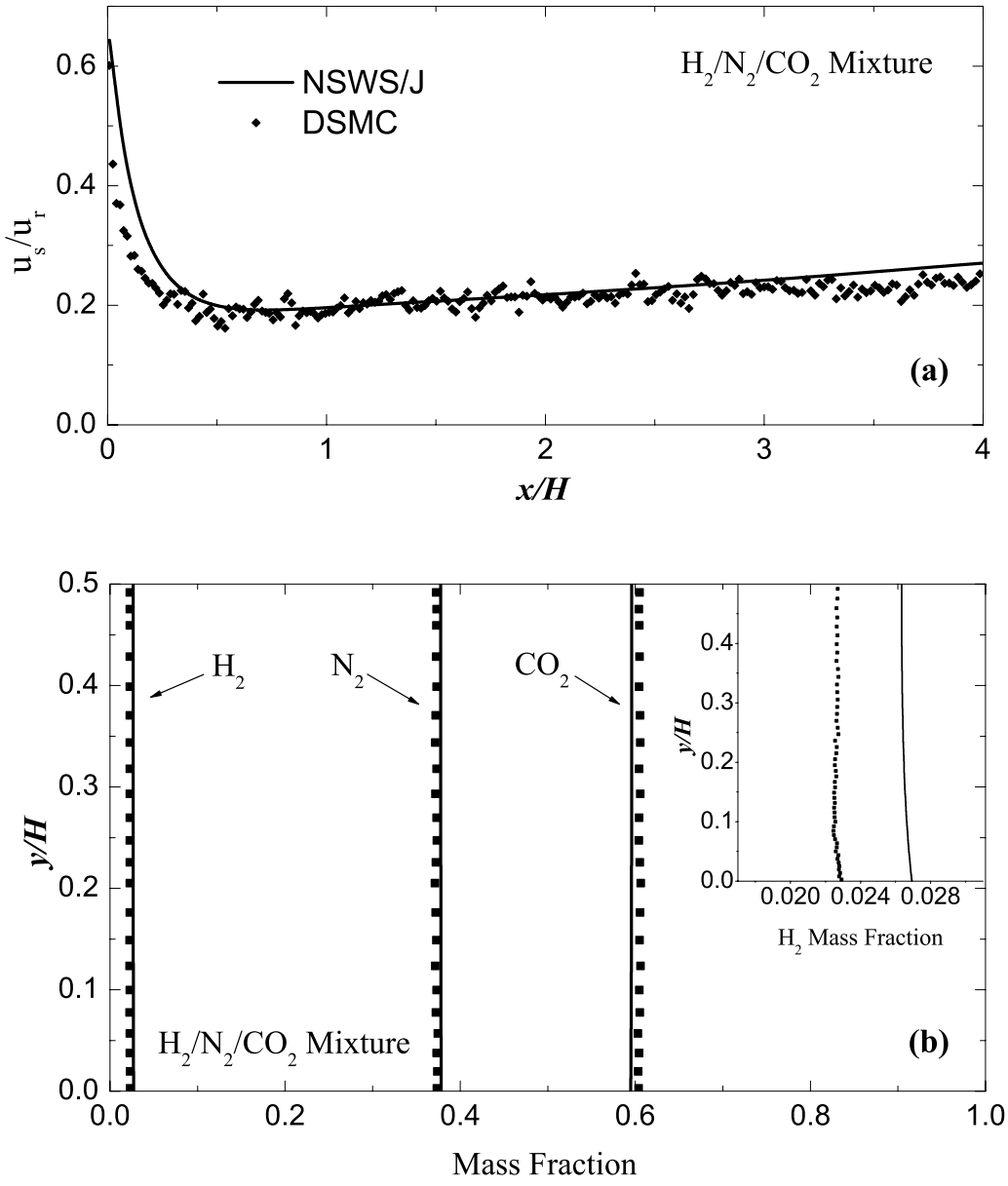

Figure 3.22: Velocity slip (a) and mass fractions of different species at $x/H = 0.157$ (b) for the $H_2/N_2/CO_2$ mixture (case 6); solid lines: NSWS/J, squares: DSMC.

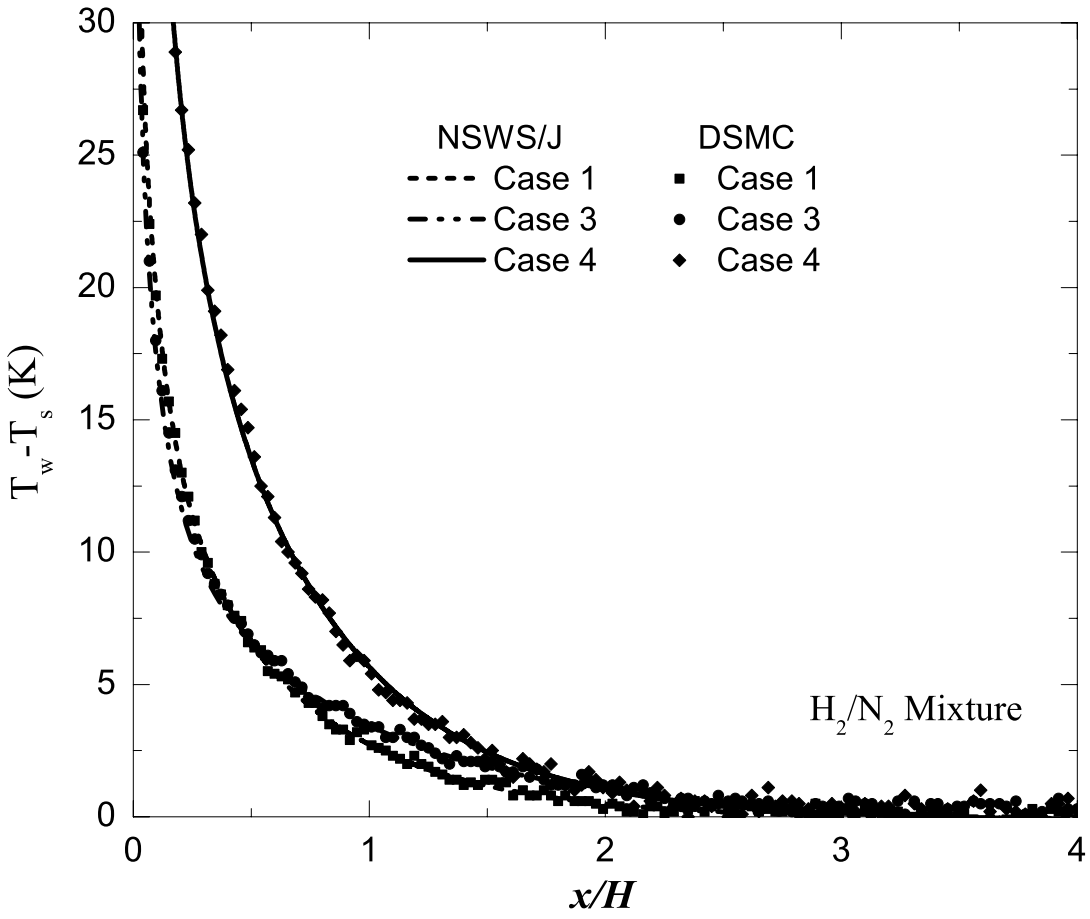

Figure 3.23: Temperature discontinuity at the edge of the Knudsen layer under different operating conditions.

observed, the simulation results of the two methods are generally in a very good agreement under these operating conditions. An increased inlet mass flux reduces the uncertainty due to scattering in the DSMC method and the wall heat fluxes of the methods become closer. In Case 4, the increased temperature gradient at the wall (and consequently the wall Knudsen number) results in slight deviation between the two methods, although the maximum difference remains below 10%.

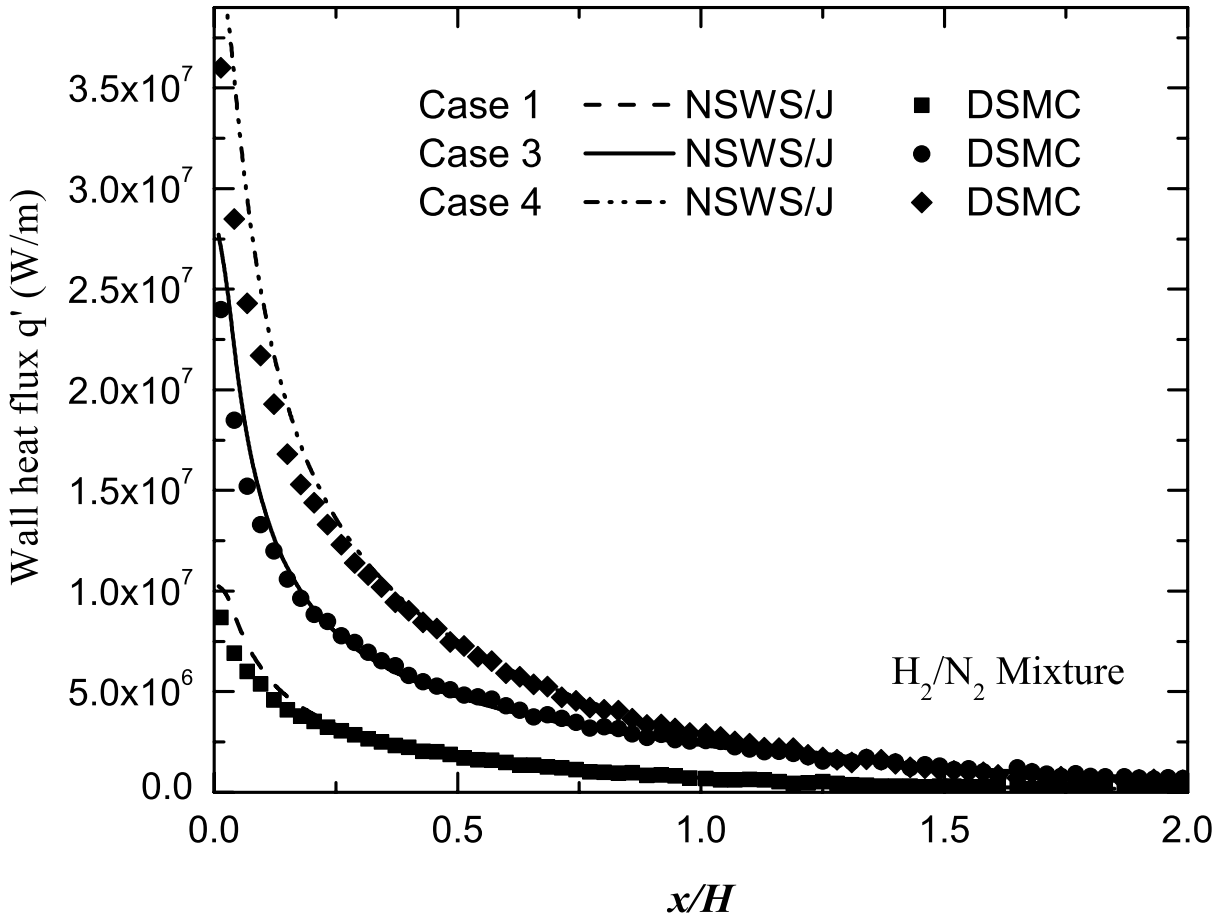

Figure 3.24: Wall heat flux along the channel under different operating conditions; The results of case 1 are multiplied by 0.5 to avoid cluttering.

High statistical scattering associated with DSMC results is another reason behind the discrepancy in predictions of these two methods. This effect is more pronounced in low velocity flows. The presence of statistical scattering particularly at the channel inlet and outlet prevents the effective implementation of prescribed boundary values such as species mass fluxes which causes different simulation results in these regions [106].

3.3.4 Conclusion

The implemented multicomponent velocity slip boundary condition is in good agreement with the analytical and molecular simulation results. The velocity slip predictions in an isothermal channel closely follow the high order analytical predictions in the developed region of the channel. It has also been shown that the axial temperature gradient at the edge of the Knudsen layer in the utilized velocity slip boundary condition is of secondary importance and is only important in the entrance region where the gradients are the highest. As the velocity and temperature gradients increase (with an increase in the wall temperature or the inlet mass flux) the slip model simulation results start to deviate from the DSMC predictions in the channel inlet within a reasonable tolerance. A decrease in the Knudsen number generally brings the simulation results closer together everywhere in the channel. The mass fractions of species within the solution field also match closely. The mass fraction field in the continuum model shows an almost constant offset across the channel compared to DSMC results. This deviation is mainly due to non–matching inlet composition calculations which carries over into the solution domain.

The predicted temperature discontinuity at the edge of the Knudsen layer shows a very good agreement with the molecular simulations as well. The change in the operating conditions does not seem to affect the accuracy of the temperature jump model as the results match closely under all operating conditions. The predicted wall heat fluxes show a slight discrepancy very close to the inlet; however the results from both methods quickly merge together along the channel. The differences are more apparent at higher Knudsen numbers.

Chapter 4

Contribution of homogeneous reactions to hydrogen oxidation in catalytic microchannels

4.1 Introduction[1]

In recent years, there has been intensive research on microfluidic systems for compact reactor technologies. Investigations have been conducted to better understand and predict the flow, heat transfer and mass transfer properties of so–called microreactors. As the characteristic size decreases, heat and mass transfer at the walls play an important role in defining the combustion characteristics of such systems [66]. The increased heat and radical losses at the walls can suppress homogeneous reactions to a great extent. In order to maintain stable combustion in the gas phase useful strategies such as Swiss–Roll

[1] A brief version of this section including some figures is published as an article in the Combustion and Flame, 2012, Vol. 159, 784-792.

and Heat–Recirculating burners [2, 50] have been proposed. Several other studies have been conducted to sustain homogeneous combustion in sub–millimetre burners. Miesse et al. [65] showed that by chemically treating the vessel walls, gas–phase combustion of methane/oxygen is achievable in sub–millimetre sizes. Also, it was shown that the flame structure is not similar to what is expected in a macro–structured configuration under similar conditions. Spadaccini et al. [89] reported sustainable propane–air reactions in catalytically stabilized sub–millimeter conduits.

Along with experimental studies, several numerical simulations have also been performed in order to study the behaviour of different fuels, the role of heat loss and radical quenching, and wall material on homogeneous combustion [73]. Aghalayam et al. [1] numerically investigated the role of wall quenching of radicals on the extinction behavior of hydrogen/air mixtures in a stagnation–point geometry. It was proposed that in general, the radical quenching on the wall hinders the homogeneous reactions; however, the heat release due to the catalytic surface reactions can reduce this effect. Raimondeau et al. [79] modeled methane flame propagation inside tubular microchannels. The near entrance heat and radical quenching were identified as the main factors controlling flame propagation in these channels which could be controlled by proper insulation and preheating. Maruta et al. [60] numerically studied the extinction limits of self–sustaining methane/air combustion on Platinum in a cylindrical tube. They showed that when heat losses exist, i.e. non–adiabatic walls, the extinction limits are due to blow–off at high inlet velocities and heat–loss–extinction at low inlet velocities similar to ordinary gas phase combustion.

Heat transfer characteristics of premixed stoichiometric hydrogen/air combustion inside cylindrical chambers of different dimensions were numerically studied by Hua et al. [43]. They concluded that thermal management of micro–chambers can significantly improve the combustion stability and lead to the design of practical micro–combustors. Leach et

al. [55] performed a 1D numerical analysis of the effects of heat losses on the reaction zone thickness in H_2 combustors. They also presented an analytic model for the prediction of reaction zone thickness based on the channel size and thermal properties of the structure. The broadening reaction zone was attributed to the heat exchange between the reacting mixture and the channel walls with thicker reaction zone in channels of higher conductivities. Karagiannidis et al. [45] studied the combustion characteristics of fuel–lean methane/air mixtures in a Pt–coated planar geometry. The presence of catalytic walls is reported to expand the stability limits of gas phase combustion in micro conduits. The positive effect of exothermic surface reactions on the stability of gas phase reaction is highlighted in their work. Li et al. [57] performed a numerical analysis involving combustor size, geometry and boundary conditions to study their effects on the flame temperature of premixed methane/air mixtures. Their findings suggest that a fully–developed inlet velocity profile stabilizes the flame within the chamber.

As discussed in previous studies, key parameters such as the fuel–air equivalence ratio, the mixture temperature, the flow rate, heat losses to the wall and wall thermal conductivity play an important role in defining the interaction between the gas phase and catalytic reactions. The effects of these parameters can also be very different as the channel size is reduced. In this chapter, the relative importance of gas phase and surface reactions associated with hydrogen oxidation at different inlet mass fluxes, equivalence ratios and channel heights are assessed for lean H_2/air mixtures in planar microchannels. Detailed gas phase and surface reaction mechanisms are employed in order to fully account for the effects of minor species in determining the homogeneous and heterogeneous reaction pathways.

4.2 Problem statement

A schematic view of channel geometry and the coordinate system are shown in Fig. 3.11. The governing mass, momentum, energy, and species continuity equations are described in section 2.1. Detailed gas phase and surface reaction mechanisms along with a multi–component species diffusion model are used. These equations were discretized using the colocated finite volume method. The mixture transport properties as well as the pure species properties are obtained using the CHEMKIN database [47]. The homogeneous production rates in the conservation equations are modeled using a detailed gas phase reaction mechanism due to Maas and Warnatz [59] involving nine gas phase species as shown in Table 4.1. Also, a detailed surface reaction mechanism proposed by Deutschmann et al. [23], shown in Table 4.2, with five surface species is adopted in the present work in order to model hydrogen oxidation on platinum.

Since a large number of variables can change in this type of problem, some parameters are kept constant in order to make a meaningful comparison between different cases. To this end, the inlet mass flux of each species is assumed to be constant. This constraint forces the overall inlet mass flux to remain constant as well. This approach is especially useful when dealing with low Péclet number ($\mathrm{Pe}_k = \mathrm{ReSc}_k$, where Sc is the Schmidt number) flows in which the inlet diffusion mass flux can be significant. In such a case, the inlet mass flux of each species $\vec{\dot{m}}_k = \rho Y_k \mathbf{U} + \mathbf{J}_k$ can be utilized to determine the relative contribution of the diffusion and convection mass fluxes. This will be further explained in the results section. The surface site density is specified to be $\Gamma = 2.7 \times 10^{-5}$ mole/m^2 simulating a polycrystalline platinum coating on the wall [23]. The inlet gas temperature is assumed to be 300 K while the wall temperature T_w is maintained at 1450 K. The selected wall temperature ensures enough gas phase contribution to hydrogen oxidation in the range of

Table 4.1: Gas phase reaction mechanism of hydrogen-oxygen [59]

No.	Reaction	A^a [mol, sec, cm]	b -	E_a [kJ/mol]
G1	$O_2 + H \rightleftharpoons OH + O$	2.00×10^{14}	0.0	70.30
G2	$H_2 + O \rightleftharpoons OH + H$	5.06×10^{4}	2.7	26.30
G3	$H_2 + OH \rightleftharpoons H_2O + H$	1.00×10^{8}	1.6	13.80
G4	$OH + OH \rightleftharpoons H_2O + O$	1.50×10^{9}	1.1	0.42
G5	$H + H + M \rightleftharpoons H_2 + M^b$	1.80×10^{18}	-1.0	0.00
G6	$O + O + M \rightleftharpoons O_2 + M$	2.90×10^{17}	-1.0	0.00
G7	$H + OH + M \rightleftharpoons H_2O + M$	2.20×10^{22}	-2.0	0.00
G8	$H + O_2 + M \rightleftharpoons HO_2 + M$	2.30×10^{18}	-0.8	0.00
G9	$HO_2 + H \rightleftharpoons OH + OH$	1.50×10^{14}	0.0	4.20
G10	$HO_2 + H \rightleftharpoons H_2 + O_2$	2.50×10^{13}	0.0	2.90
G11	$HO_2 + H \rightleftharpoons H_2O + O$	3.00×10^{13}	0.0	7.20
G12	$HO_2 + O \rightleftharpoons OH + O_2$	1.80×10^{13}	0.0	-1.70
G13	$HO_2 + OH \rightleftharpoons H_2O + O_2$	6.00×10^{13}	0.0	0.00
G14	$HO_2 + HO_2 \rightleftharpoons H_2O_2 + O_2$	2.50×10^{11}	0.0	-5.20
G15	$OH + OH + M \rightleftharpoons H_2O_2 + M$	3.25×10^{22}	-2.0	0.00
G16	$H_2O_2 + H \rightleftharpoons H_2 + HO_2$	1.70×10^{12}	0.0	15.70
G17	$H_2O_2 + H \rightleftharpoons H_2O + OH$	1.00×10^{13}	0.0	15.0
G18	$H_2O_2 + O \rightleftharpoons OH + HO_2$	2.80×10^{13}	0.0	26.80
G19	$H_2O_2 + OH \rightleftharpoons H_2O + HO_2$	5.40×10^{12}	0.0	4.20

[a] Arrhenius parameters for reaction rate constants: $k_f = AT^b \exp(-E_a/RT)$.
[b] Third body enhancement factors: $\omega(H_2O) = 6.5$, $\omega(O_2) = \omega(O_2) = 0.4$ in reactions 5, 6, 7, 8, 15.

Table 4.2: Surface reaction mechanism of hydrogen oxidation on platinum [23]

No.	Reaction	A^a or γ [mol, sec, cm]	E_a [kJ/mol]
S1	$H_2 + 2\,Pt(s) \longrightarrow 2\,H(s)^{b,c}$	0.046	-
S2	$H + Pt(s) \longrightarrow H(s)$	1.0	-
S3	$O_2 + 2\,Pt(s) \longrightarrow 2\,O(s)$	0.07^c	-
S4	$O + Pt(s) \longrightarrow O(s)$	1.0	-
S5	$H_2O + Pt(s) \longrightarrow H_2O(s)$	0.75	-
S6	$OH + Pt(s) \longrightarrow OH(s)$	1.0	-
S7	$H(s) + O(s) \longrightarrow OH(s) + Pt(s)$	3.7×10^{21}	11.5
S8	$OH(s) + Pt(s) \longrightarrow H(s) + O(s)$	3.7×10^{21}	24.5
S9	$H(s) + OH(s) \longrightarrow H_2O(s) + Pt(s)$	3.7×10^{21}	17.5
S10	$H_2O(s) + Pt(s) \longrightarrow H(s) + OH(s)$	3.7×10^{21}	113.5
S11	$OH(s) + OH(s) \longrightarrow H_2O(s) + O(s)$	3.7×10^{21}	48.2
S12	$H_2O(s) + O(s) \longrightarrow OH(s) + OH(s)$	3.7×10^{21}	131.4
S13	$2\,H(s) \longrightarrow H_2 + 2\,Pt(s)$	3.7×10^{21}	$67.4 - 6Z_H$
S14	$2\,O(s) \longrightarrow O_2 + 2\,Pt(s)$	3.7×10^{21}	$213.2 - 60Z_O$
S15	$H_2O(s) \longrightarrow H_2O + Pt(s)$	1.0×10^{13}	40.3
S16	$OH(s) \longrightarrow OH + Pt(s)$	1.0×10^{13}	192.8

[a] Arrhenius parameters for reaction rate constants: $k_f = A\exp(-E_a/RT)$.
[b] (s) denotes surface-adsorbed species.
[c] Hydrogen adsorption reaction is first order with respect to Platinum. The Oxygen sticking coefficient has a temperature dependence of the form $\gamma_{O_2} = 0.07(T_0/T)$ with $T_0 = 300$K.

operating conditions considered here. The equivalence ratio of the mixture is also specified at the inlet for each case. The flow is mass driven such that the mass flux of each species is uniform across the channel inlet. The outlet pressure is assumed to be atmospheric. In the range of channel heights and operating conditions considered in this chapter, slip/jump effects on the wall are negligible and no–slip boundary conditions are employed on the channel walls.

For the low Péclet number values used in this study, numerical simulations showed that a channel length of about $4H$ is sufficient for for all the variables to develop. In the present work, a channel length of $L = 10H$ is considered for all simulations. The solution domain is discretized using an orthogonal non–uniform grid distribution. Grid point density is higher near the wall and channel inlet since the highest gradients are expected in these regions. Different mesh sizes were examined in order to test the grid independence of the results. A mesh size of 140×24 (with an expansion ratio of 1.02 and 1.025 in the x and y directions, respectively) yields grid–independent results. Also, since the channel geometry and boundary conditions are symmetric, only half of the channel is simulated numerically.

4.3 Results and discussion

The effects of channel height, inlet mass flux and mixture equivalence ratio on the gas phase contribution to hydrogen oxidation are studied in this section. In order to study the gas phase reaction contribution to hydrogen oxidation under different operating conditions, two of these parameters are kept constant while the third one is varied.

4.3.1 Channel height effect

As the channel size decreases, the heat and mass transfer rates generally increase. This, in turn, can affect the gas phase reaction rate to a great extent. In order to study the direct effect of channel size on gas phase reactions, the inlet mass flow rate per unit area ($\dot{m}'' = 0.355$ kg/m^{2}s), the wall temperature ($T_w = 1450$ K) and the inlet equivalence ratio ($\varphi = 0.45$) are kept constant in simulating channels of different heights. The hydrogen conversion rate, integrated over channel half–height, along channels of different heights is plotted in Fig. 4.1. The gaseous conversion rates are integrated (not averaged) across the channel height to have the same dimension (mol/m^{2}s) as their catalytic counterparts when comparing their relative importance to the overall hydrogen conversion. The gas phase conversion rate decreases with decreasing channel height. Initially, as the channel height is reduced from 1000 μm to 600 μm, the gas phase conversion rate gradually decreases, mainly due to the reduced channel volume. The heterogeneous H_2 conversion rate remains essentially constant in this range of channel heights. However, as the channel size is further reduced, there is a sheer drop in the gas phase H_2 conversion rate. The catalytic H_2 conversion rate also increases for channel heights below 600 μm due to reduced gas phase conversion rate.

The OH destruction rate at the wall also exhibits an interesting trend as shown in Fig. 4.2. As the channel size is reduced from 1000 μm to 600 μm the OH destruction rate on the wall remains almost constant despite the reduced OH levels in the gas phase. In order to assess the impact of wall radical destruction on the gas phase reaction inhibition, the following reactions (OH adsorption/desorption reactions) are removed from the surface mechanism:

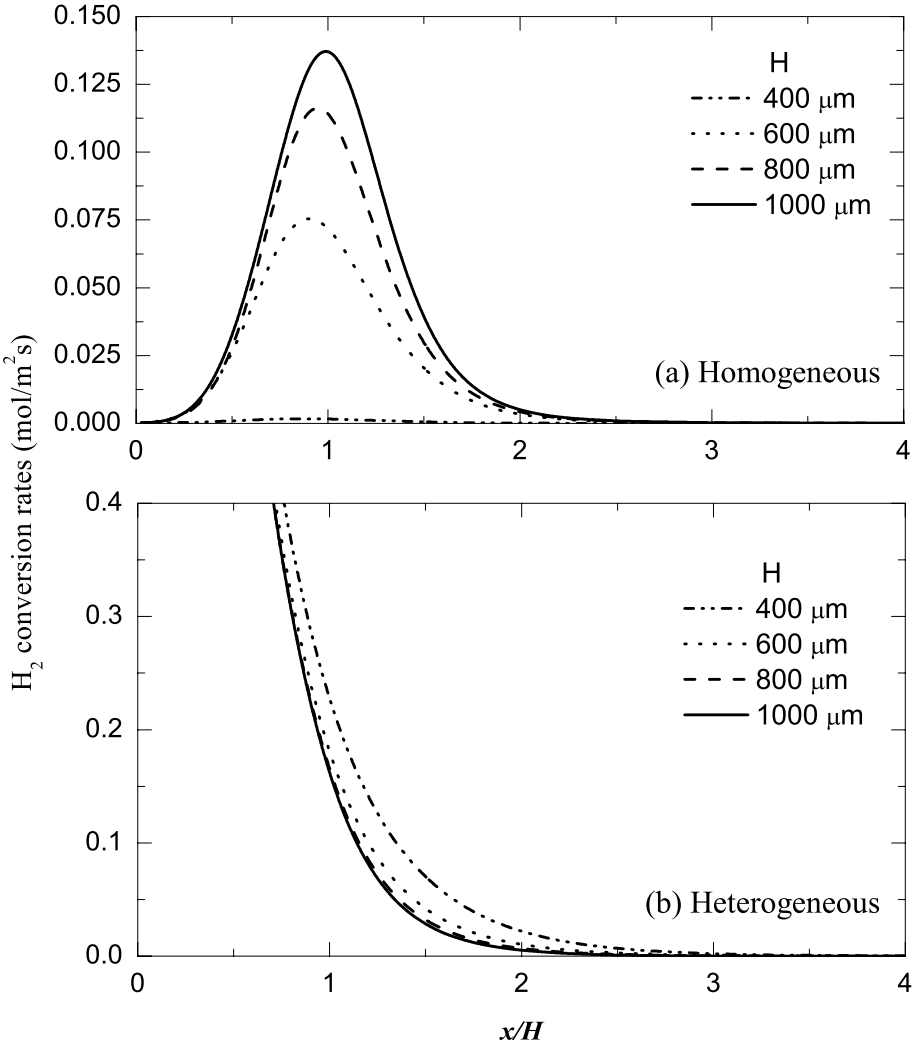

Figure 4.1: (a) Gas phase (integrated over channel half-height) and (b) catalytic conversion rates of H_2 at different channel heights.

$$\mathrm{OH} + \mathrm{Pt(s)} \longrightarrow \mathrm{OH(s)} \tag{4.1a}$$

$$\mathrm{OH(s)} \longrightarrow \mathrm{OH} + \mathrm{Pt(s)} \tag{4.1b}$$

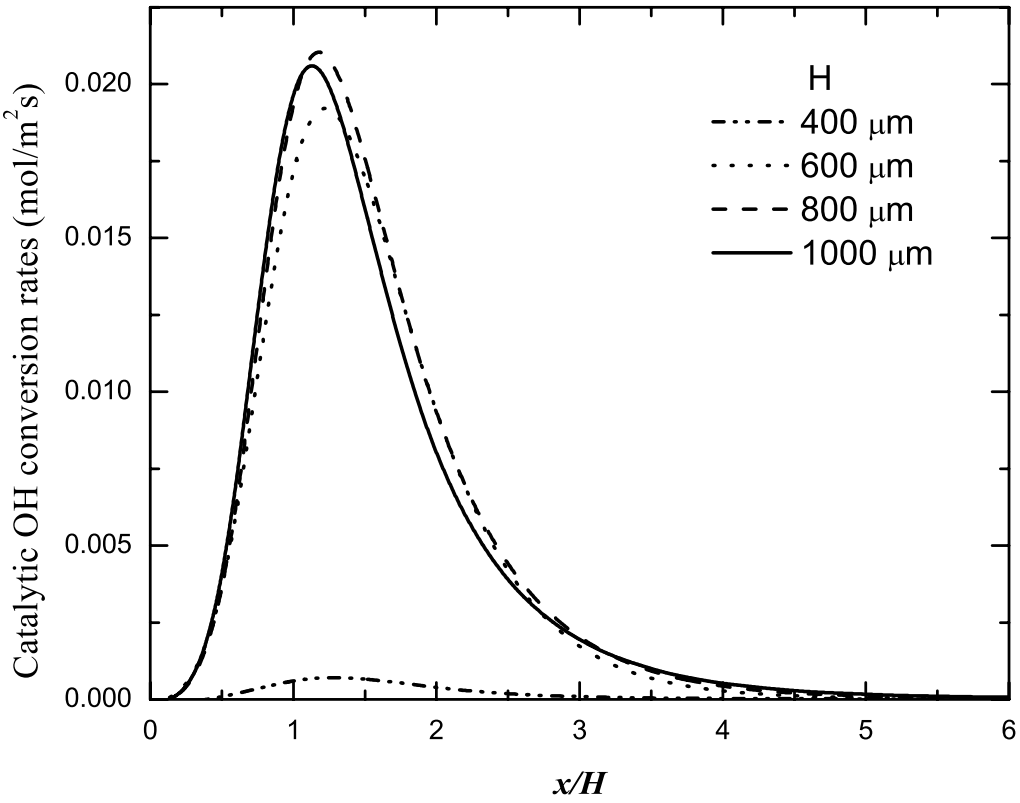

Figure 4.2: Streamwise catalytic conversion rate of OH at different channel heights.

where (s) denoted surface–adsorbed species. The results are depicted in Fig. 4.3 where the gas phase conversion rates are compared to the normal simulations for channel heights of 400 μm to 1000 μm. The OH radical destruction on the wall considerably inhibits the gaseous reaction rates. In the case of the 600 μm channel, for instance, the maximum homogeneous H_2 conversion rate increases by about 47% when the OH adsorption/desorption reactions are excluded from the reaction mechanism. This effect is even more pronounced for the 400 μm channel. However, as the channel size increases, the wall radical destruction effect becomes less important. This can be observed in Fig. 4.3 (b) where the homogeneous hydrogen conversion rates are compared with and without OH adsorption/desorption reac-

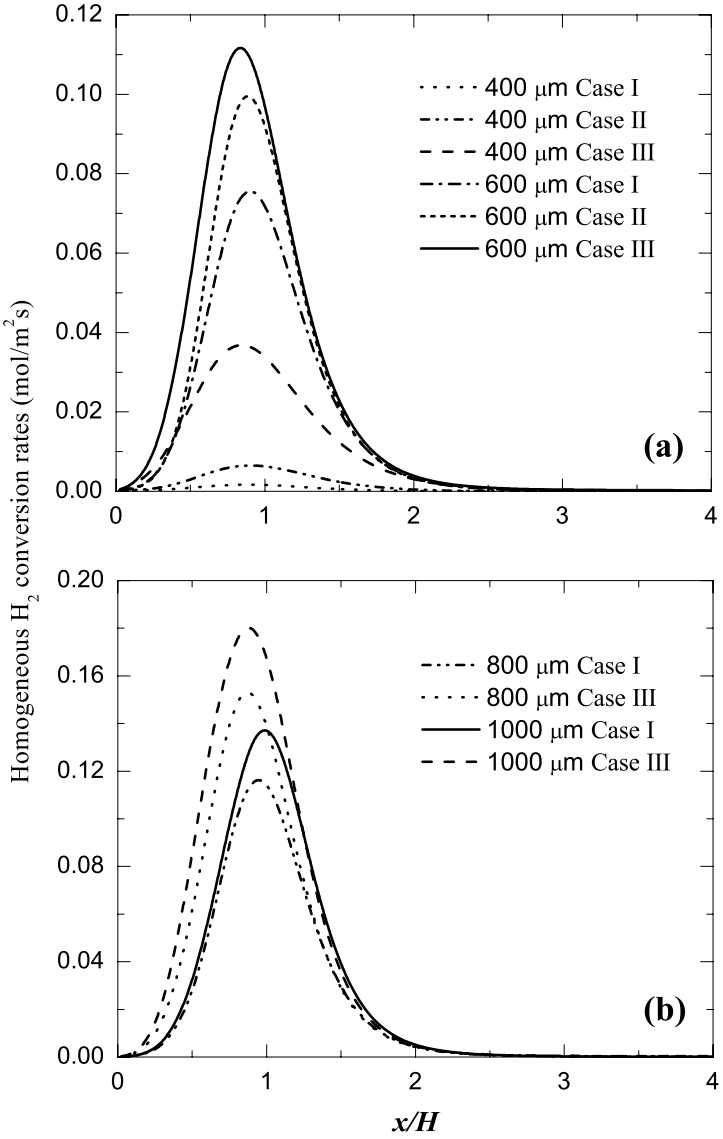

Figure 4.3: Gas phase (integrated over channel half-height) conversion rates of H_2 at two different channel heights; Case I: Normal simulation results; Case II: Lower H_2O effect in gaseous reaction mechanism (artificial H_2O third-body enhancement coefficient reduction); Case III: OH adsorption/desorption surface reactions are removed from surface reaction mechanism.

tions on the wall. Due to the inhibiting effect of OH destruction on the wall, the maximum homogeneous H_2 conversion rate increases by about 32% and 30% for the 800 μm and 1000 μm channels, respectively, when the adsorption/desorption reactions are removed. As observed, the OH adsorption/desorption reactions are mostly important in smaller channels, and as the channel height increases, this effect gradually diminishes. The axial location where the maximum gas phase H_2 conversion occurs is however not sensitive to the wall OH adsorption/desorption reactions and is only slightly shifted upstream.

Besides the radical destruction on the wall, the suppression of the hydrogen oxidation in the gas phase can be further analyzed by observing the inlet mixture composition. The inlet mass flux of each species, which is held constant, consists of the diffusion mass flux and the convective mass flux of that species. As the channel size is reduced, the diffusive mass transfer generally becomes more effective. Since hydrogen is consumed in the channel, right at the inlet there exists a positive diffusive mass flux of hydrogen into the channel. In order to keep the total inlet mass flux constant, the inlet mass fraction of the hydrogen should be adjusted (lowered) accordingly. This way the total inlet mass flux of hydrogen, $\vec{\dot{m}}''_{H_2} = \rho Y_{H_2}\mathbf{U} + \mathbf{J}_{H_2}$ remains constant. The same scenario also applies to the oxygen. However, since hydrogen molecules are much faster than oxygen, this effect is more pronounced for hydrogen. On the other hand, the H_2O produced in the channel can also diffuse back towards the inlet, which results in a negative diffusive mass flux of H_2O out of the channel. Since the total mass flux of H_2O (diffusion + convection) is set equal to zero in the simulations, this outgoing H_2O mass flux should be balanced by the incoming convective flux of H_2O, i.e. $\rho Y_{H_2O}\mathbf{U}$, at the inlet. Therefore a finite amount of H_2O will exist at the channel inlet, despite the fact that the inlet H_2O mass flux is zero. As stated earlier, the diffusion flux becomes stronger as the channel size is reduced, which intensifies this process. At each iteration, the inlet mass fraction of all species Y_k

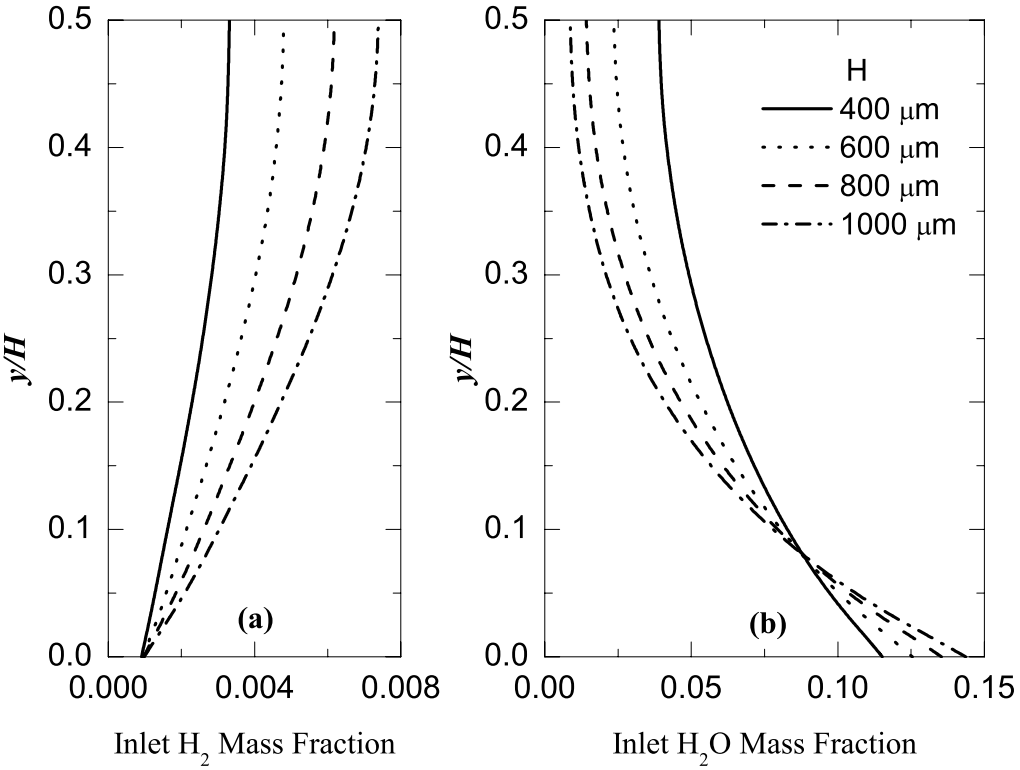

Figure 4.4: Inlet (a) H_2 and (b) H_2O mass fractions for different channel heights.

and the mass–averaged inlet velocity $\mathbf{U}$ are calculated using $\vec{m}_k'' = \rho Y_k \mathbf{U} + \mathbf{J}_k = \text{const}$ (N_g constraints) along with $\sum_{k=1}^{N_g} Y_k = 1$. The diffusive fluxes of species $\mathbf{J}_k$ are calculated from the previous iteration.

The inlet mass fractions of H_2 and H_2O for different channel heights are shown in Fig. 4.4. As the channel height is reduced, the inlet H_2 mass fraction generally decreases across the channel because of stronger diffusive mass flux specially in regions close to the wall while the average inlet H_2O mass fraction increases as a consequence of stronger diffusion effect at lower heights. However, unlike the monotonic trend observed in the inlet H_2 mass fraction distribution across the channel, the inlet H_2O mass fraction in the vicinity of the

wall is higher in larger channels. This behaviour is due to the relatively smaller diffusion coefficient of H_2O as compared to H_2. The diffusive flux is responsible for the removal of the produced H_2O from the wall. In larger channels, the diffusive flux is not strong enough to wash away the reaction products from the wall, and therefore, a considerable difference exists between the mid-plane and wall H_2O mass fractions right at the channel inlet. The reduction in channel height enhances the diffusive transfer of wall products to the gas phase which in turn, as observed, reduces the difference between the gas phase and wall H_2O mass fractions. This increase in the product and decrease in fuel levels at the inlet alters the reaction rates.

Ghermay et al. [31] and Bui et al. [13] have demonstrated that the presence of water in the mixture inhibits gaseous combustion. As a chain terminating reaction, $H + O_2 + M \rightleftharpoons HO_2 + M$ is an important step in the ignition process as discussed in [98, 13]. As a third-body species, H_2O promotes this reaction where active H atoms react with O_2 molecules producing relatively inert HO_2 radicals. In order to assess the H_2O–induced suppression effect on the gas phase conversion rate, the H_2O enhancement factor $\omega(H_2O)$ relative to O_2 is reduced from 16.25 to 1 by reducing $\omega(H_2O)$ from 6.5 to 0.4. The gas phase H_2 conversion rates with and without this artificial adjustment of the enhancement factor are shown in Fig. 4.3. As observed, the presence of H_2O suppresses the gaseous hydrogen conversion. For instance, in the 600 μm channel, the peak value of the hydrogen conversion in the gas phase is about 30% greater in the artificially adjusted $\omega(H_2O)$ case compared to the normal simulation results. However, at the smallest examined channel height, the H_2O–induced suppression of the gas phase reaction is much smaller than the wall OH destruction effect.

The mid–plane temperature profiles along the channel at different channel heights are shown in Fig. 4.5. Due to stronger diffusion effect at smaller channel heights, the mid–

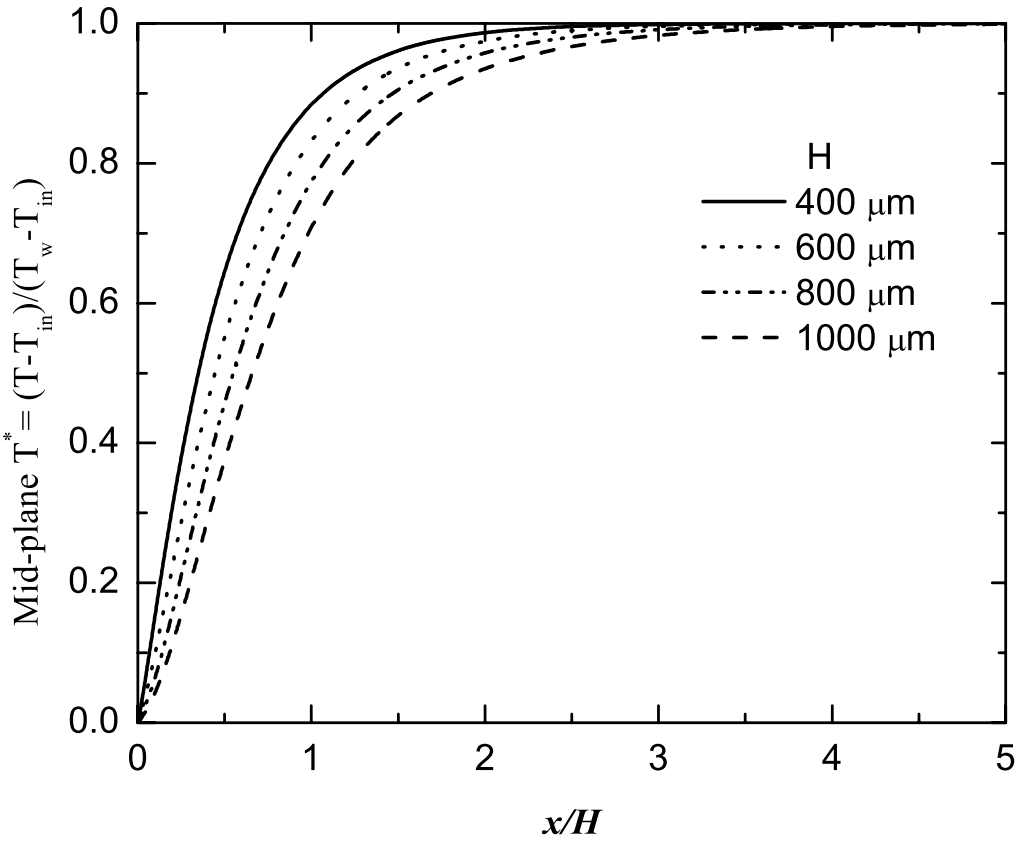

Figure 4.5: Non–dimensional mid-plane temperature T^* at different channel heights.

plane temperature increases as the channel height is decreased. Elevated temperatures promote gas phase conversion since the reaction rates are strong functions of temperature. However, as observed earlier, the temperature variation due to channel size change does not seem to have a considerable influence on the the gas phase conversion rate. In other words, the rise in gas temperature due to smaller channel size is not strong enough to compete with other suppressing effects.

4.3.2 Mass flux variation

In order to study the effect of mass flow rate on the gas phase reaction rate, the inlet mass flux in a $H = 700\ \mu m$ channel is varied while keeping the wall temperature $T_w = 1450$ K and the inlet equivalence ratio $\varphi = 0.45$ constant. The change in the inlet mass flux alters the relative importance of convective and diffusive mass fluxes which can affect the behaviour of the reactive flow. Figure 4.6 shows the streamwise profile of H_2 conversion rate in the gas phase (integrated over channel half-height) as well as the catalytic H_2 conversion rate on the wall. Starting at a relatively weak level, the gas phase H_2 conversion rate initially increases as the inlet mass flux is increased and then diminishes as the inlet mass flow rate is further increased.

The catalytic conversion rate, however, increases as the inlet mass flow rate is increased. The surface site fraction of H(s) and H_2O(s) are plotted in Fig. 4.7 along the channel at different inlet mass fluxes. At higher inlet mass fluxes, more fuel can be delivered to the wall for catalytic conversion which as expected results in higher levels of H(s) and H_2O(s) surface coverages on the wall. The increased catalytic conversion rate inhibits the gas phase reaction at higher inlet mass fluxes despite a higher inlet hydrogen supply. This can be readily observed in Table 4.3 where the relative contribution of the gas phase and catalytic conversion rates to the overall available hydrogen for oxidation are given. In all cases, the catalytic conversion dominance in hydrogen conversion is apparent. The hydrogen supply to the channel increases linearly as the inlet mass flux is increased while the relative contribution of the gas phase H_2 conversion rapidly decreases to negligible levels. It is, however, interesting to note that the amount of homogeneous H_2 conversion (in kg/s) initially increases as the inlet mass flux is increased to 0.274 kg/m^{2}s and then decreases again with further increase in the inlet mass flux. Because of highly non–linear

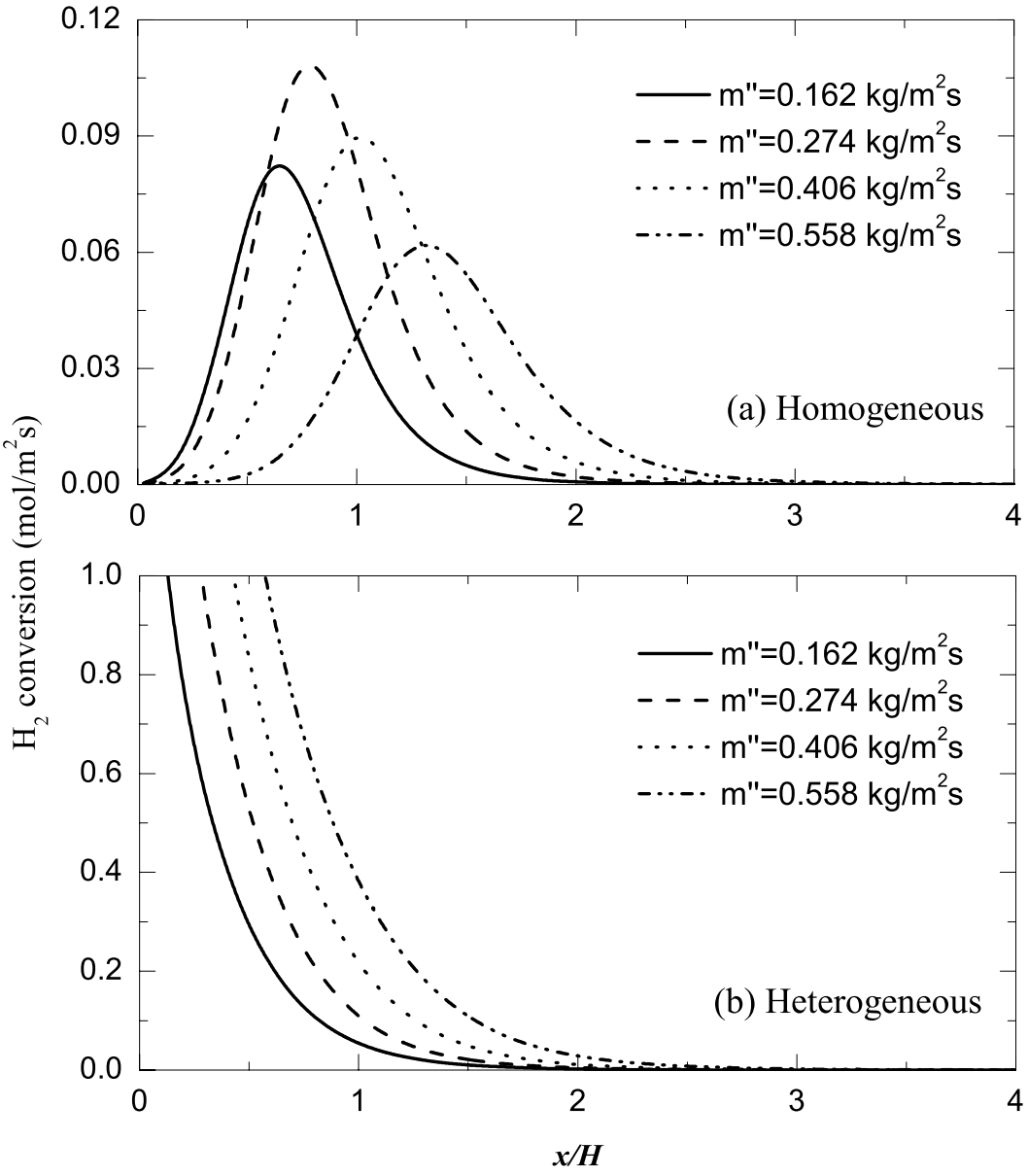

Figure 4.6: (a) Gas phase (integrated over channel half–height) and (b) catalytic H_2 conversion rates at different inlet mass flow rates along a $H = 700\ \mu m$ channel with $T_w = 1450$ K.

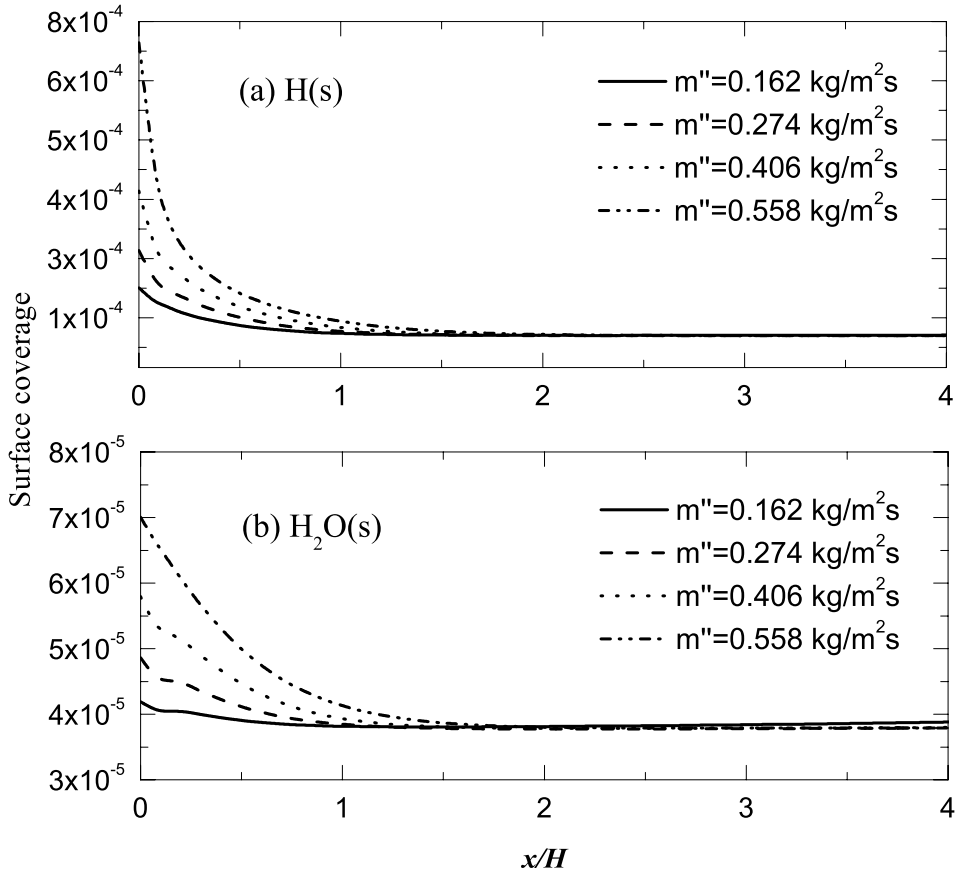

Figure 4.7: Surface site fraction of (a) H(s) and (b) H_2O(s) along a $H = 700\ \mu m$ channel with $T_w = 1450$ K at different inlet mass fluxes.

interactions between the diffusion and convection fluxes, transport properties and gas phase and wall chemistry, one should not expect a linear behavior in the catalytic conversion rate.

Figure 4.8 depicts the cross–stream hydrogen mass fraction profiles at axial locations where the homogeneous conversion rate peaks for the above–mentioned inlet mass fluxes. The trend observed in the available hydrogen for homogeneous reaction in the channel is consistent with the contribution of homogeneous hydrogen conversion observed in Fig.

Table 4.3: Homogeneous and heterogeneous conversion rates at different inlet mass fluxes along a $H = 700\ \mu m$ channel.

$\dot{m}''$ (kg/m^{2}s)	0.162	0.274	0.406	0.558
$\dot{m}_{H_2}$ inlet ($\times 10^6$ kg/s)	0.736	1.241	1.839	2.528
Gas Conv. ($\times 10^6$ kg/s)	0.077	0.109	0.103	0.080
Cat. Conv. ($\times 10^6$ kg/s)	0.659	1.132	1.735	2.448
% Gas Contribution	10.4	8.7	5.6	3.1
% Catal Contribution	89.5	91.2	94.3	96.8

4.6 and Table 4.3. Initially, as the inlet mass flux is increased from 0.162 kg/m^{2}s to 0.274 kg/m^{2}s, the available hydrogen for gaseous combustion also increases. However, with further increase in the inlet mass flow rate, the increased catalytic conversion of hydrogen depletes the available hydrogen in the gas phase which inhibits the gaseous conversion. As observed, the available hydrogen for homogeneous conversion is the highest for $\dot{m}'' = 0.274$ kg/m^{2}s at its peak gaseous conversion axial location, whereas the supplied hydrogen at the inlet is higher for $\dot{m}'' = 0.558$ kg/m^{2}s.

The change in the inlet mass flux also influences the temperature field in the channel which in turn can inhibit the gas phase conversion rates. The temperature at every axial location is lower when the inlet mass flux increases, as observed in Fig. 4.9 where the mid–plane temperatures are shown along the channel. Therefore, as the inlet mass flux increases, besides the drop in the available hydrogen for gaseous combustion, lower temperature levels also restrain homogeneous combustion.

Figure 4.10 shows the OH mass fraction contours in the channel at four different inlet mass fluxes. It is found that the OH mass fraction level drops sharply as the inlet mass flux is increased above 0.406 kg/m^{2}s or decreased below 0.274 kg/m^{2}s. This behaviour is consistent with the gas phase reaction levels at different inlet mass fluxes, observed earlier.

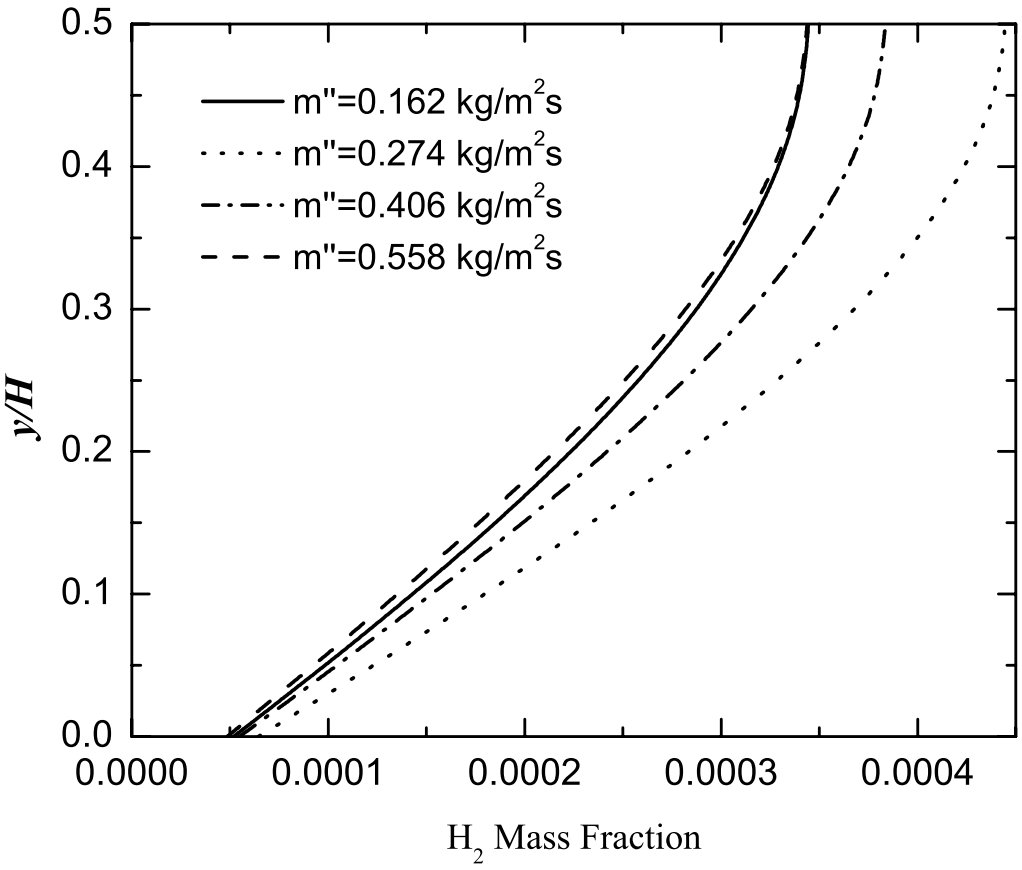

Figure 4.8: Cross–stream H_2 mass fraction at axial locations of maximum gaseous conversion (ref. Fig. 4.6 (a)). Solid line: $x/H = 0.66$; dotted line: $x/H = 0.78$; dash–dotted line: $x/H = 1.01$; dashed line: $x/H = 1.34$.

Higher gas phase contribution to H_2 conversion produces more OH in the gas phase. The location of the highest OH concentration slightly shifts downstream as the inlet mass flow rate is increased, with the gas phase reaction zone stretched along the channel.

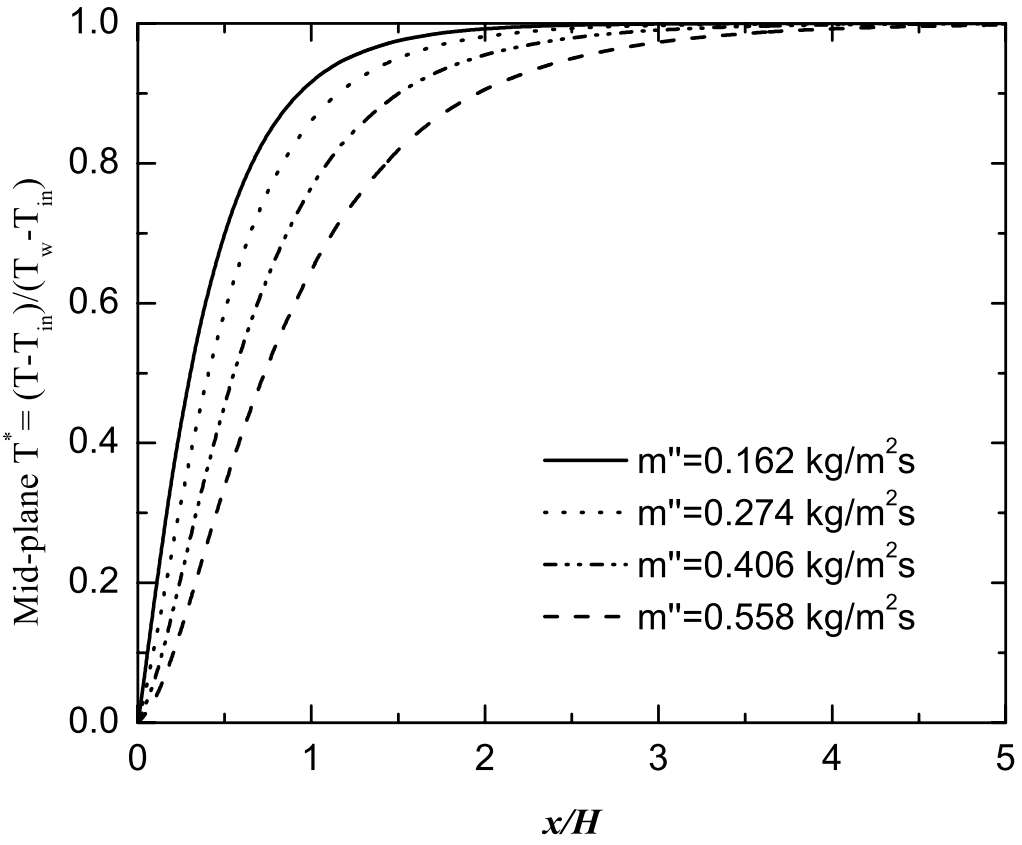

Figure 4.9: Non–dimensional mid-plane temperature T^* at different inlet mass fluxes.

4.3.3 Equivalence ratio effect

In the previous sections, the fuel–air equivalence ratio of the mixture at the inlet was kept constant at $\varphi = 0.45$. However, since the chemical kinetics of the reacting flow is a strong function of the equivalence ratio, its effect is also studied independently in this section. To this end, the inlet mixture equivalence ratio is varied keeping the wall temperature $T_w = 1450$ K constant. At low equivalence ratios, due to the absence of enough fuel, the reaction rates are generally lower. This can be confirmed in Fig. 4.11 where the gas phase

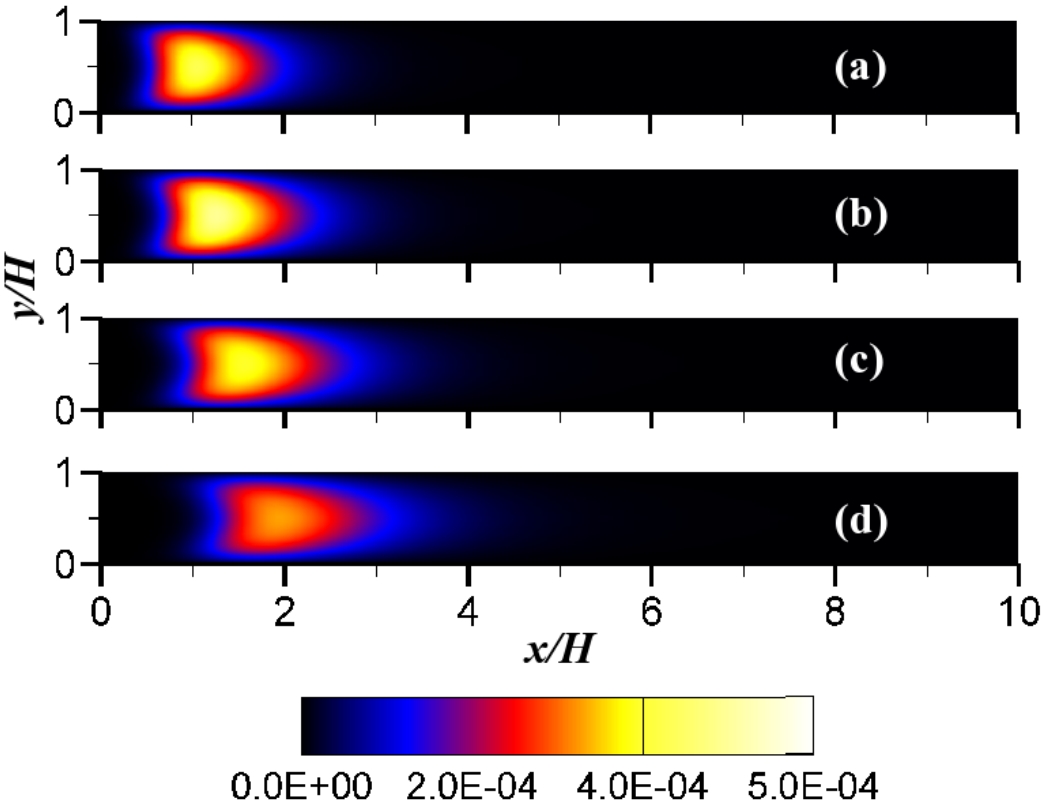

Figure 4.10: OH mass fractions at different inlet mass flow rates, (a) $\dot{m}'' = 0.162$, (b) $\dot{m}'' = 0.274$, (c) $\dot{m}'' = 0.406$, (d) $\dot{m}'' = 0.558$ kg/m^{2}s along a 700μm channel with $T_w = 1450$ K.

(integrated over channel half–height) and wall conversion rates of H_2 are depicted along a 700 μm channel. In all cases, the inlet mass flux is set equal to $\dot{m}'' = 0.355$kg/m^{2}s. As expected, the gas phase and wall conversion rates of H_2 are higher for relatively richer mixtures. The increase in the relative gas phase contribution to the overall H_2 conversion can be clearly detected at $\varphi = 0.75$ by observing the sudden drop in the wall conversion rate in Fig. 4.11. Leaner fuel/air mixtures exhibit a monotonic decrease in the wall conversion rate along the channel as the fuel gets depleted mainly through the wall reaction. however,

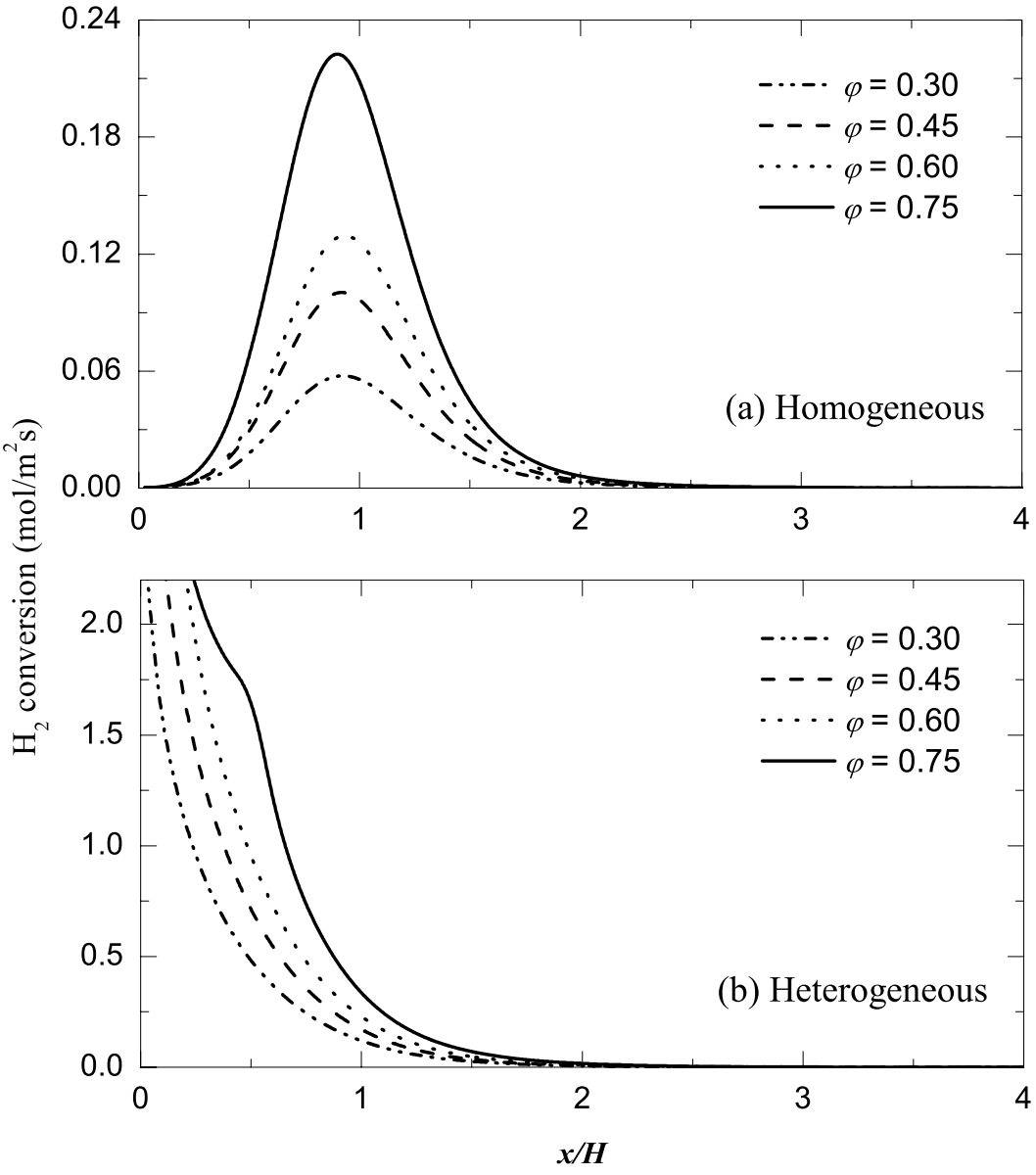

Figure 4.11: (a) Gas phase (integrated over channel half–height) and (b) catalytic H_2 conversion rates at different inlet equivalence ratios along a 700 μm channel with $T_w = 1450$ K.

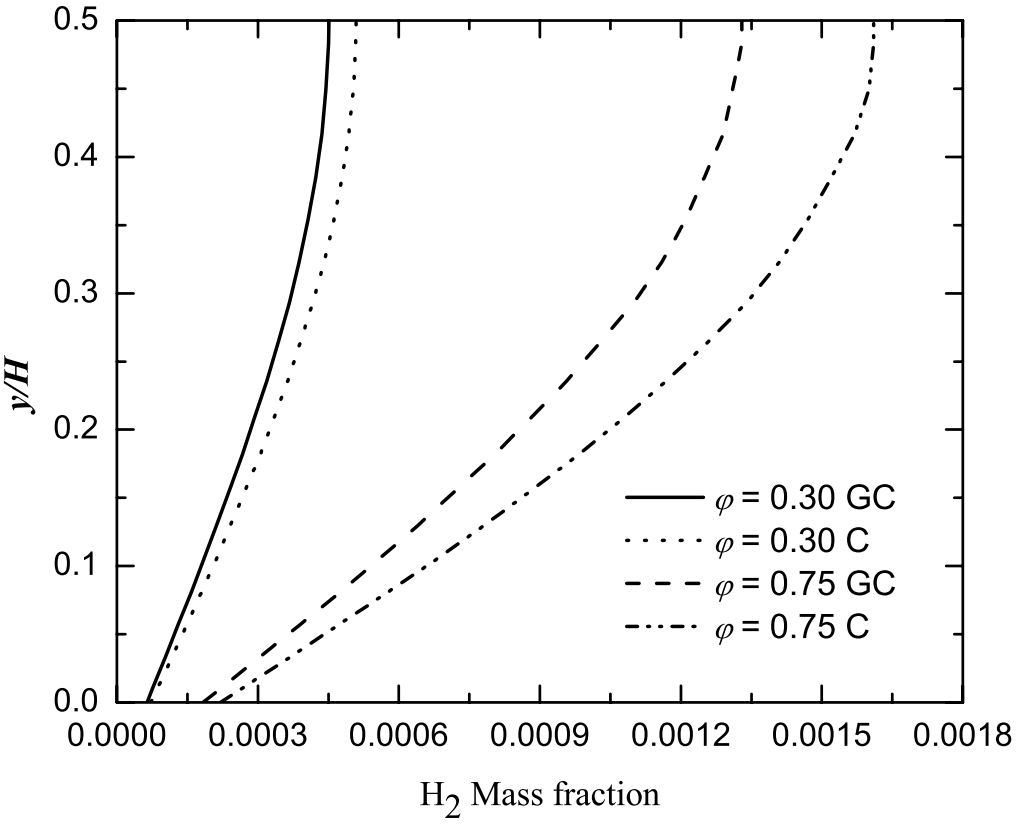

Figure 4.12: Hydrogen mass fraction across a 700 μm channel at $x/H = 0.78$; Gas phase and catalytic reactions (GC) vs. catalytic reactions only (C).

at the inlet equivalence ratio of $\varphi = 0.75$, as the gas phase reaction initiates, there is a sudden drop in the catalytic H_2 conversion rate at the wall since the gas phase hydrogen consumption becomes considerable. In order to assess the relative contribution of the gas phase reactions to hydrogen oxidation at different equivalence ratios, the results of numerical simulations with and without gas phase reactions are examined. Figure 4.12 depicts H_2 mass fraction distribution across the channel with and without considering the gas phase reactions at $x/H = 0.78$. As observed, the error associated with neglecting the

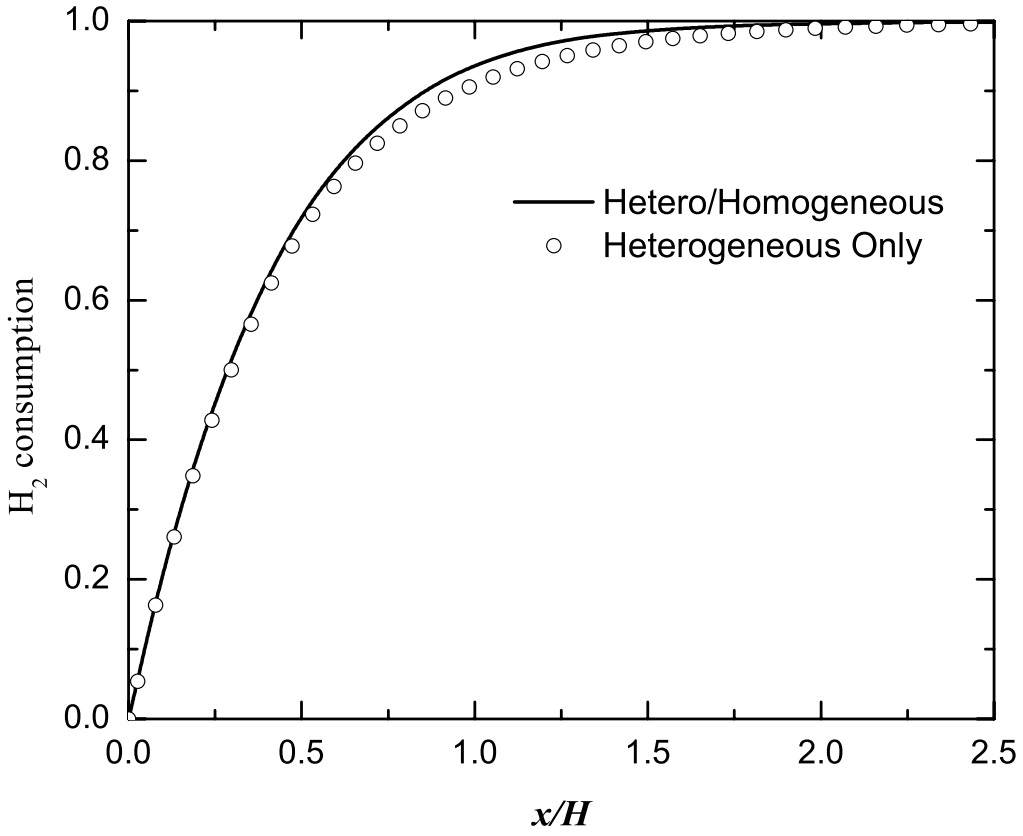

Figure 4.13: Hydrogen consumption along a 700 μm channel with an inlet equivalence ratio of $\varphi = 0.75$ and wall temperature $T_w = 1450$ K.

gas phase reactions is much higher in relatively richer mixtures. This effect can also be confirmed observing the global behaviour of the channel in H_2 conversion. Figure 4.13 shows the hydrogen consumption in a relatively richer mixture along the channel with and without considering the gas phase reactions. Hydrogen consumption at any axial location x is defined as:

$$\text{H}_2 \text{ consumption} = \left[\frac{\dot{m}_{in} - \dot{m}_x}{\dot{m}_{in}}\right]_{\text{H}_2} \tag{4.2}$$

Close to the channel inlet, since hydrogen is consumed mostly by the wall reactions, the

two simulations predict almost identical results. However, as the reaction starts in the gas phase, the difference in hydrogen consumption predictions becomes apparent. The highest difference in this case is about 3% at $x/H = 0.98$.

4.4 Conclusions

Combustion of hydrogen in Pt-coated microchannels has been studied numerically in planar geometry at a constant wall temperature. Gas phase contribution to hydrogen conversion in lean H_2/air mixtures has been investigated under different inlet mass fluxes, fuel–air equivalence ratios as well as different channel heights.

Reducing the channel height decreases the contribution of homogeneous reactions to hydrogen conversion. For a wall temperature of $T_w = 1450$ K and inlet equivalence ratio of $\varphi = 0.45$, as the channel height is reduced from 1000 μm to 600 μm, the decline in homogeneous reaction rates is gradual and is mainly due to the reduced channel volume and increased OH adsorption on the catalytic wall. The radical destruction on the wall continues to inhibit the gas phase reaction even further at smaller channel heights. The heterogeneous hydrogen conversion rate remains essentially constant in this range. The upstream diffusion of product species from the channel towards the inlet becomes considerable as the channel size is reduced because of the strong diffusive mass flux at smaller length scales. This leads to the existence of some of the product species, most notably H_2O, at the channel inlet which contributes even further to the decline in the gas phase conversion rate below the $H = 600$ μm sizes.

Variation of the inlet mass flux at constant channel height alters the balance between the convective and diffusive mass fluxes. At low inlet mass fluxes, the presence of product species suppresses the gas phase reaction rates. As the inlet mass flux of the reacting

mixture is increased, initially the amount of H_2 conversion in the gas phase also increases. However, after a certain mass flux, this trend reverses and the increased inlet mass flux leads to lower gas phase conversion. Since the catalytic H_2 conversion is diffusion-limited, it increases steadily as the inlet mass flux is increased mainly due to steeper gradients at the wall. Since the catalytic reaction is dominant in hydrogen conversion, the relative contribution of gas phase reaction to the overall conversion declines rapidly as the inlet mass flux increases.

The fuel-air equivalence ratio of the mixture significantly changes the contribution of the gas phase reactions to the overall hydrogen conversion. At low equivalence ratios, the homogeneous and heterogeneous conversion rates are both low compared to richer mixtures. As the equivalence ratio increases, both gas phase and wall reactions increase, although the rise in the gas phase conversion rate is more vigorous.

Chapter 5

Rarefaction effects on catalytic reactive flows in microchannels[1]

5.1 Introduction

In the slip flow regime, the continuum equations for mass, momentum and energy conservation can still be employed but proper slip/jump boundary conditions should be specified to account for non–equilibrium effects in the Knudsen layer. In the case of multi–species transport, an important effect analogous to temperature–jump should also be taken into account, i.e., the concentration–jump. There is very limited work on the concentration jump and its effects on catalytic reactions and the available literature has mainly focused on the temperature jump and velocity slip effects. In this chapter, the velocity slip, temperature jump and concentration jump effects on two distinct catalytic reactions are examined in planar microchannels: hydrogen oxidation on platinum; and ammonia decomposition

[1] A brief version of this section including some figures is published as an article in the Chemical Engineering Journal, 2012, Vol. 181-182, 643-654.

on ruthenium. To this end, the slip/jump boundary conditions derived in section 2.2 are employed. This set of boundary conditions, derived in their most general form, represent various terms in predicting the slip/jump conditions for reacting multicomponent mixtures. Unlike the first–order slip/jump boundary conditions where the mixture–averaged properties are utilized to relate the slip velocity and temperature discontinuity to the field variable gradients, this set of conditions accounts for individual species separately along with possible concentration discontinuity at the wall. Due to very small channel sizes considered in the present study, the homogeneous reactions can be ignored as discussed in detail in chapter 4. Detailed surface reaction mechanisms are employed in order to fully account for the effects of surface species in determining the heterogeneous reaction pathways.

5.2 Catalytic oxidation of lean H_2/air mixture on Pt

The schematic view of channel geometry and the coordinate system are shown in Fig. 3.11. The governing mass, momentum, energy, and species continuity equations are described in section 2.1. Detailed gas phase and surface reaction mechanisms along with a multi–component species diffusion model are used. These equations were discretized using the colocated finite volume method. After each step in the solution of gas phase species, the flux matching boundary condition (2.51) and the surface species production rate (2.52) equations are solved on every wall element considering the concentration–jump effect, Eq. (2.47). These equations form a set of non–linear DAEs and are solved using the SUNDIALS code [40]. The solution to this set of equations yields the surface species site fractions on the *wall* and the mass fractions of gas phase species at the edge of the *Knudsen layer* which are employed as the proper boundary conditions for the next iteration. This was described in more detail in section 2.2.2. The mixture transport properties as well as the pure species

properties are obtained using the CHEMKIN database [47]. The production rate of both gas and surface species on the wall are modeled using a detailed surface reaction mechanism proposed by Deutschmann et al. [23] as shown in Table 4.2.

Some parameters are kept constant in order to make a meaningful comparison between different cases studied in this chapter. To this end, the inlet mass flux of each species is assumed to be constant in each simulation. This constraint forces the overall inlet mass flux to remain constant as well. This approach is especially useful when dealing with low Péclet number ($\mathrm{Pe}_k = \mathrm{ReSc}_k$, where Sc is the Schmidt number) flows in which the inlet diffusion mass flux can be significant. At each iteration, the inlet mass fraction of all species Y_k and the mass–averaged inlet velocity $\mathbf{U}$ are calculated using $\vec{m}_k'' = \rho Y_k \mathbf{U} + \mathbf{J}_k = \text{const}$ (N_g constraints) along with $\sum_{k=1}^{N_g} Y_k = 1$. The diffusive fluxes of species $\mathbf{J}_k$ are calculated from the previous iteration. This is discussed in more detail in chapter 4.

The surface site density of the catalytic walls is specified to be $\Gamma = 2.7 \times 10^{-5} \mathrm{mole/m}^2$ simulating a polycrystalline platinum coating [23]. In this study, the inlet gas temperature is assumed to be $T_{in} = 300$ K while the wall temperature T_w is maintained at 1000 K, unless otherwise specified. The equivalence ratio of the mixture is also specified at the inlet for each case. The flow is mass driven such that the mass flux of each species is constant at the channel inlet. The outlet pressure is assumed to be atmospheric. The accommodation coefficient θ is equal to zero for specular reflection at the wall and equal to 1 for diffuse reflection [15]. This coefficient decreases for high temperatures and rough surfaces and typically can range between 0.1 to 1.0. In this chapter, two values of 0.25 and 1.0 are chosen for the surface accommodation coefficient. For the low Péclet number flows considered here, the numerical simulations show that a channel length of about $4H$ is sufficient for all the variables to develop. In this chapter, a channel length of $L = 6H$ is considered for all simulations.

Table 5.1: Operating conditions and geometrical specification of different simulation cases of hydrogen oxidation. In all cases, the surface accommodation coefficient of other species θ_k is equal to 1.

	H (μm)	$\dot{m}''_{\text{in}}$(kg/m^{2}s)	T_w (K)	θ_{H_2}
Case 1	25	4.0	1000	1.0
Case 2	25	4.0	700	1.0
Case 3	25	4.0	700	0.25
Case 4	25	3.0	1000	1.0
Case 5	25	1.0	1000	1.0
Case 6	50	4.0	1000	1.0
Case 7	10	4.0	1000	1.0

5.2.1 Results and discussion

In this section, the effects of slip/jump boundary conditions on various field variables are discussed. The previously described velocity slip, temperature jump and concentration jump boundary conditions are denoted by "VS", "TJ" and "CJ", respectively. The inlet equivalence ratio of the mixture is set constant to $\phi = 0.5$ in all simulations. The inlet mass flux of species as well as the wall temperature T_w and channel height are specified for different cases as outlined in Table 5.1.

Flow and temperature fields

A channel with operating conditions of Case 1 is simulated under different boundary condition combinations and the resulting slip velocity and temperature jump along the channel are shown in Fig. 5.1 (a) and (b). When only the velocity slip boundary condition is considered, the temperature at the edge of the Knudsen layer is equal to the wall temperature, which eliminates the axial temperature gradient. In such a case, the wall shear stress

τ^{xy} governs the slip velocity behavior. Due to the very low Reynolds number (Re $\sim$ 1), normal velocity gradients are only significant close to the channel inlet and quickly fade out further down the channel. Therefore, except for regions close to the inlet, the velocity slip does not influence the flow field to a great extent. On the other hand, the temperature discontinuity at the wall significantly affects the slip velocity. The presence of a strong temperature gradient along the wall in the developing region of the channel increases the slip velocity. The temperature jump itself is mostly influenced by the temperature gradient normal to the wall. Again, the highly diffusive nature of the transport processes in these small channels (Pe $\sim$ 1) diminishes the gradients within about one channel height into the channel.

The concentration jump boundary condition, however, does not alter the velocity slip and temperature jump at the wall and its influence is negligible. Although, as will be discussed later, the species mass fractions are affected by the concentration jump boundary condition, their effect on the mixture properties is minimal and hence does not influence the flow and temperature fields. The above mentioned effects are more evident in Fig. 5.1 (c) and (d) where the velocity and temperature fields are sketched across the channel at $x/H = 0.103$ under different boundary condition combinations. Clearly, in this operating condition, the presence of temperature jump is the most important factor in defining both the velocity and temperature fields. The minimal effect of concentration jump boundary condition on the velocity and temperature distributions across the channel is also evident.

The Knudsen number plays an important role in characterizing the heat and mass transfer properties of slip flows. Based on the kinetic theory of gases, the mean free path of each species ζ_k is related to its viscosity as:

$$\zeta_k = \frac{16}{5} \frac{\mu_k}{\rho\sqrt{2\pi R_k T}} \tag{5.1}$$

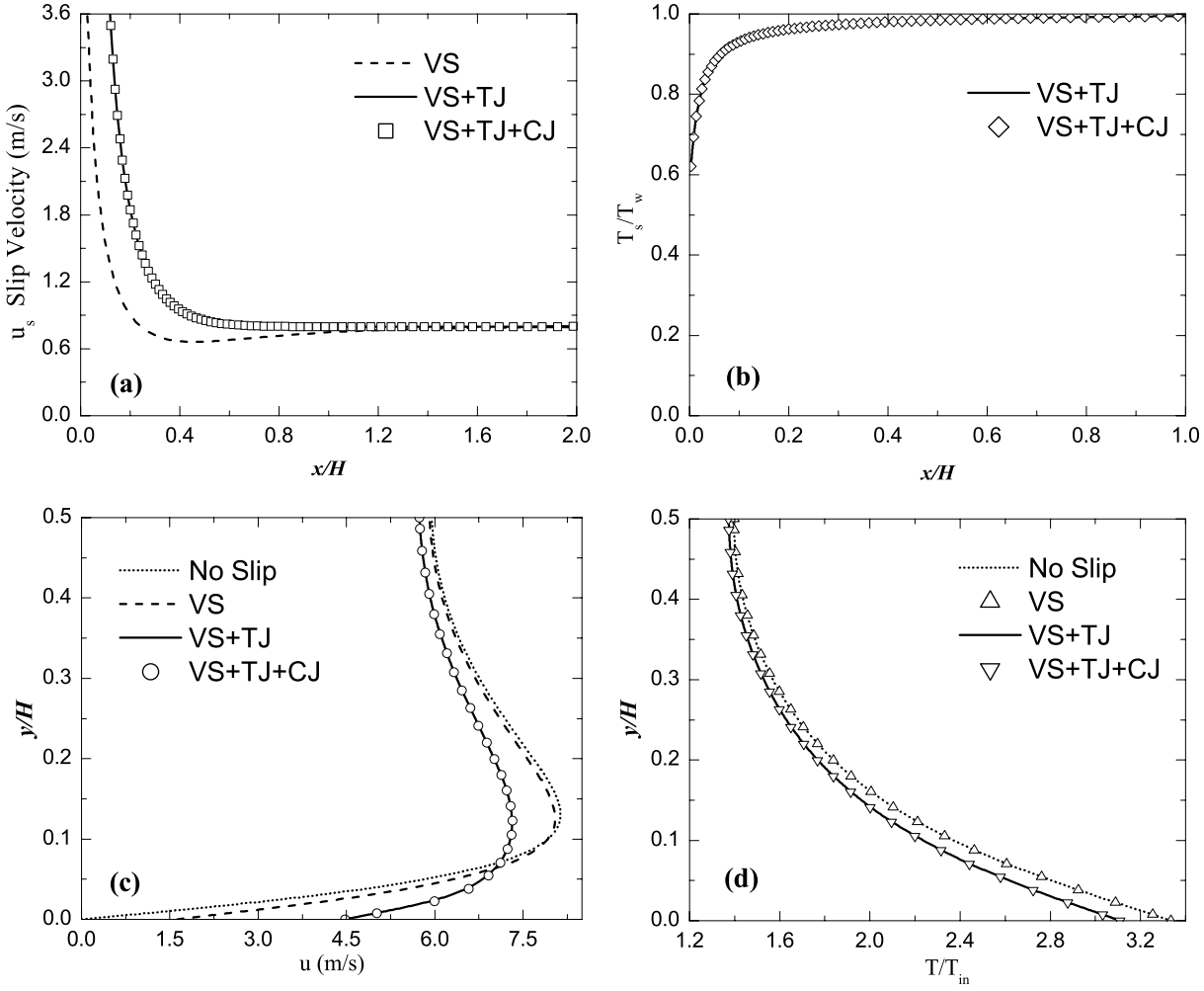

Figure 5.1: Velocity slip (a) and temperature jump (b) at the edge of the Knudsen layer along the channel under different slip/jump boundary conditions. Cross stream velocity (c) and temperature (d) distributions at $x/H = 0.103$ for Case 1.

For comparison purposes, in this chapter, the mixture Knudsen number is defined based on a mass–averaged mean free path. As can be readily seen in this equation, the Knudsen number is a function of field variables, and therefore, changes in different cases studied in the present work. However, under the operating conditions of Case 1, the Knudsen number

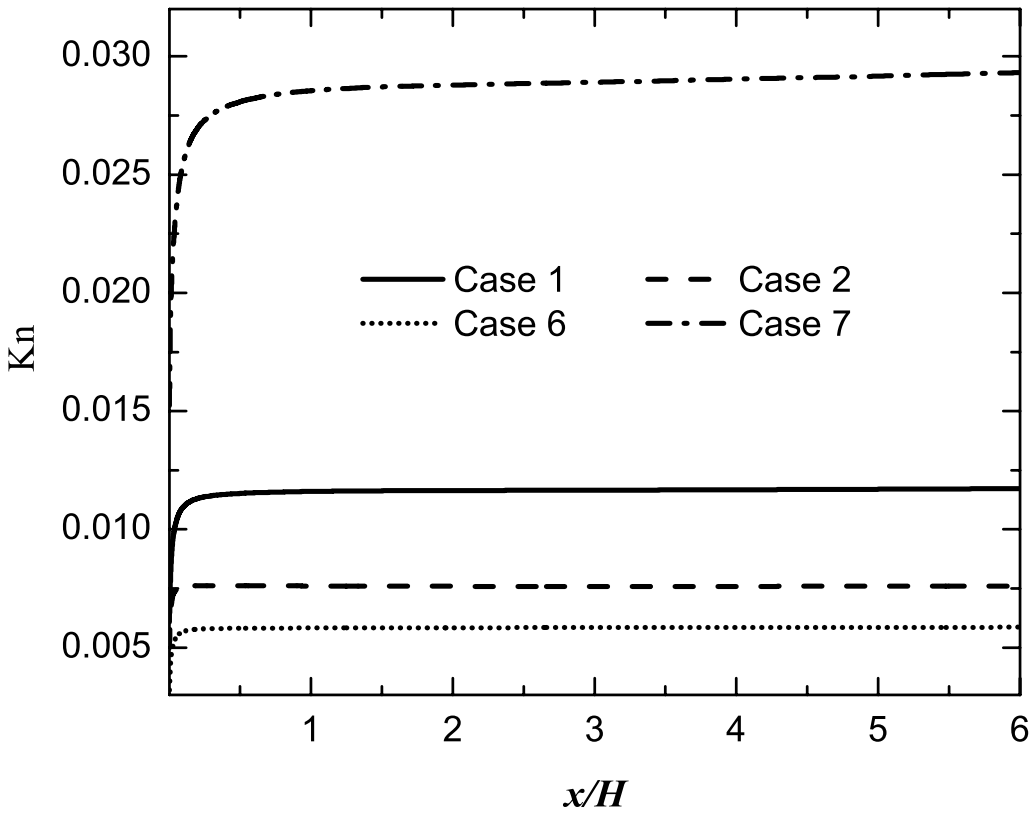

Figure 5.2: The Knudsen number variation along the channel under different operating conditions.

remains close to 0.012. The typical Knudsen number behavior is shown Fig. 5.2 for various cases where all slip and jump boundary conditions are in effect.

Mass transfer

Due to the constant mass flux boundary condition imposed at the inlet, the species mass fractions can be different under different wall boundary condition combinations. The inlet mass flux of each species $\dot{m}''_k = \rho Y_k \mathbf{U} + \mathbf{J}_k$ consists of the diffusion mass flux and the

convective mass flux of that species. With different wall boundary conditions the flow field can change significantly. Therefore, the inlet mass fraction of each species will adjust itself to keep the mass flux constant. Right at the channel inlet, due to hydrogen consumption in the channel, there exists a positive diffusive mass flux of hydrogen into the channel. In order to keep the total hydrogen inlet mass flux constant, the inlet mass fraction of the hydrogen should be adjusted (lowered) accordingly. On the other hand, the H_2O produced in the channel can diffuse back towards the channel inlet which results in a negative diffusive mass flux of H_2O out of the channel. Since the total H_2O mass flux (diffusion + convection) is set equal to zero in the simulations, this outgoing diffusive H_2O mass flux should be balanced by the incoming convective flux, i.e. $\rho Y_{H_2O}\mathbf{U}$, at the inlet. Therefore a finite amount of H_2O will exist at the channel inlet despite the zero total inlet H_2O mass flux.

The inlet mass fraction of H_2 is shown in Fig 5.3 (a) under different types of wall boundary condition combinations for Case 1. Interestingly, the hydrogen mass fraction profile changes its direction close to the wall. In the entrance region, the thermal diffusion effect becomes very strong close to the wall and overwhelms the concentration gradient in Eq. (2.7). Therefore, despite the net hydrogen diffusive mass flux being towards the wall, the hydrogen concentration gradient is reversed in this region. Neglecting the thermal diffusion effect in the diffusive mass flux calculations, therefore, can lead to a different inlet (and consequently within the channel) hydrogen distribution. This can be seen in Fig. 5.3 (b) where the inlet hydrogen mass fraction is depicted for Case 1 without the thermal diffusion term in Eq. (2.7). In both figures, it is evident that the velocity slip boundary condition alone does not affect the inlet composition. However, the presence of a temperature discontinuity noticeably alters the inlet hydrogen mass fraction especially in regions close to the wall.

The species mass fractions of H_2, O_2 and H_2O at the edge of the Knudsen layer are

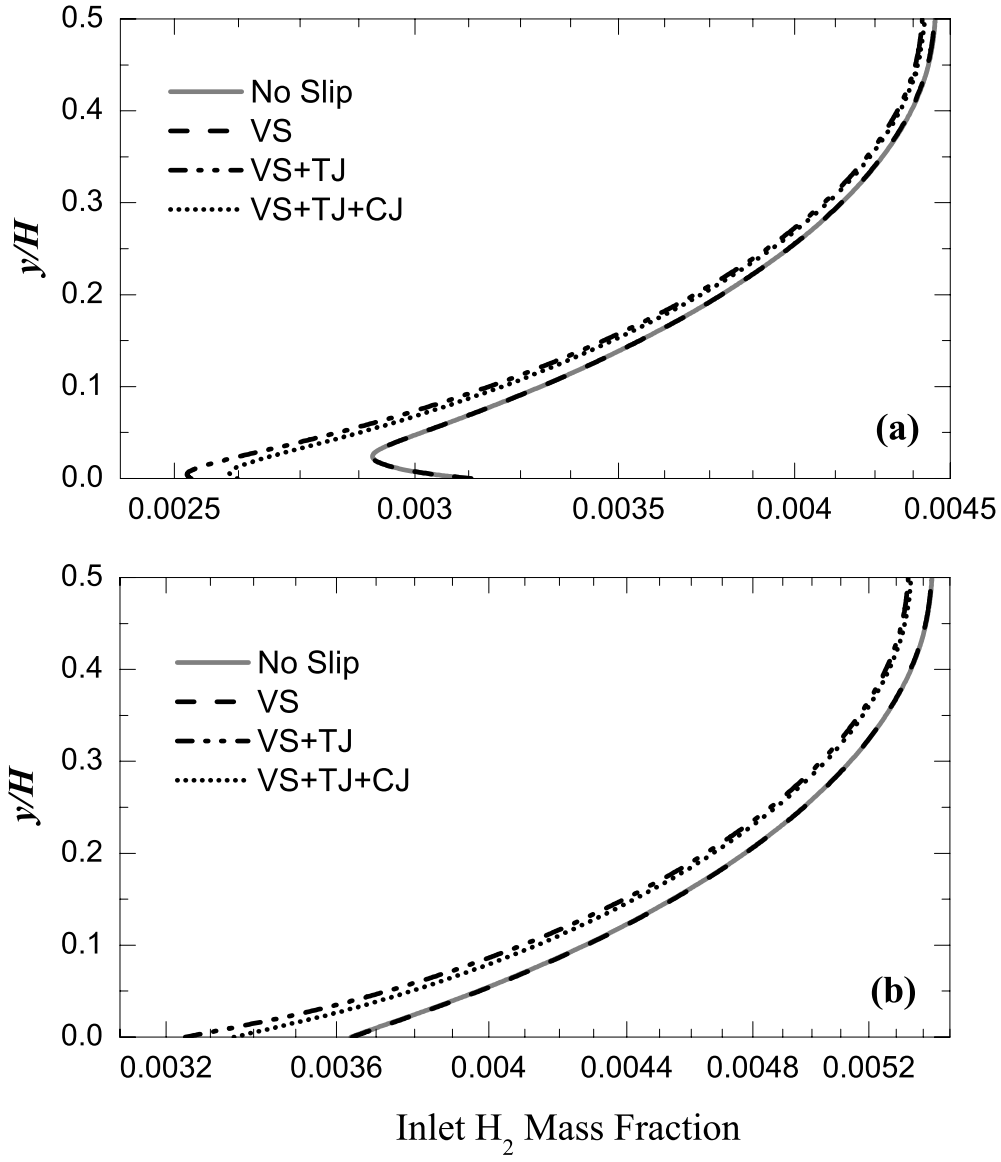

Figure 5.3: Inlet H_2 mass fractions for different types of wall boundary conditions in Case 1; diffusion mass flux calculated (a) with thermal diffusion, (b) without thermal diffusion in Eq. (2.7).

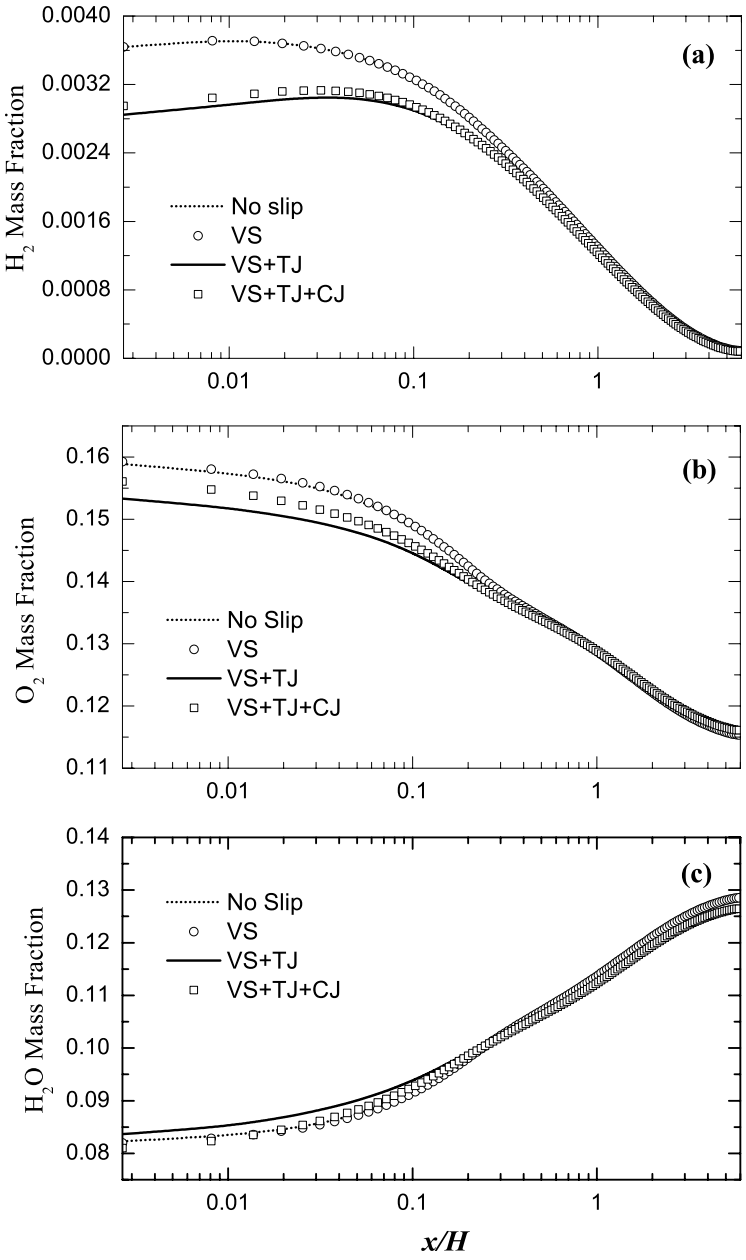

Figure 5.4: H_2 (a), O_2 (b) and H_2O (c) mass fractions at the edge of the Knudsen layer of Case 1 under different types of wall boundary conditions along the channel.

shown in Fig. 5.4 for Case 1 along the channel. The velocity slip, as observed earlier, only slightly changes the species inlet composition and temperature and velocity fields. Hence, its influence on the species mass fractions is also negligible. The noticeable decrease in the hydrogen and oxygen mass fractions in the "VS+TJ" cases is mainly due to the *constant mass flux* treatment of the inlet boundary. With velocity slip and temperature jump at the wall, the velocity profile begins to resemble plug flow (Fig. 5.1 (c)). The increased slip velocity close to the wall decreases the inlet hydrogen and oxygen mass fractions in this region as observed in Fig 5.3. The slight increase in H_2O mass fraction at the edge of the Knudsen layer in "VS+TJ" boundary condition is due to the increased water levels at the inlet under this particular boundary condition. With the introduction of concentration jump, the hydrogen and oxygen mass fractions slightly increase at the wall. This is again related to the altered inlet composition when there is a concentration discontinuity at the wall.

The species distribution in the channel is influenced by the boundary conditions considered on the wall as well. The hydrogen mass fraction across the channel is shown in Fig 5.5 at two axial locations of $x/H = 0.044$ and $x/H = 0.103$ for Case 1. In regions close to the wall, the hydrogen mass fraction in the "No Slip" case is over–predicted by about 13% and 10% compared to the "VS+TJ" and "VS+TJ+CJ" cases, respectively, with the difference diminishing towards the channel center. This over–prediction is partly due to lower inlet hydrogen mass fractions in the "VS+TJ" and "VS+TJ+CJ" cases (see Fig 5.3 (a)) which is carried over into the channel. The difference in catalytic hydrogen consumption at the wall under different wall boundary conditions can also lead to this over–prediction.

In order to investigate slip/jump effects on species transport, the catalytic conversion rates of H_2 for Case 1 under various boundary condition combinations are shown in Fig. 5.6. Due to a very low Reynolds number, the transport of species and energy is generally

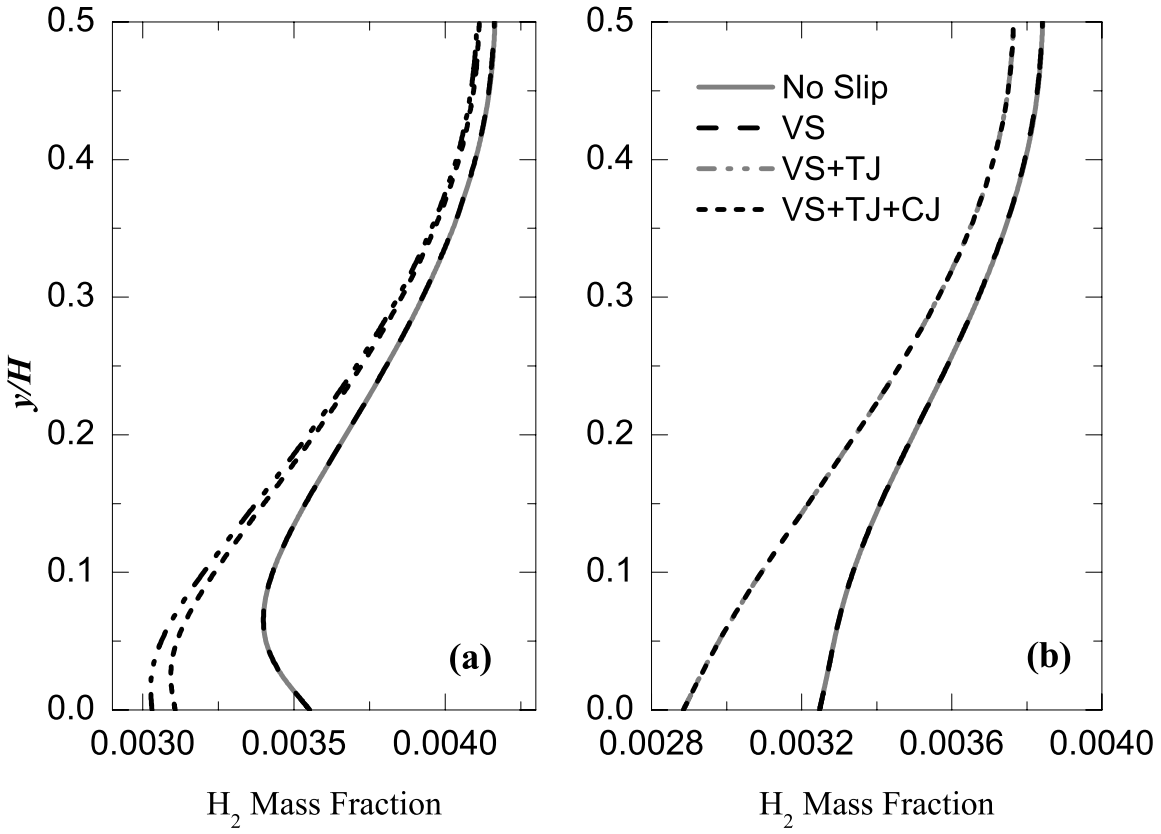

Figure 5.5: Hydrogen mass fraction across the channel at (a) $x/H = 0.044$ and (b) $x/H = 0.103$ for Case 1 under different boundary condition combinations.

diffusive and therefore the velocity slip does not alter the flow and temperature fields significantly, as observed in Fig. 5.1 (c). As such, the velocity slip boundary condition alone has a very small impact on the hydrogen conversion rate. However, the influence of the temperature jump boundary condition is noticeable, especially in the developing region. The axial temperature gradient at the edge of the Knudsen layer substantially increases the slip velocity, which in turn enhances the convective mass transfer and causes steeper gradients in the vicinity of the wall. As the temperature jump boundary condition

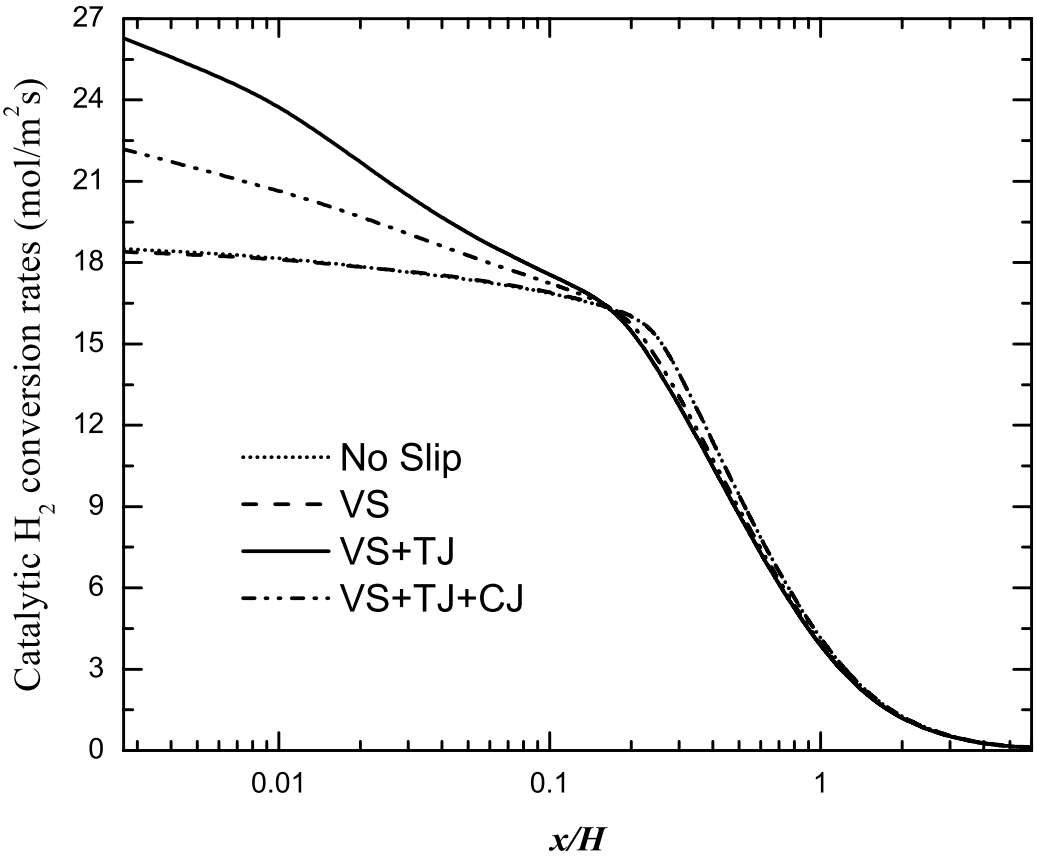

Figure 5.6: Catalytic conversion rates of H_2 along the channel for Case 1 under different types of boundary condition combinations.

is introduced, the conversion rate experiences a considerable increase in the developing region and then merges with the no–slip case result further downstream. The presence of concentration discontinuity at the wall, on the other hand, counter balances the increase in hydrogen conversion rate by reducing the species mass fraction gradient normal to the wall. The decrease in the concentration gradients (and consequently the hydrogen diffusive mass flux towards the wall) translates into lower hydrogen conversion rates as can be readily seen in Eq. (2.51).

Species coverage on the catalytic wall is also influenced by the slip/jump boundary conditions. The surface coverage of H(s) and O(s) are mainly dictated by the gas phase concentration of H_2 and O_2 just above the catalytic wall (in this case, the edge of the Knudsen layer). It has also been shown that for the fuel lean mixtures, Pt(s) and O(s) are the dominant surface species [37, 38]. Figure 5.7 shows the surface coverage Z_k of different species at the wall. Low H(s) coverage indicates that the heterogeneous reaction initiation step (reaction S5 in Table 4.2) is limited by the reactant coverage which is restrained by the mass diffusion to the wall. The H(s) coverage follows the same trend as H_2 mass fraction at the edge of the Knudsen layer observed in Fig. 5.4 (a). The increase in near–wall velocity due to velocity slip and temperature jump enhances species transfer which lowers the H(s) coverage even further. The presence of concentration discontinuity at the wall slightly decreases the H(s) coverage. This is due to the increased H_2 level at the edge of the Knudsen layer in the presence of the concentration jump boundary condition. With the introduction of velocity slip and temperature jump, the increase in O(s), as described earlier, is again due to the abundance of oxidizer in a fuel–lean mixture and increased mass transfer to the wall. The H_2O(s) is influenced the most by the presence of concentration discontinuity at the wall. The H_2O(s) coverage is not affected as the velocity slip and temperature jump boundary conditions are exercised.

Different factors contribute to the concentration jump of each species as inferred from Eq. (2.47): the normal stress τ_k^{yy}, the surface production rate J_{ky}, the temperature discontinuity $(T_w/T_s)^{(1/2)}$, and finally physical and chemical properties of the surface θ_k, γ_k. As stated earlier, due to very low Reynolds number, the normal stress τ_k^{yy} is negligible compared to local pressure and its effect will not be investigated separately here. In order to examine the direct effect of the temperature jump term $(T_w/T_s)^{(1/2)}$ on concentration jump, Case 1 is simulated with this term artificially set equal to 1. The catalytic hydrogen

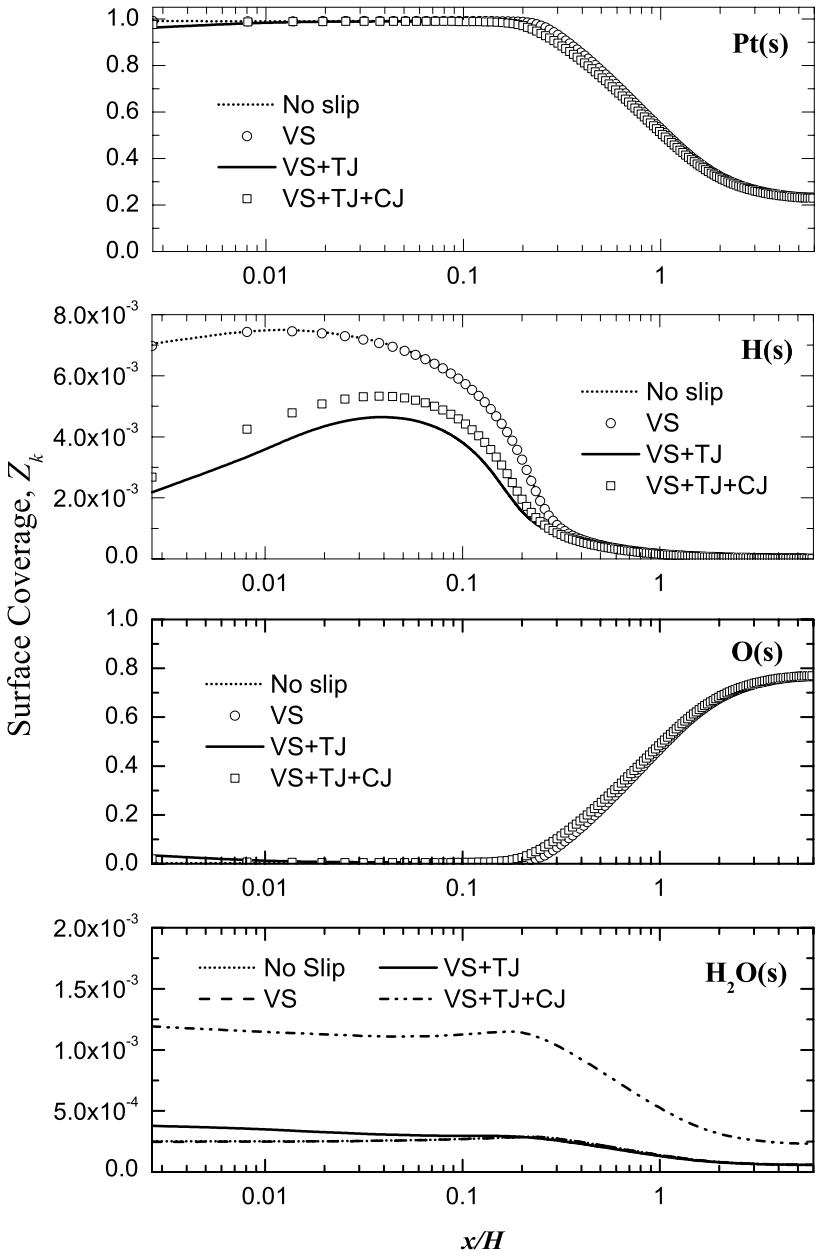

Figure 5.7: Surface species coverage of Pt(s), H(s), O(s) and H_2O(s) of Case 1 at the wall under different types of wall boundary conditions along the channel.

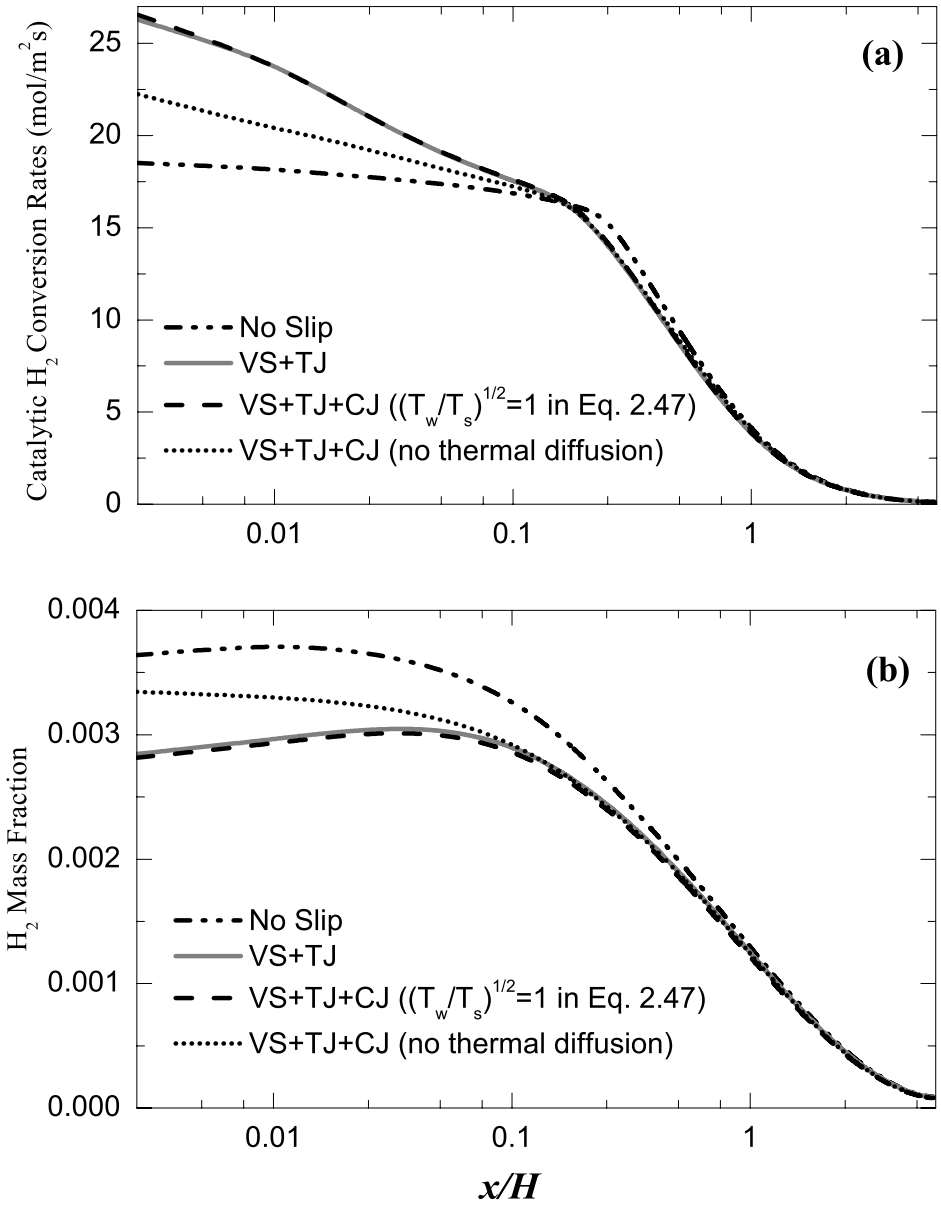

Figure 5.8: (a) Catalytic hydrogen conversion rates and (b) mass fraction of H_2 at the edge of the Knudsen layer along the channel for Case 1 under different types of boundary condition combinations.

production rate and its mass fraction at the edge of the Knudsen layer are shown in Fig. 5.8. As observed, the temperature discontinuity term is clearly the dominant factor in defining the concentration jump effect. With this artificial adjustment of the $(T_w/T_s)^{(1/2)}$ term, concentration jump boundary condition has very little impact on the catalytic hydrogen conversion as well as the wall H_2 mass fraction. It is also interesting to note that the absence of the thermal diffusion term in calculating the diffusive mass flux of species leads to an under prediction of the hydrogen conversion rate and a higher H_2 mass fraction at the edge of the Knudsen layer.

The surface accommodation coefficient directly influences the concentration jump boundary condition. An accommodation coefficient of 1.0 physically implies that all the impinging molecules come to thermodynamic equilibrium with the wall and are then released back into the flow field diffusively with a normal velocity distribution [107]. Decreasing the accommodation coefficient, therefore, shifts this trend towards specular reflection where some of the incident gas molecules are specularly reflected by the wall without reaching the equilibrium state. The surface accommodation coefficient, appearing on the right hand side of the concentration jump boundary condition (Eq. (2.47)), directly influences the terms involving the normal stress τ_k^{yy} and the surface production rate J_{ky}. Lower accommodation coefficients magnify the effect of normal diffusive fluxes of species. In order to study the relative importance of the accommodation coefficient, Cases 2 and 3 with hydrogen accommodation coefficients of 1.0 and 0.25, respectively, are considered here. It should be recalled that in the present work, the momentum and thermal accommodation coefficients are the same. The catalytic hydrogen conversion rates and the H_2 mass fractions at the edge of the Knudsen layer are shown in Fig. 5.9. As observed, the reduction in the accommodation coefficient does not change the catalytic conversion rate noticeably and most of the change between the "No Slip" and "VS+TJ+CJ" cases are again due to

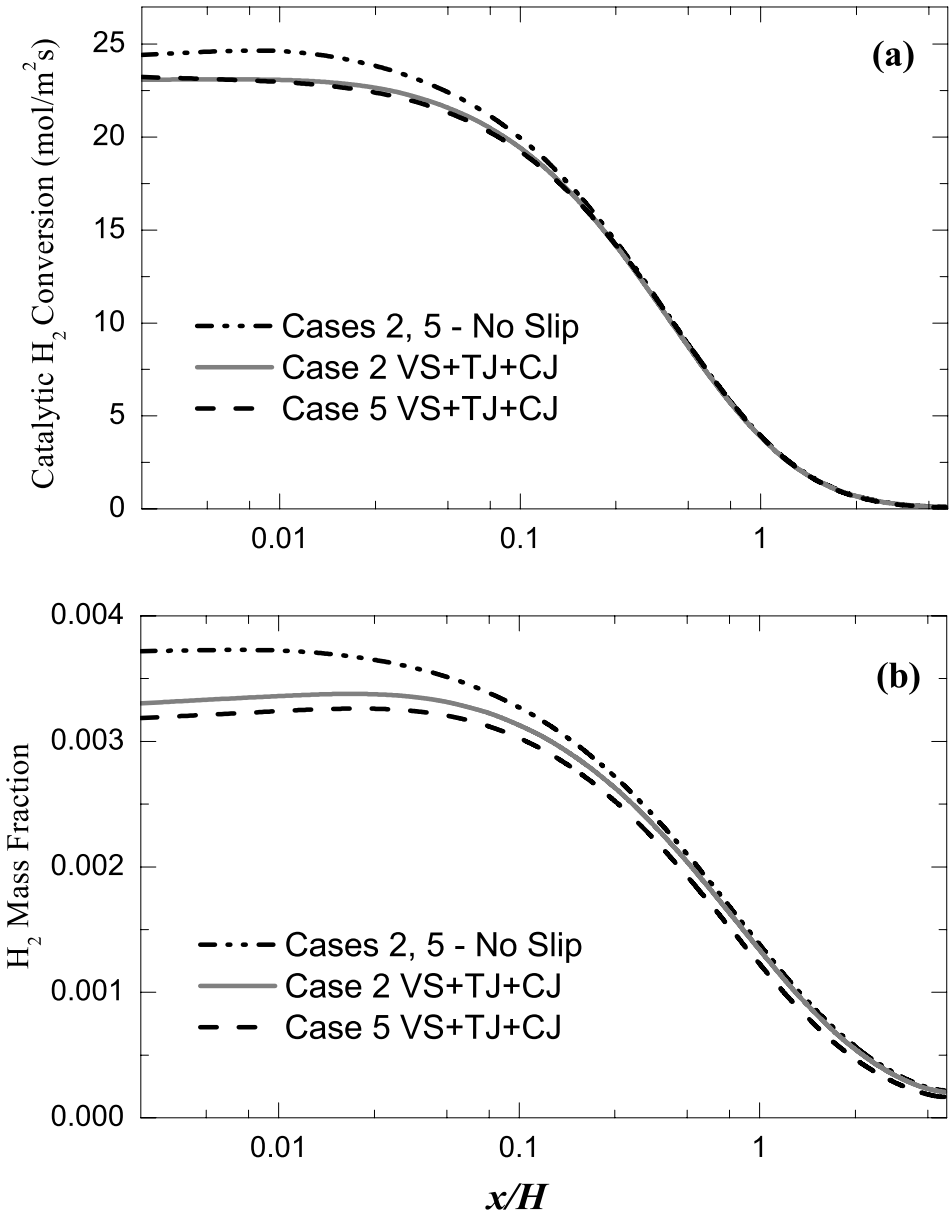

Figure 5.9: (a) Catalytic conversion rates and (b) wall mass fraction of H_2 along the channel for Cases 2 and 3.

the temperature discontinuity $(T_w/T_s)^{(1/2)}$ at the edge of the Knudsen layer. The wall H_2 mass fraction is only slightly reduced as the accommodation coefficient is reduced.

The inlet mass flux can also change the mass transfer characteristics of such flows by altering the flow and temperature distributions as well as their gradients within the field. In order to study these effects, three different inlet mass fluxes of 4.0, 3.0 and 1.0 kg/m^2s (Cases 1, 4 and 5) are examined. The catalytic conversion rate of hydrogen and the surface species coverages of H(s), O(s) and H_2O(s) are shown in Fig. 5.10. The surface catalytic conversion rate noticeably decreases as the inlet mass flux decreases. There are two main reasons behind this behavior: lower mass transfer to the wall (due to decreased gradients) and different inlet H_2 and H_2O compositions. As the inlet mass flux decreases, the process of mass transfer is mostly carried out by diffusion and the fuel (hydrogen) mass fraction at the edge of the Knudsen layer drops as observed in Fig. 5.11 (a). This brings the combustion process closer to the mass transport limited operation state (in an ideal mass transport limited case, the hydrogen mass fraction at the wall is zero) where the consumption of hydrogen is limited by the available amount of fuel at the surface.

The inlet H_2 and H_2O compositions also affect the catalytic hydrogen conversion rate as the mass flux is reduced. As observed in Fig. 5.11 (b), the inlet H_2 mass fraction is considerably reduced in Case 5 and this effect will be carried over into the domain. Besides the altered balance between the convective and diffusive terms discussed above, the reduced hydrogen mass fraction at the inlet is another factor in reducing the hydrogen mass fraction at the edge of the Knudsen layer. Figure 5.11 (c) shows the inlet H_2O mass fraction in Cases 1, 4 and 5. The increased H_2O content at the inlet is due to the increased effect of diffusive mass transfer as discussed in detail in chapter 4.

The difference between the "No Slip" and "VS+TJ+CJ" predictions of O(s) surface coverage displays an interesting trend in Fig. 5.10. As observed, at an inlet mass flux of

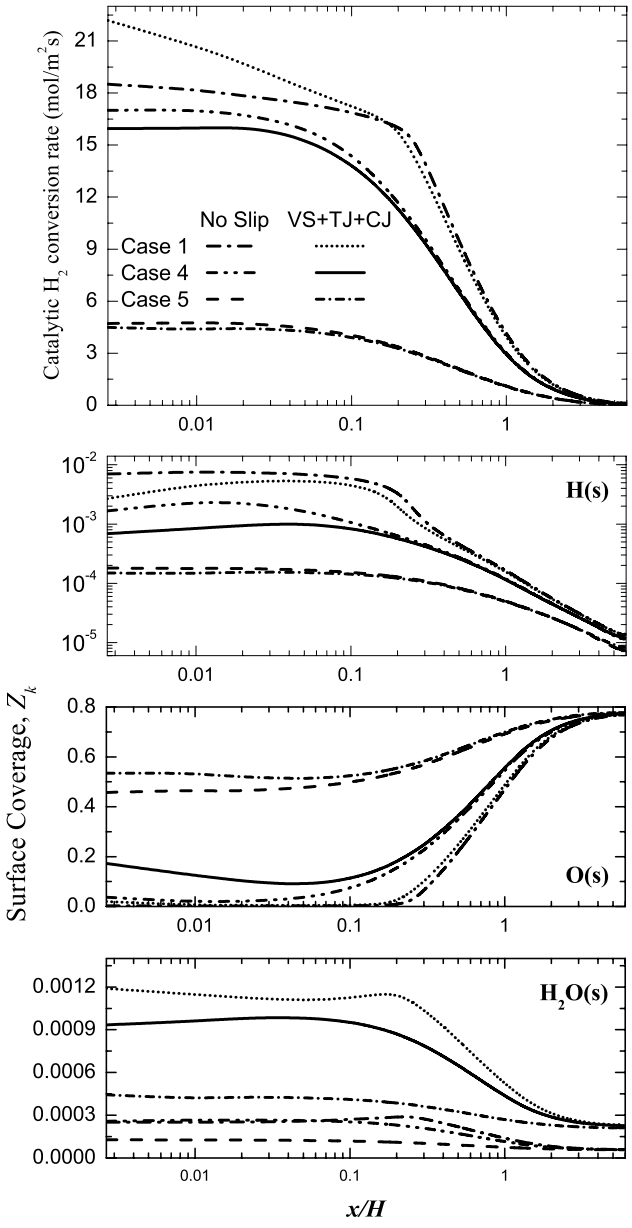

Figure 5.10: Catalytic hydrogen conversion rates and surface species coverage of H(s), O(s) and H_2O(s) of Cases 1, 4 and 5 along the channel with different inlet mass fluxes of 4.0, 3.0 and 1.0 kg/m^{2}s, respectively. The legend applies to all subfigures.

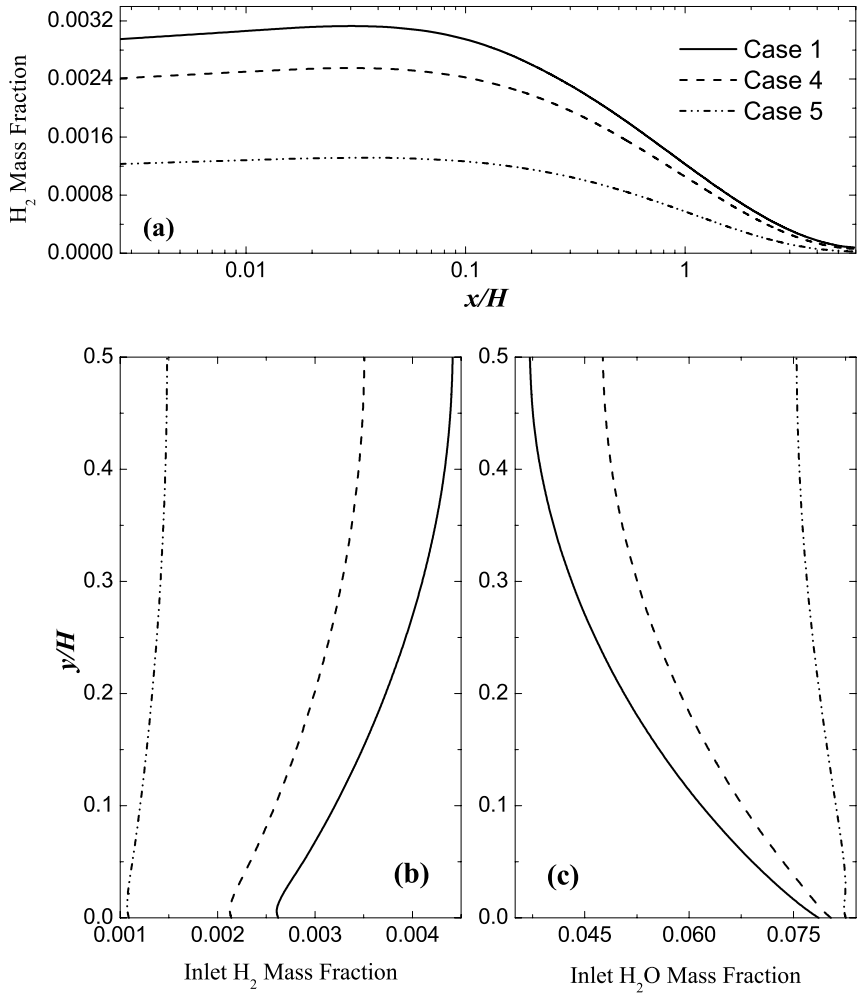

Figure 5.11: Hydrogen mass fraction at the edge of the Knudsen layer (a) and inlet (b) H_2 and (c) H_2O mass fractions of Cases 1 and 4 under "VS+TJ+CJ" boundary condition.

4.0 kg/m^{2}s, the difference between the predictions of different boundary condition sets are minimal and the O(s) surface coverage is close to zero at the channel inlet and increases further downstream. At the lowest studied inlet mass flux (1.0 kg/m^{2}s), both boundary sets predict the O(s) surface coverage close to 0.5 at the channel inlet and a gradual increase to about 0.8. However, the case with an inlet mass flux of 3.0 kg/m^{2}s is the most sensitive

to the "VS+TJ+CJ" boundary condition. The O(s) surface coverage remains close to zero at the channel inlet in the "No Slip" case while it has a finite value in the "VS+TJ+CJ" case. This behavior can be explained by observing the thermodynamics of reactions S7–S8, S9–S10, S11–S12 and S5–S15 from Table 4.2. The equilibrium condition requires:

$$K_c^{S7} = \frac{Z_{\mathrm{OH}} Z_{\mathrm{Pt}}}{Z_{\mathrm{O}} Z_{\mathrm{H}}} \tag{5.2a}$$

$$K_c^{S9} = \frac{Z_{\mathrm{H_2O}} Z_{\mathrm{Pt}}}{Z_{\mathrm{OH}} Z_{\mathrm{H}}} \tag{5.2b}$$

$$K_c^{S11} = \frac{Z_{\mathrm{H_2O}} Z_{\mathrm{O}}}{(Z_{\mathrm{OH}})^2} \tag{5.2c}$$

$$K_c^{S15} = \frac{C_{\mathrm{H_2O}} Z_{\mathrm{Pt}}}{Z_{\mathrm{H_2O}}} \tag{5.2d}$$

where K_c is the equilibrium constant and $C_{\mathrm{H_2O}}$ is the wall concentration of H_2O [3]. These equilibrium conditions and $Z_{\mathrm{Pt}} \approx 1 - Z_{\mathrm{O}}$ [37] can be employed to calculate Z_{O} as:

$$\frac{(1 - Z_{\mathrm{O}})^3}{Z_{\mathrm{O}}} = K_c^{S5} K_c^{S7} K_c^{S13} \frac{Z_{\mathrm{H}}^2}{C_{\mathrm{H_2O}}} \tag{5.3}$$

Numerical results show that $C_{\mathrm{H_2O}}$ remains almost constant as the inlet mass flux varies. Figure 5.12 qualitatively shows O(s) surface coverage as a function of H(s). As observed, beyond a certain H(s) value (in this case 10^{-3}), the O(s) surface coverage is essentially zero. Therefore, a slight difference between the H(s) surface coverage predictions of the "No Slip" and "VS+TJ+CJ" boundary conditions can lead to a considerable change in O(s) surface coverage.

The effect of channel height on the catalytic hydrogen consumption and the wall mass fractions of species is shown in Fig. 5.13 for channel heights of 10, 25 and 50 μm. For

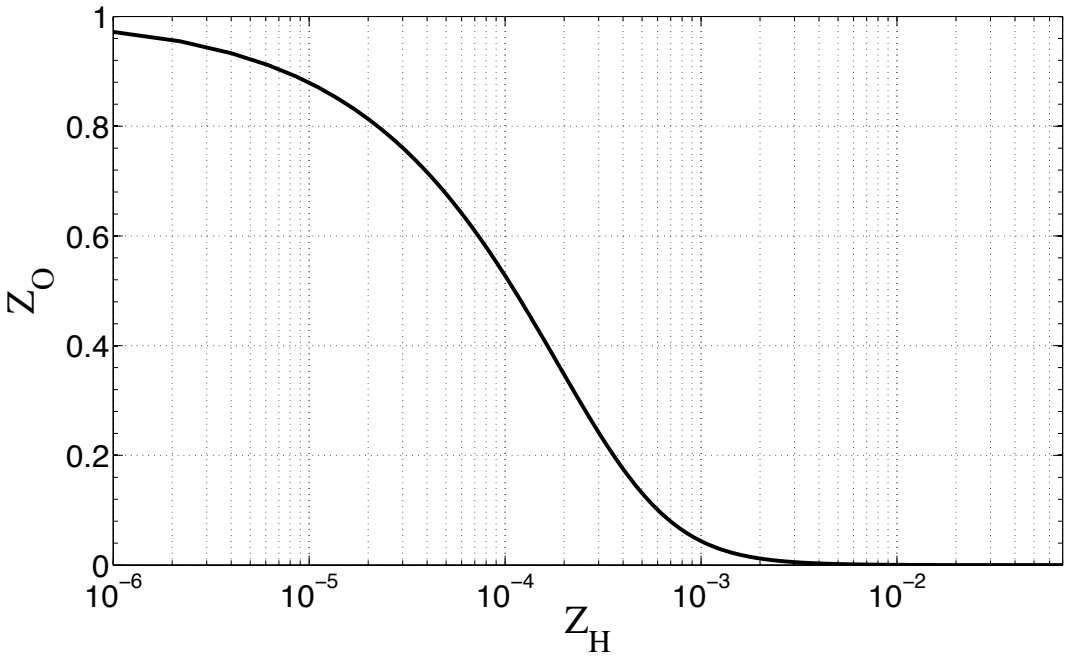

Figure 5.12: O(s) surface coverage as a function of Z_{H}.

Cases 1 and 6, the catalytic hydrogen consumption rates are higher in the "VS+TJ+CJ" case compared to the "No Slip" simulation results. As previously observed in Fig. 5.6, this is due to the temperature discontinuity at the wall and the presence of concentration jump actually suppresses this effect and reduces the catalytic conversion rate. As the channel height decreases to 10 μm (Case 7), however, the concentration jump effect becomes so important that the catalytic hydrogen conversion rate drops below the "No Slip" case as the concentration jump boundary condition is introduced. The noticeable decrease in the oxygen wall mass fraction of Case 6 observed in Fig. 5.13 is due to the relatively low diffusion coefficient of oxygen molecules compared to hydrogen. As pointed out by Bui et al. [13], even when the inlet mixture is fuel lean, the depletion of O_2 near the surface

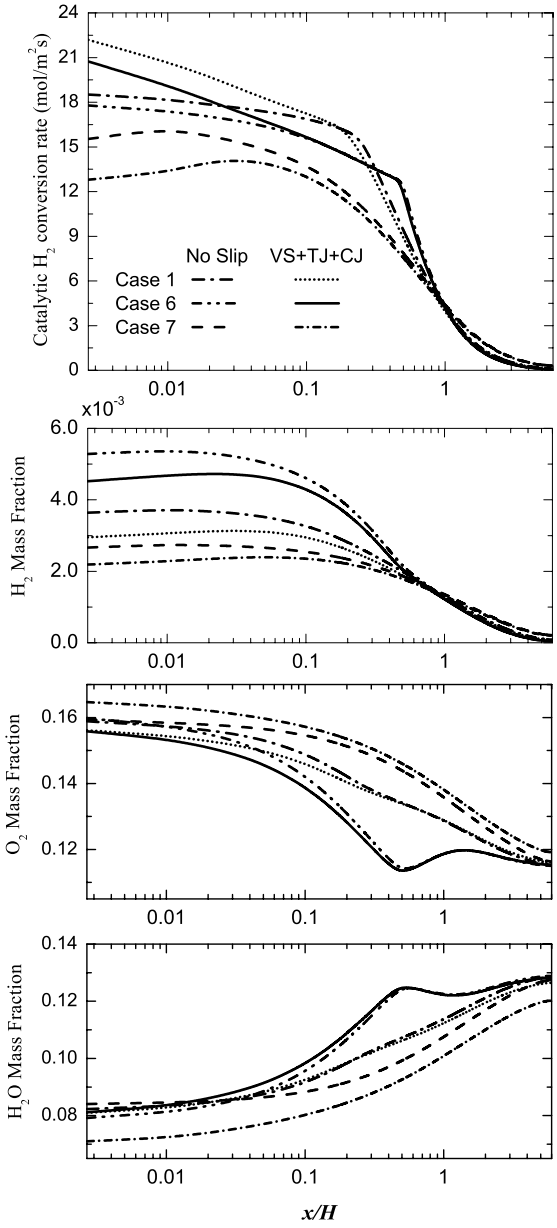

Figure 5.13: Catalytic hydrogen conversion rates and wall mass fractions of H_2, O_2 and H_2O of Cases 1, 6 and 7 along the channel with channel heights of 25, 50 and 10 μm, respectively. The legend applies to all subfigures.

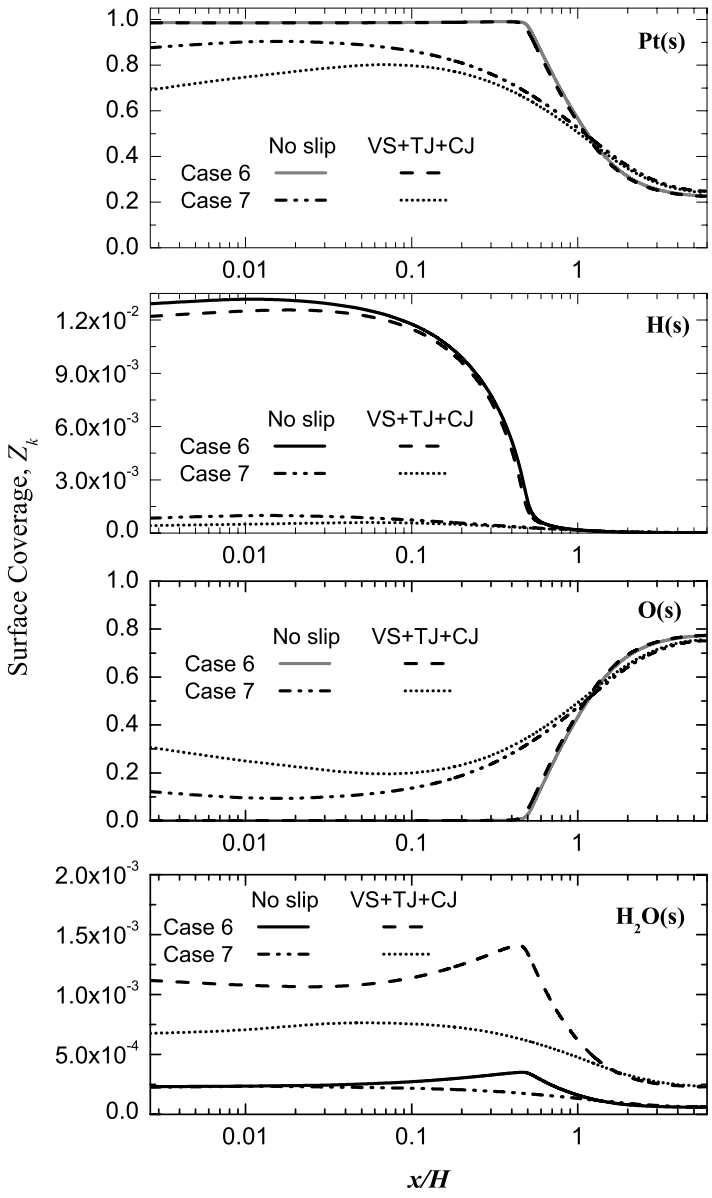

Figure 5.14: Surface species coverage of Pt, H(s), O(s) and H_2O(s) of Cases 6 and 7 with channel heights of 50 and 10 μm, respectively, at the wall with and without slip/jump along the channel.

can occur due to its smaller multicomponent diffusion coefficient. Under the operating conditions of Case 6, this trend continues up to $x/H \approx 0.5$ where the catalytic conversion rate of H_2 (as well as O_2) suddenly drops due to the considerable amount of hydrogen consumed at the wall. From this point on, the diffusion of oxygen from the core of the channel towards the wall compensates for the lack of oxygen which locally increases the O_2 level close to the wall. This effect is not evident in smaller conduits where the diffusion of oxygen is sufficient to transport enough oxygen to the wall for consumption, due to a stronger diffusion effect.

The surface coverage of species is more sensitive to the slip/jump boundary conditions at smaller channel heights as observed in Fig. 5.14. The surface coverages of Pt(s) and O(s) remain almost constant as the slip/jump boundary conditions are introduced for the case with a channel height of 50 μm while the maximum relative change in the surface coverage of H(s) is about 5%. However, the presence of slip/jump at the wall significantly alters the surface coverages of species for a 10 μm channel. For instance, the surface coverage of H(s) is about 45% lower under the "VS+TJ+CJ" boundary condition as compared to the "No Slip" case. As described earlier, the O(s) surface coverage is very sensitive to the H(s) level on the catalytic surface and the predictions of O(s) (and consequently Pt(s) $\approx 1.0 - $ O(s)) are noticeably different with the presence of slip/jump at the wall.

5.3 Ammonia decomposition on Ru

The channel geometry, governing equations, the numerical treatment of the catalytic reactions and the inlet boundary condition (constant mass flux of species) are similar to those described in section 5.2. The production rate of gas phase species and the coverage of surface species on the wall are modeled using a detailed surface reaction mechanism

proposed by Deshmukh *et* al. [21] as shown in Table 5.2.

The forward reaction rate constants for this set of reactions are calculated as:

$$k_{ads,i} = \frac{\gamma_i}{\Gamma^n}\sqrt{\frac{RT}{2\pi w_k}}\exp\left(\frac{-E_i}{RT}\right) \qquad \text{for adsorption} \tag{5.4a}$$

$$k_{fi} = \frac{A_i}{\Gamma^{n-1}}\exp\left(\frac{-E_i}{RT}\right) \qquad \text{for desorption or surface reaction} \tag{5.4b}$$

where $k_{ads,i}$ and γ_i are the rate constant and sticking coefficient of the adsorption reaction "i" involving species "k" , n is the reaction order, A_i is the pre–exponential factor and E_i is the activation energy.

The surface site density of the walls is specified to be $\Gamma = 1.66 \times 10^{-5}$ mole/m^2 simulating a polycrystalline ruthenium coating (based on ruthenium density of $\rho_{\mathrm{Ru}} = 12.45$ g/cm^3) with a surface accommodation coefficient of 1.0. In this section, the inlet gas temperature is assumed to be $T_{in} = 300$ K while the wall temperature T_w is maintained at 1000 K, unless otherwise specified. The flow is mass driven such that the mass flux of each species is constant at the channel inlet. The outlet pressure is assumed to be atmospheric. In all simulations, a channel length of $L = 20H$ is considered. However, due to the low ammonia decomposition rate, this channel length is not enough for complete ammonia consumption. Therefore, in order to handle the outlet boundary properly, the last 25% of the channel is assumed to be inert, allowing the flow, temperature and species fields to develop completely.

Table 5.2: Surface reaction mechanism of ammonia decomposition on ruthenium [21]

No.	Reaction	Sticking coefficient (unitless) or pre–exponential factor [sec^{-1}]	E_a [kcal/mol]
S1	$\mathrm{H_2} + 2\,\mathrm{Ru(s)} \longrightarrow 2\,\mathrm{H(s)}$	$\gamma = 1.0$	1.9
S2	$2\,\mathrm{H(s)} \longrightarrow \mathrm{H_2} + 2\,\mathrm{Ru(s)}$	1.0×10^{13}	23.7
S3	$\mathrm{N_2} + 2\,\mathrm{Ru(s)} \longrightarrow 2\,\mathrm{N(s)}$	$\gamma = 1.0$	14.1
S4	$2\,\mathrm{N(s)} \longrightarrow \mathrm{N_2} + 2\,\mathrm{Ru(s)}$	1.0×10^{13}	37.2
S5	$\mathrm{NH(s)} + \mathrm{Ru(s)} \longrightarrow \mathrm{N(s)} + \mathrm{H(s)}$	1.0×10^{11}	10.4
S6	$\mathrm{N(s)} + \mathrm{H(s)} \longrightarrow \mathrm{NH(s)} + \mathrm{Ru(s)}$	1.0×10^{11}	31.4
S7	$\mathrm{NH_2(s)} + \mathrm{Ru(s)} \longrightarrow \mathrm{NH(s)} + \mathrm{H(s)}$	1.0×10^{11}	19.1
S8	$\mathrm{NH(s)} + \mathrm{H(s)} \longrightarrow \mathrm{NH_2(s)} + \mathrm{Ru(s)}$	1.0×10^{11}	17.4
S9	$\mathrm{NH_3(s)} + \mathrm{Ru(s)} \longrightarrow \mathrm{NH_2(s)} + \mathrm{H(s)}$	1.0×10^{11}	17.5
S10	$\mathrm{NH_2(s)} + \mathrm{H(s)} \longrightarrow \mathrm{NH_3(s)} + \mathrm{Ru(s)}$	1.0×10^{11}	13.2
S11	$\mathrm{NH_3} + \mathrm{Ru(s)} \longrightarrow \mathrm{NH_3(s)}$	$\gamma = 1.0$	0
S12	$\mathrm{NH_3(s)} \longrightarrow \mathrm{NH_3} + \mathrm{Ru(s)}$	1.0×10^{13}	18.2

5.3.1 Results and discussion

In this section, the effects of slip/jump boundary conditions on various field variables are discussed. Pure ammonia enters the channel with an inlet mass flux of $\dot{m}''_{\text{in}} = 2$ kg/m^{2}s while the temperature at the walls are kept constant at $T_w = 1000$ K. Two channel sizes of $H = 15$ μm and $H = 30$ μm are considered here.

Due to the constant mass flux boundary condition imposed at the inlet, the species mass fractions can be different under different wall boundary condition combinations. The inlet mass fractions of NH_3 and H_2 are shown in Fig 5.15 for a $H = 15$ μm channel under different types of wall boundary condition combinations. Right at the channel inlet, due to ammonia consumption in the channel, there exists a positive diffusive mass flux of NH_3 into the channel. In order to keep the total ammonia inlet mass flux constant, the inlet mass fraction of ammonia should be adjusted (lowered) accordingly. On the other hand, the hydrogen and nitrogen produced in the channel can diffuse back towards the channel inlet which results in a negative diffusive mass flux of H_2 and N_2 out of the channel. Since the total mass flux (diffusion + convection) of the reaction products is set equal to zero in the simulations, the outgoing diffusive mass flux of H_2 and N_2 should be balanced by the incoming convective flux, i.e. $\rho Y_{\text{H}_2}\mathbf{U}$ and $\rho Y_{\text{N}_2}\mathbf{U}$, at the inlet. Therefore a finite amount of H_2 and N_2 will exist at the channel inlet despite their zero total inlet mass flux. It is evident that the velocity slip boundary condition alone does not affect the inlet composition. However, the presence of a temperature discontinuity noticeably alters the inlet hydrogen mass fraction especially in regions close to the wall.

The species mass fractions of H_2, N_2 and NH_3 at the edge of the Knudsen layer are shown in Fig. 5.16 for a $H = 15$ μm channel. As observed, the influence of velocity slip on the species mass fractions is minimal. It is due to the fact that the presence of velocity

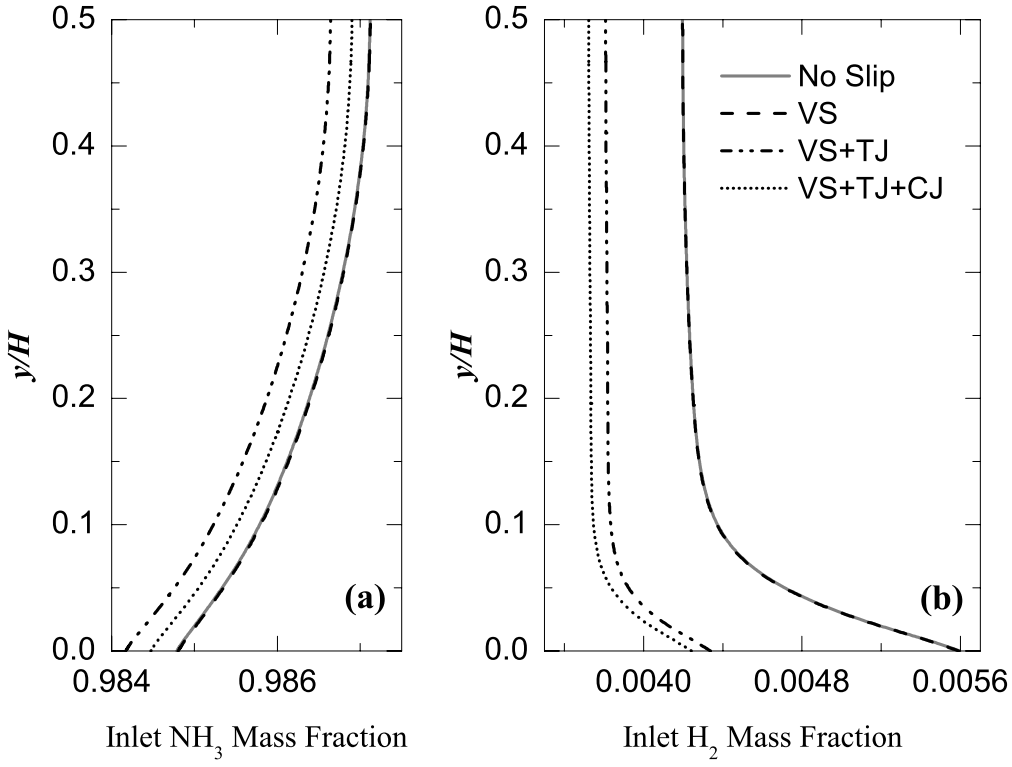

Figure 5.15: Inlet NH_3 and H_2 mass fractions for a $H = 15$ μm channel under different types of wall boundary conditions.

slip alone at the wall does not significantly change the velocity and temperature fields, as discussed in the previous section. The decrease in the hydrogen mass fraction in the "VS+TJ" cases is mainly due to the decreased hydrogen levels at the inlet. The presence of strong axial temperature gradient as a result of temperature discontinuity significantly increases the velocity slip at the edge of the Knudsen layer. The increased slip velocity close to the wall decreases the inlet hydrogen and oxygen mass fractions in this region as observed in Fig 5.15. In addition, the increased near–wall velocity alters the velocity and temperature distributions in the channel. The nitrogen and ammonia mass fractions at the edge of the Knudsen layer remain intact with the introduction of slip/jump boundary

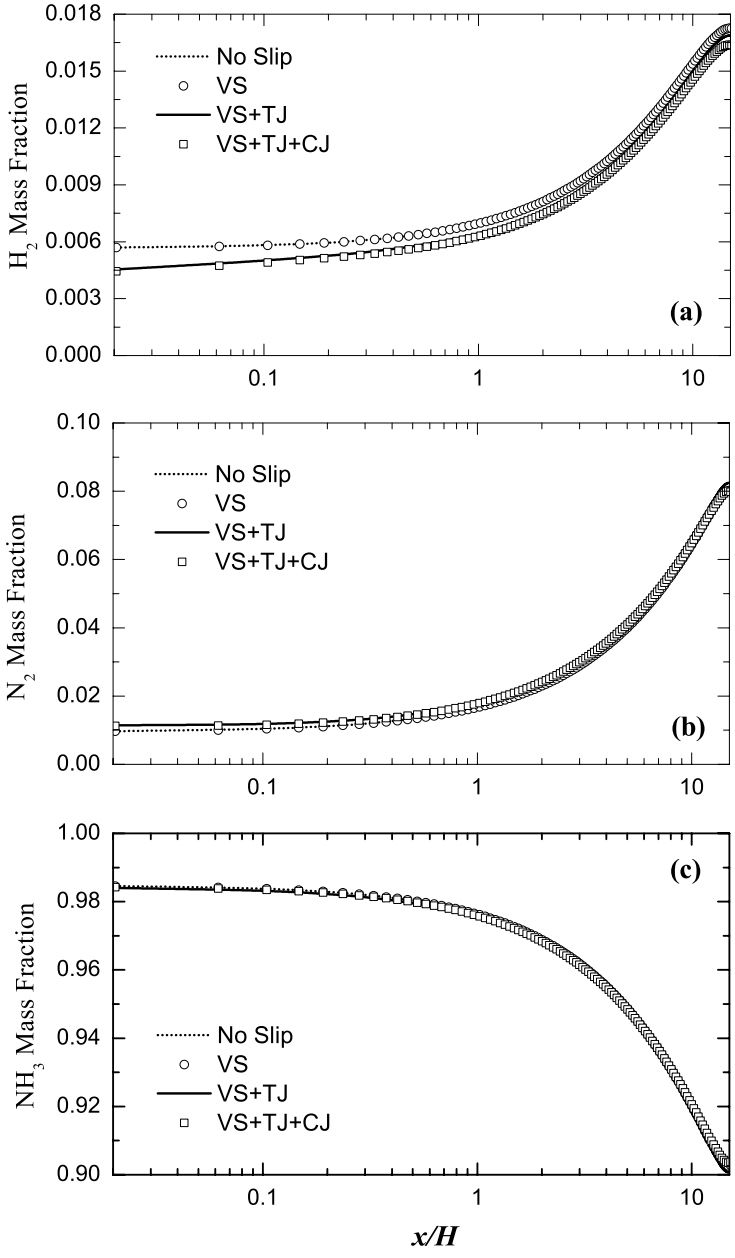

Figure 5.16: (a) H_2, (b) N_2 and (c) NH_3 mass fractions at the edge of the Knudsen layer for a $H = 15$ μm channel under different types of wall boundary conditions.

conditions.

In order to investigate slip/jump effects on species transport, the catalytic production rates of H_2 under various boundary condition combinations are shown in Fig. 5.17. Due to a very low Reynolds number, the transport of species and energy is generally diffusive, and therefore, the velocity slip does not alter the mass and energy transfer significantly. As such, the velocity slip boundary condition alone has a very small impact on the hydrogen production rate. However, the influence of the temperature jump boundary condition is noticeable, especially in the developing region of the $H = 15$ μm channel. The increase in the catalytic hydrogen production due to the presence of temperature discontinuity diminishes as the channel size increases, as observed in Fig. 5.17 (b). This is in accord with the decreased Knudsen number (curtailing slip/jump effects in general) in the larger channel.

The axial temperature gradient at the edge of the Knudsen layer substantially increases the slip velocity, which in turn enhances the convective mass transfer and causes steeper gradients in the vicinity of the wall. As can be inferred from Eq. (2.51) steeper normal gradients (higher diffusion mass flux) increase the species reaction rates $\dot{s}_k$. As the temperature jump boundary condition is introduced, the conversion rate experiences a considerable increase in the developing region and then merges with the no–slip case result further downstream. The presence of concentration discontinuity at the wall, on the other hand, counter balances the increase in hydrogen production rate by reducing the species mass fraction gradient normal to the wall. The decrease in the concentration gradients (and consequently the ammonia diffusive mass flux towards the wall) translates into lower hydrogen production rates as can be readily seen in Eq. (2.51). Lower hydrogen level at the inlet in the presence of temperature discontinuity at the wall also contributes to higher levels of hydrogen production in the case of "TJ".

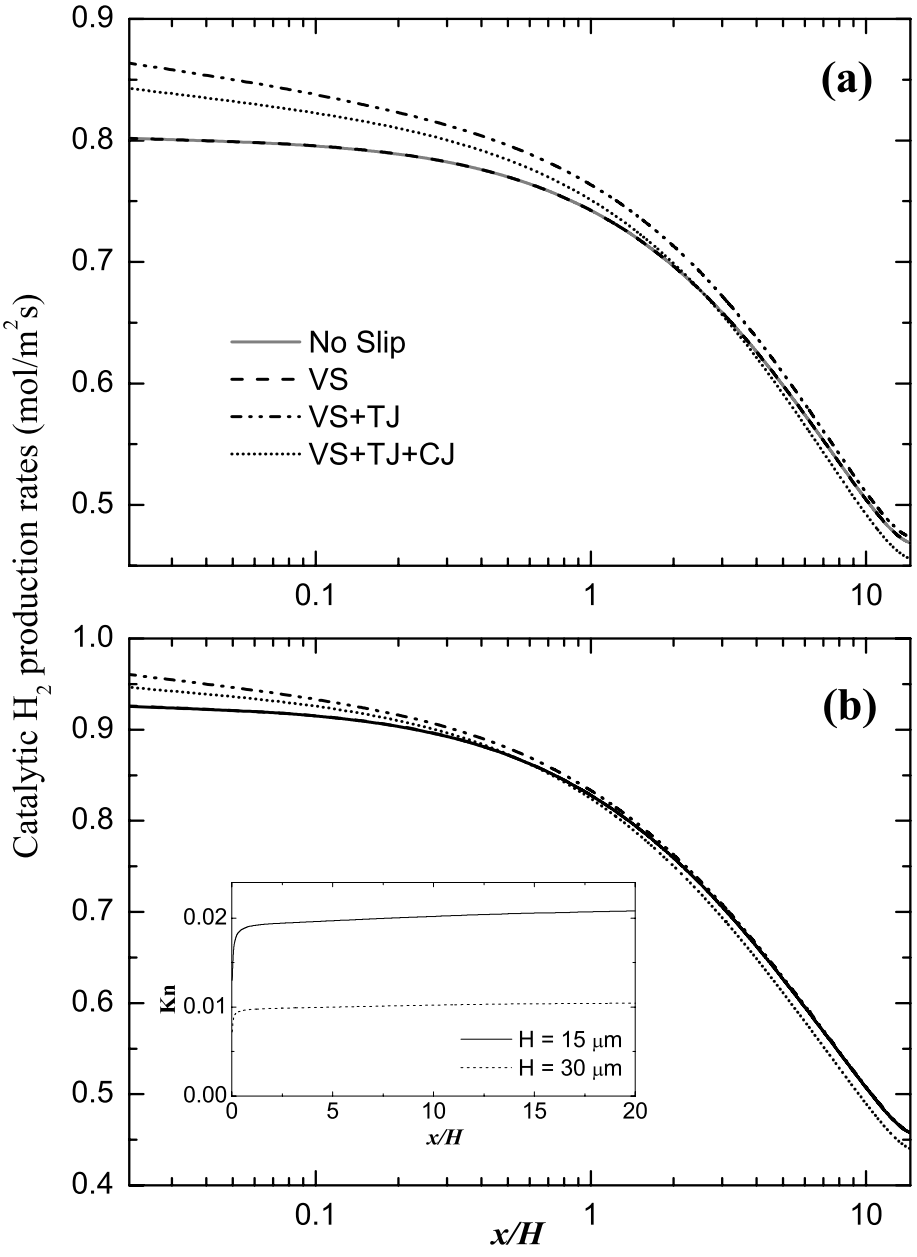

Figure 5.17: Catalytic production rates of H_2 along the channel for (a) $H = 15$ μm and (b) $H = 30$ μm under different types of boundary condition combinations.

Species coverage on the catalytic wall is also influenced by the slip/jump boundary conditions. Figure 5.18 shows the surface coverage Z_k of different species at the wall for a $H = 15$ μm channel. Close to the channel inlet, the surface is dominated by free sites and N(s). As ammonia reacts along the channel, the increased hydrogen in the channel gives rise to H(s) coverage. Although the nitrogen level in the channel is also increased, the adsorbed hydrogen coverage starts increasing at the expense of N(s) due to the much lower activation energy barrier (see Table 5.2). As with other variables before, the velocity slip alone does not influence the surface species coverages. In the presence of temperature jump the change in H(s) and N(s) coverages compared to the "No Slip" case follows the same trend as the mass fractions of H_2 and N_2 at the edge of the Knudsen layer; i.e. slightly lower H(s) and slightly higher N(s) coverages. The available free sites Ru(s) and NH_3(s) are influenced the most by the presence of concentration discontinuity at the wall.

5.4 Conclusions

In this chapter, two distinct problems have been investigated to examine the rarefaction effects on the heat and mass transfer properties of catalytic reactive flows; hydrogen oxidation on platinum and ammonia decomposition on ruthenium.

For both set of reactions, the concentration jump effect on the flow and temperature fields is found to be negligible since the mass–averaged properties of the mixture do not vary considerably. In the range of operating conditions considered in this chapter, the temperature jump boundary condition affects the flow and temperature fields the most. The presence of strong axial temperature gradients at the channel inlet substantially increases the velocity.

In the case of H_2 oxidation on platinum, numerical results show that the thermal

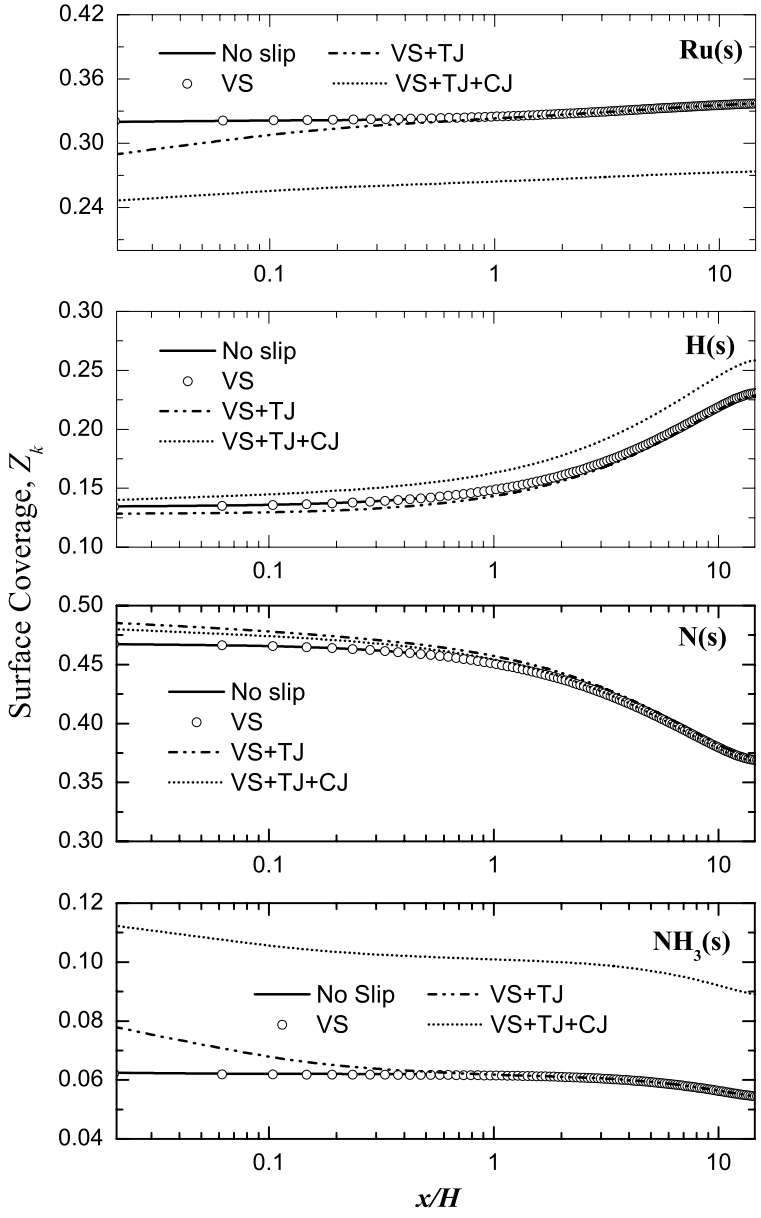

Figure 5.18: Surface species coverage of Ru(s), H(s), N(s) and NH_3(s) for a $H = 15$ μm channel at the wall under different types of wall boundary conditions along the channel.

diffusion effects cannot be neglected especially in the entrance region where the temperature gradients are strong. Due to consumption of hydrogen on the wall the overall H_2 diffusive mass flux is towards the wall. However, In this region, the thermal diffusion effect is the dominant driving force which causes a positive hydrogen concentration gradient towards the wall. Consequently, the numerical predictions of hydrogen consumption at the wall are different when the thermal diffusion term is excluded. The velocity slip boundary condition only slightly influences the species distribution at the edge of the Knudsen layer as well as inside the channel. The temperature jump, on the other hand, affects the species field noticeably. As the temperature jump boundary condition is introduced, the H_2 and O_2 mass fractions at the edge of the Knudsen layer decrease. This is mainly due to reduced mass fractions of these species at the inlet with the increased near–wall velocity due to the introduction of the temperature discontinuity at the wall. Catalytic hydrogen consumption is also affected by the temperature and concentration discontinuity at the wall. Since the hydrogen consumption at the wall is mass transport limited, in the "VS+TJ" case where the velocity increases close to the wall, the hydrogen consumption substantially increases in the entrance region due to increased convective mass transfer. The presence of a concentration discontinuity, however, decreases the catalytic hydrogen conversion due to the reduced concentration gradients at the edge of the Knudsen layer. The presence of a temperature discontinuity at the wall in the form of $(T_w/T_s)^{1/2}$ is the main factor in defining the concentration jump at the edge of the Knudsen layer. Numerical results suggest a strong dependence of catalytic hydrogen consumption on this term. On the other hand, the surface accommodation coefficient appears to have a small effect on the prediction of hydrogen consumption at the wall with slip/jump boundary conditions. As the surface accommodation coefficient is reduced from 1.0 to 0.25, the hydrogen mass fraction at the wall slightly increases. Mass transfer characteristics are influenced as the total inlet mass

flux is altered. Since hydrogen is transported to the wall mostly via diffusion, at lower inlet mass fluxes the combustion process is brought closer to an ideal mass transport limited state with lower hydrogen mass fractions at the wall. Due to weaker gradients, however, the slip/jump effects are diminished as the inlet mass flux is reduced. Detailed numerical simulations in the current work suggest that for precise modeling of rarefied reactive flows, the slip/jump boundary conditions should be included since certain surface or gas phase species concentration values can change with small changes in surface parameters. For instance, the O(s) surface coverage is practically zero for H(s) surface coverage values above a certain limit. However, with the slightest decrease in adsorbed hydrogen concentration, O(s) surface coverage acquires a finite value. The effect of slip/jump boundary conditions on the gas phase mass fractions, surface species coverages and the catalytic conversion rates is affected by the channel height as well. At very small channel heights, the decrease in the catalytic conversion rates due to the presence of concentration jump can eclipse the positive effect of temperature discontinuity on catalytic conversion rates. The impact of slip/jump at the wall on the coverage of surface species is also more pronounced in smaller channel heights.

Ammonia decomposition on ruthenium shows similar behaviour in some aspects. The presence of temperature discontinuity at the wall increases ammonia decomposition and as the channel size decreases, this effect becomes more evident. The presence of concentration discontinuity at the wall, on the other hand, counter balances the increase in hydrogen production rate by reducing the species mass fraction gradient normal to the wall. As the temperature jump boundary condition is introduced, the hydrogen mass fraction at the edge of the Knudsen layer decreases mainly due to the decreased hydrogen levels at the inlet. With the rise in hydrogen level within the channel due to ammonia decomposition, the H(s) surface coverage increases along the channel as well. However, since hydrogen

adsorption has a much lower activation energy barrier, the adsorbed hydrogen coverage starts increasing at the expense of N(s) despite the fact that nitrogen is also being produced in the process.

Chapter 6

Conclusions and future work

6.1 Conclusions

In this thesis a numerical scheme is presented for the simulation of rarefied catalytic reacting gaseous flows in microreactors. To this end, a complete set of velocity–slip, temperature–jump and concentration–jump boundary conditions for multi–component reacting gaseous flows is developed based on the kinetic theory of gases. A numerical colocated finite volume code for the solution of laminar, steady, reacting gas flows is developed to accommodate this set of boundary conditions. Detailed gas phase and surface reaction mechanisms along with a multi–component species diffusion model are used to fully account for the effects of minor species in determining the homogeneous and heterogeneous reaction pathways.

The increased heat and radical losses at the walls can suppress homogeneous reactions to a great extent in sub–millimetre channels. In order to assess the importance of gas phase reactions in these channels, the relative contribution of homogeneous reactions compared to the surface reactions is studied for H_2/air mixtures at different inlet mass fluxes, equivalence

ratios and channel heights. Reducing the channel height decreases the contribution of homogeneous reactions to hydrogen conversion. The decline in homogeneous reaction rates is gradual and is mainly due to the reduced channel volume and increased OH adsorption on the catalytic walls. The radical destruction on the wall continues to inhibit the gas phase reaction even further at smaller channel heights. The upstream diffusion of product species from the channel towards the inlet becomes considerable as the channel size is reduced because of the strong diffusive mass flux at smaller length scales. This leads to the existence of some of the product species at the channel inlet which contributes even further to the decline in the gas phase conversion rate in smaller channels.

Variation of the inlet mass flux at constant channel height alters the balance between the convective and diffusive mass fluxes. At low inlet mass fluxes, the presence of product species suppresses the gas phase reaction rates. As the inlet mass flux of the reacting mixture is increased, initially the amount of H_2 conversion in the gas phase also increases. However, after a certain mass flux, this trend reverses and the increased inlet mass flux leads to lower gas phase conversion. Since the catalytic H_2 conversion is diffusion–limited, it increases steadily as the inlet mass flux is increased mainly due to steeper gradients at the wall. Since the catalytic reaction is dominant in hydrogen conversion, the relative contribution of gas phase reaction to the overall conversion declines rapidly as the inlet mass flux increases. The fuel–air equivalence ratio of the mixture also changes the contribution of the gas phase reactions to the overall hydrogen conversion significantly. At low equivalence ratios, the homogeneous and heterogeneous conversion rates are both low compared to richer mixtures. As the equivalence ratio increases, both gas phase and wall reactions increase, although the rise in the gas phase conversion rate is more vigorous.

In this thesis, non–equilibrium slip/jump effects in catalytic oxidation of lean H_2/air and ammonia decomposition are numerically studied in planar microchannels. The con-

centration jump effect on the velocity and temperature fields is found to be negligible since the mass–averaged properties of the mixture do not vary considerably, while the temperature jump boundary condition affects the velocity and temperature fields the most. The presence of strong axial temperature gradients at the channel inlet substantially increases the slip velocity. Numerical results show that the thermal diffusion effects cannot be neglected especially in the entrance region where the temperature gradients are strong. The velocity slip boundary condition only slightly influences the species distribution at the edge of the Knudsen layer as well as inside the channel. The temperature jump, on the other hand, affects the species field noticeably. Catalytic reaction rates on the wall are also affected by the temperature and concentration discontinuity at the wall. The hydrogen consumption and ammonia decomposition substantially increase in the entrance region due to increased convective mass transfer (high slip velocity close to the wall). The presence of a concentration discontinuity, however, decreases the catalytic reaction rates due to the reduced concentration gradients at the edge of the Knudsen layer, counter balancing the temperature discontinuity effects.

The presence of a temperature discontinuity at the wall in the form of $(T_w/T_s)^{1/2}$ is the main factor in defining the concentration jump at the edge of the Knudsen layer. Numerical results suggest a strong dependence of catalytic reaction rates on this term. On the other hand, the surface accommodation coefficient appears to have a small effect on the prediction of catalytic reaction rates at the wall with slip/jump boundary conditions. Mass transfer characteristics are influenced as the total inlet mass flux is altered. For the hydrogen oxidation on platinum, since hydrogen is transported to the wall mostly via diffusion, at lower inlet mass fluxes the combustion process is brought closer to an ideal mass transport limited state with lower hydrogen mass fractions at the wall. Due to weaker gradients, however, the slip/jump effects are diminished as the inlet mass flux is reduced.

Detailed numerical simulations in the current work suggest that for precise modeling of rarefied reactive flows, the slip/jump boundary conditions should be included since certain surface or gas phase species concentration values can change with small changes in surface parameters. For instance in the hydrogen oxidation case, the O(s) surface coverage is practically zero for H(s) surface coverage values above a certain limit. However, with the slightest decrease in adsorbed hydrogen concentration, O(s) surface coverage acquires a finite value. The effect of slip/jump boundary conditions on the gas phase mass fractions, surface species coverages and the catalytic conversion rates is affected by the channel height as well. At very small channel heights, the decrease in the catalytic conversion rates due to the presence of concentration jump can eclipse the positive effect of temperature discontinuity on catalytic conversion rates. The impact of slip/jump at the wall on the coverage of surface species is also more pronounced in smaller channel heights for both reaction sets.

The present work was focused on the fundamental study of reacting flows in microchannels. The theoretical/numerical methodologies developed in this thesis are applicable to any reacting/non–reacting multicomponent flow in microchannels involving heat and mass transfer with variable physical properties.

6.2 Future work

Based on the current work on catalytic reactive flows in microchannels, the following research is recommended for future study:

- Due to the complex nature of most reactive flows, some of the findings of the present work cannot be easily generalized and extended to other reactions. The current work

clearly demonstrates the methodology for the simulation of catalytic reactive flows in microchannels with slip/jump effects. The rarefaction effects with different catalysts and fuels can be explored subject to availability of reliable chemical kinetics models. Besides, the catalytic oxidation of hydrogen has been extensively studied and numerous chemical schemes have been proposed in the past. The elementary reaction sets utilized in the current work are known to produce the closest theoretical/numerical results to experimental data. However, other surface reaction schemes are also recommended to be analyzed to assess the relative importance of slip/jump effects.

- The numerical code in the present work is validated in different stages. The chemically reacting flow section of the code has been compared against the experimental data for catalytic hydrogen oxidation in a 7 mm high channel. Therefore, experiments are recommended to verify the slip/jump effects, although the channel sizes should be two orders of magnitude smaller. Alternatively, the pressure can be lowered about two orders of magnitude below the atmospheric pressure to study the slip/jump effects which is not a good representative of actual working conditions. For these reasons, the associated experimental difficulties are very significant at such scales.

- The effect of geometry can be further explored to study the rarefaction effects in 3D and more complex configurations. Rectangular channels of different aspect ratios, due to the corner effects, can exhibit a different behaviour. Since the channel heights are generally small, the pressure variation along the channel can be significant as the channel length increases. Therefore, it would be useful to also investigate the effect of channel length on the catalytic reactive flows in microchannels.

- The proposed set of slip/jump boundary conditions are limited to Knudsen numbers below 0.1. For the range of Knudsen numbers beyond 0.1, the Direct Simulation Monte Carlo DSMC method can be used to predict the heat and mass transfer characteristics of catalytic reactive flows. The rarefaction effects in non–reacting flows of multicomponent mixtures were compared to DSMC simulation results. However, the reactive flows can be further studied in smaller channels using the DSMC method.

APPENDICES

Appendix A

Numerical formulation

The governing equations described in previous sections are conservation of mass, momentum and scalar fields such as enthalpy and species concentration. Generally, they can be represented in vector form as:

$$\nabla \cdot (\rho \mathbf{U}) = 0 \tag{A.1}$$

$$\nabla \cdot (\rho \mathbf{U}\mathbf{U}) = -\nabla \left(p + \frac{2}{3}\mu \nabla \cdot \mathbf{U} \right) + \nabla \cdot \left[\mu \left(\nabla \mathbf{U} + \nabla \mathbf{U}^T \right) \right] \tag{A.2}$$

$$\nabla \cdot (\rho \mathbf{U} \phi) = \nabla \cdot (\Gamma_\phi \nabla \phi) + S_\phi \tag{A.3}$$

Here, a general finite volume discretization scheme will be presented for the numerical solution of the above mentioned set of equations. Two general Cartesian control volumes sharing an interior face are shown schematically in Fig. A.1. It should be noted that s is an unsigned quantity denoting the distance, while $\mathbf{r}$ is a vector with specific direction and length. In some cases, the description is general and for the problem in hand, some simplifications might be possible. However, in this appendix, the formulation is kept as general as possible.

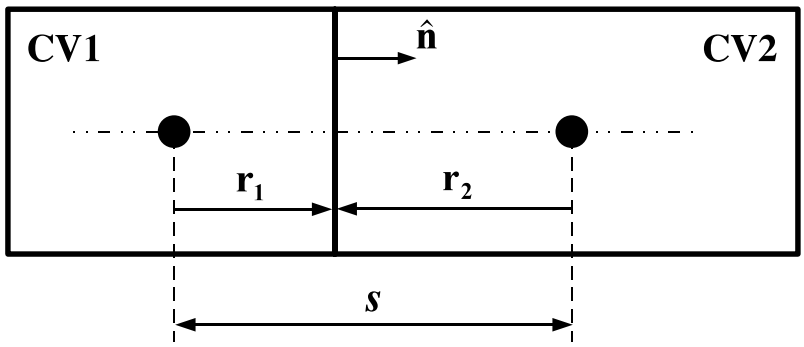

Figure A.1: A generic interior face shared by control volumes CV1 and CV2.

A.1 Discretization of the continuity equation

The differential form of the mass continuity equation, in vector notation, can be written as,

$$\nabla \cdot (\rho \mathbf{U}) = 0 \tag{A.4}$$

Integrating this equation over each control volume and employing the Gauss Divergence Theorem gives the integral form of the continuity equation as,

$$\int_{\mathrm{CV}} \nabla \cdot (\rho \mathbf{U}) \; dV = \int_{\mathrm{CS}} \rho \mathbf{U} \cdot \hat{\mathbf{n}} \, dA = 0 \tag{A.5}$$

where $\hat{\mathbf{n}}$ is the unit normal vector to the control volume surface. Assuming that the control volumes are polygonal, the above integral can be written as the sum of mass flux across each face as,

$$\sum_{\text{faces}} J_{\text{vol}} = \sum_{\text{faces}} \rho \tilde{U}_n A_f = 0 \tag{A.6}$$

in which $\tilde{U}_n$ is the face normal advecting velocity which is considered to carry mass. In this equation, ρ and $\tilde{U}_n$ are evaluated at the face and should be properly discretized. In the

current work, the velocity-pressure coupling is achieved through the formulation proposed by Rhie and Chow [82] in order to discretize the advecting velocity.

A.1.1 Mass flux across interior faces

Since the pressure does not appear in the continuity equation, the treatment of the coupling between pressure and velocity needs special attention. In order to avoid the checkerboard (solution decoupling) problem in the solution of the momentum and mass equations, the flow across the face is discretized using the Rhie and Chow velocity-pressure interpolation as [82],

$$\tilde{U}_n = \bar{U}_n - \hat{d}_f \left(\left.\frac{\partial p}{\partial n}\right|_{\text{face}}^{\text{active}} - \left.\frac{\partial p}{\partial n}\right|_{\text{face}}^{\text{lagged}} \right) \tag{A.7}$$

in which $\bar{U}_n$ represents the velocity that carries momentum, called the advected velocity. The advected velocity on the face is discretized using the second order accurate central differencing scheme between control volumes 1 and 2, sharing the face, as:

$$\bar{U}_n = \frac{1}{2}\left(U_{n1} + U_{n2}\right)^m + \frac{1}{4}\left(\nabla U_{n1} + \nabla U_{n2}\right)^{m-1} . \left(\mathbf{r}_1 + \mathbf{r}_2\right) \tag{A.8}$$

In the above relation, indices $m-1$ and m represent the previous and current steps in the iterative solution algorithm, respectively. Pressure dissipation coefficient $\hat{d}_f$ is defined as [82]:

$$\hat{d}_f = \frac{1}{2}\left(\frac{\mathcal{V}_1}{a_1} + \frac{\mathcal{V}_2}{a_2}\right) \tag{A.9}$$

where and $\mathcal{V}_1$ and $\mathcal{V}_2$ are volumes and a_1 and a_2 are the average coefficients of the momentum equation corresponding to control volumes 1 and 2, respectively. The active and lagged normal pressure gradients are evaluated at the current and previous iteration, respectively,

as follow

$$\left.\frac{\partial p}{\partial n}\right|_{\text{face}}^{\text{active}} = \left(\frac{p_2 - p_1}{s}\right)^m \tag{A.10a}$$

$$\left.\frac{\partial p}{\partial n}\right|_{\text{face}}^{\text{lagged}} = \frac{1}{2}\left(\nabla p_1 + \nabla p_2\right)^{m-1} \cdot \hat{\mathbf{n}} \tag{A.10b}$$

Physical properties of the fluid can also depend on the solution which makes the system of equations non–linear. Therefore, these properties should be calculated using the solution of the previous iteration. Density ρ on the face can therefore be evaluated as:

$$\rho_f = \frac{1}{2}\left(\rho_1 + \rho_2\right)^{m-1} + \frac{1}{4}\left(\nabla\rho_1 + \nabla\rho_2\right)^{m-1} \cdot \left(\mathbf{r}_1 + \mathbf{r}_2\right) \tag{A.11}$$

Putting the discretized values back into the definition of mass flux across interior faces yields,

$$\begin{aligned} J_{\text{vol}}^{\text{int}} &= \frac{\rho_f A_f}{2}\left(\mathbf{U}_1 + \mathbf{U}_2\right)^m \cdot \hat{\mathbf{n}} + \hat{d}_f \rho_f A_f \left[\frac{\left(p_1 - p_2\right)^m}{s} + \frac{1}{2}\left(\nabla p_1 + \nabla p_2\right)^{m-1} \cdot \hat{\mathbf{n}}\right] \\ &\quad \frac{\rho_f A_f}{4}\left(\nabla U_{n1} + \nabla U_{n2}\right)^{m-1} \cdot \left(\mathbf{r}_1 + \mathbf{r}_2\right) \end{aligned} \tag{A.12}$$

A.1.2 Boundary faces

The treatment of fluxes across boundaries is somehow different than the interior faces due to different types of boundary conditions. In the following subsections, fluxes across different boundary faces will be discussed.

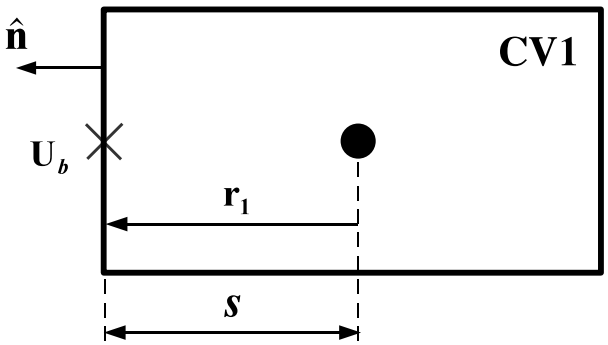

Figure A.2: Schematic of a generic inflow/wall boundary face.

Inflow and wall boundary conditions

In the case of inflow boundary or prescribed velocity on the wall (slip or no-slip) boundary conditions, the flow velocity at the boundary face is prescribed. A general inflow/wall boundary face is shown in Fig. A.2.

In this case, the flux across the boundary face can be written as:

$$J_{\text{vol}}^{\text{in}} = \rho_{\text{in}} U_n A_f = \rho_{\text{in}} \left(\mathbf{U}_b \cdot \hat{\mathbf{n}} \right) A_f \tag{A.13}$$

In the case of no-slip wall, the fluid velocity is equal to that of wall; however, if there exists a velocity slip on the wall, the fluid velocity should be corrected using the proper slip boundary condition.

Outflow boundary condition

For the outflow boundary condition, it is assumed that the pressure is prescribed on the boundary face, and therefore, the velocity should be calculated properly. A general outflow

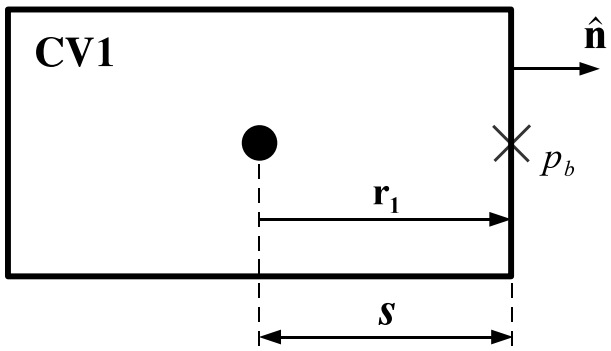

Figure A.3: Schematic of a generic outflow boundary face.

boundary face is shown in Fig. A.3. In this case, the advecting velocity can be written as:

$$\tilde{U}_n = U_{n1}^m + \nabla U_{n1}^{m-1} \cdot \mathbf{r}_1 - \hat{d}_f \left[\frac{p_b - p_1}{s} - (\nabla p_1 \cdot \hat{\mathbf{n}})^{m-1} \right] \tag{A.14}$$

which upon substitution into the face flux relation, will result in:

$$\begin{aligned} J_{\text{vol}}^{\text{out}} &= \rho_{\text{out}} A_f \mathbf{U}^m \cdot \hat{\mathbf{n}} + \frac{\hat{d}_f \rho_{\text{out}} A_f}{s} \left(p_1^m - p_b \right) + \\ &\quad \rho_{\text{out}} A_f \nabla \left(\mathbf{U}^{m-1} \cdot \hat{\mathbf{n}} \right) \cdot \mathbf{r}_1 + \hat{d}_f \rho_{\text{out}} A_f \left(\nabla p_1 \cdot \hat{\mathbf{n}} \right)^{m-1} \end{aligned} \tag{A.15}$$

Symmetry boundary condition

By definition, the volumetric flux across a symmetry boundary condition is identically equal to zero,

$$J_{\text{vol}}^{\text{sym}} = 0 \tag{A.16}$$

A.2 Discretization of the momentum equation

The differential form of the momentum equation, in vector notation, can be written as:

$$\nabla \cdot (\rho \mathbf{U}\mathbf{U}) = -\nabla \left(p + \frac{2}{3}\mu \nabla \cdot \mathbf{U} \right) + \nabla \cdot \left[\mu \left(\nabla \mathbf{U} + \nabla \mathbf{U}^T \right) \right] \tag{A.17}$$

Integrating the above equation over each control volume and applying the Divergence theorem results in the integral form of the momentum equation as:

$$\begin{aligned} \sum_{\text{faces}} \int_{\text{face}} (\rho \mathbf{U}\mathbf{U}) \cdot \hat{\mathbf{n}} \, dA \;\; &+ \;\; \sum_{\text{faces}} \int_{\text{face}} \left(p + \frac{2}{3}\mu \nabla \cdot \mathbf{U} \right) \hat{n} \, dA \\ &- \;\; \sum_{\text{faces}} \int_{\text{face}} \mu \left(\nabla \mathbf{U} + \nabla \mathbf{U}^T \right) \cdot \hat{\mathbf{n}} \, dA = 0 \end{aligned} \tag{A.18}$$

In order to discretize the above equation, the values of dependent variables u, v and p and their derivatives should be approximated using the cell values. In the following sections, the discretized form of the x and y momentum equations will be presented for interior as well as boundary faces.

A.2.1 Momentum flux across interior faces

Considering a general control volume as shown in Fig. A.1, the x component of the momentum flux on each face can be written as:

$$\begin{aligned} J_{\text{x-mom}} \;\; = \;\; & \int_{\text{face}} \left(\rho \tilde{U}_n \right) u \, dA + \\ & \int_{\text{face}} \left(p + \frac{2}{3}\mu \nabla \cdot \mathbf{U} \right) n_x \, dA - \int_{\text{face}} \mu \left(\nabla u + \frac{\partial \mathbf{U}}{\partial x} \right) \cdot \hat{\mathbf{n}} \, dA \end{aligned} \tag{A.19}$$

in which,

$$u|_{\text{face}}^{\text{int}} = u_{\text{up}}^{m} + \nabla u_{\text{up}}^{m-1} \cdot \mathbf{r}_{\text{up}} \tag{A.20a}$$

$$p|_{\text{face}}^{\text{int}} = \frac{1}{2}\left(p_1 + p_2\right)^m + \frac{1}{4}\left(\nabla p_1 + \nabla p_2\right)^{m-1} \cdot \left(\mathbf{r}_1 + \mathbf{r}_2\right) \tag{A.20b}$$

$$\nabla \cdot \mathbf{U}|_{\text{face}}^{\text{int}} = \frac{1}{2}\left[\left(\frac{\partial u_1}{\partial x} + \frac{\partial u_2}{\partial x}\right) + \left(\frac{\partial v_1}{\partial y} + \frac{\partial v_2}{\partial y}\right)\right]^{m-1} \tag{A.20c}$$

$$\nabla u \cdot \hat{\mathbf{n}}|_{\text{face}}^{\text{int}} = \left(\frac{u_2 - u_1}{s}\right)^m \tag{A.20d}$$

$$\frac{\partial \mathbf{U}}{\partial x} \cdot \hat{\mathbf{n}}\bigg|_{\text{face}}^{\text{int}} = \frac{1}{2}\left[\left(\frac{\partial u_1}{\partial x} + \frac{\partial u_2}{\partial x}\right) n_x + \left(\frac{\partial v_1}{\partial x} + \frac{\partial v_2}{\partial x}\right) n_y\right]^{m-1} \tag{A.20e}$$

$$\mu|_{\text{face}}^{\text{int}} = \frac{1}{2}\left(\mu_1 + \mu_2\right)^{m-1} + \frac{1}{4}\left(\nabla \mu_1 + \nabla \mu_2\right)^{m-1} \cdot \left(\mathbf{r}_1 + \mathbf{r}_2\right) \tag{A.20f}$$

The second order upwind scheme (Linear Deferred Correction) is employed to discretize the convective terms. The upwind node is denoted by subscript "up" and the gradient from the previous iteration is used to add a linear correction in approximating the face values. Therefore, the momentum flux in the x direction can be written in the discretized form as:

$$\begin{aligned} J_{\text{x-mom}}^{\text{int}} \;=\; & J_{\text{vol}}^{\text{int}}\, u_{\text{up}}^{m} + \frac{A_f \mu_f}{s}\left(u_1 - u_2\right)^m + \frac{A_f n_x}{2}\left(p_1 + p_2\right)^m + \\ & J_{\text{vol}}^{\text{int}}\left(\nabla u_{\text{up}} \cdot \mathbf{r}_{\text{up}}\right)^{m-1} + \frac{A_f n_x}{4}\left(\nabla p_1 + \nabla p_2\right)^{m-1} \cdot \left(\mathbf{r}_1 + \mathbf{r}_2\right) - \\ & \frac{A_f \mu_f}{2}\left[\left(\frac{\partial u_1}{\partial x} + \frac{\partial u_2}{\partial x}\right) n_x + \left(\frac{\partial v_1}{\partial x} + \frac{\partial v_2}{\partial x}\right) n_y\right]^{m-1} + \\ & \frac{A_f \mu_f n_x}{3}\left[\left(\frac{\partial u_1}{\partial x} + \frac{\partial u_2}{\partial x}\right) + \left(\frac{\partial v_1}{\partial y} + \frac{\partial v_2}{\partial y}\right)\right]^{m-1} \end{aligned} \tag{A.21}$$

In the same manner, the y component of the momentum flux across an interior face

can be written as:

$$
\begin{aligned}
J_{\mathrm{y-mom}} &= \int_{\mathrm{face}} \left(\rho \tilde{U}_n\right) v \, dA + \\
&\int_{\mathrm{face}} \left(p + \frac{2}{3}\mu \nabla \cdot \mathbf{U}\right) n_y \, dA - \int_{\mathrm{face}} \mu \left(\nabla v + \frac{\partial \mathbf{U}}{\partial y}\right) \cdot \hat{\mathbf{n}} \, dA
\end{aligned} \tag{A.22}
$$

Following the same discretization sequence, the final form of the momentum flux in the y direction reads:

$$
\begin{aligned}
J^{\mathrm{int}}_{\mathrm{y-mom}} &= J^{\mathrm{int}}_{\mathrm{vol}} \, v^m_{\mathrm{up}} + \frac{A_f \mu_f}{s} \left(v_1 - v_2\right)^m + \frac{A_f n_y}{2} \left(p_1 + p_2\right)^m + \\
&J^{\mathrm{int}}_{\mathrm{vol}} \left(\nabla v_{\mathrm{up}} \cdot \mathbf{r}_{\mathrm{up}}\right)^{m-1} + \frac{A_f n_y}{4} \left(\nabla p_1 + \nabla p_2\right)^{m-1} \cdot \left(\mathbf{r}_1 + \mathbf{r}_2\right) - \\
&\frac{A_f \mu_f}{2} \left[\left(\frac{\partial u_1}{\partial y} + \frac{\partial u_2}{\partial y}\right) n_x + \left(\frac{\partial v_1}{\partial y} + \frac{\partial v_2}{\partial y}\right) n_y\right]^{m-1} + \\
&\frac{A_f \mu_f n_y}{3} \left[\left(\frac{\partial u_1}{\partial x} + \frac{\partial u_2}{\partial x}\right) + \left(\frac{\partial v_1}{\partial y} + \frac{\partial v_2}{\partial y}\right)\right]^{m-1}
\end{aligned} \tag{A.23}
$$

A.2.2 Momentum flux across boundary faces

The momentum flux across boundary faces should be discretized depending on the type of boundary condition. In the following subsections, different boundary conditions and their corresponding momentum flux treatments will be discussed.

Wall boundary condition

The common boundary condition for the wall is the so-called no-slip condition, in which the fluid velocity is assumed to be equal to that of the wall. However, in the current work, the velocity slip can exist on the wall. For the sake of generality, the fluid velocity at the

fluid-wall interface is denoted by $\mathbf{U}_b$ which can be prescribed (in the case of no–slip) or dependent on flow field, composition and temperature distribution. This type of boundary condition is schematically shown in Fig. A.2.

For the wall boundary condition, it is easier to resolve the momentum flux in the wall–normal and wall–tangential coordinate system. Recalling the total momentum flux across an arbitrary face:

$$\mathbf{J}_{\text{mom}} = \int_{\text{face}} \left(\rho \tilde{U}_n\right) \mathbf{U}\, dA + \int_{\text{face}} \left(p + \frac{2}{3}\mu \nabla \cdot \mathbf{U}\right) \hat{\mathbf{n}}\, dA - \int_{\text{face}} \mu \left(\nabla \mathbf{U} + \nabla \mathbf{U}^T\right) \cdot \hat{\mathbf{n}}\, dA \quad \text{(A.24)}$$

the normal component of momentum flux will be:

$$\begin{aligned} J_{\text{n}-\text{mom}} &= \mathbf{J}_{\text{mom}} \cdot \hat{\mathbf{n}} \\ &= \int_{\text{face}} \left[\rho \tilde{U}_n U_n + p + \frac{2}{3}\mu \nabla \cdot \mathbf{U} - \mu \left(\nabla \mathbf{U} + \nabla \mathbf{U}^T\right) : (\hat{\mathbf{n}} \otimes \hat{\mathbf{n}})\right] dA \end{aligned} \quad \text{(A.25)}$$

where the operator $\otimes$ is the dyadic product of two vectors:

$$\mathbf{a} \otimes \mathbf{b} = \begin{pmatrix} a_x \\ a_y \end{pmatrix} \begin{pmatrix} b_x & b_y \end{pmatrix} = \begin{pmatrix} a_x b_x & a_x b_y \\ a_y b_x & a_y b_y \end{pmatrix} \quad \text{(A.26)}$$

and operator (:) is the Frobenius inner product of two matrices:

$$A : B = \begin{pmatrix} A_{11} & A_{12} \\ A_{21} & A_{22} \end{pmatrix} : \begin{pmatrix} B_{11} & B_{12} \\ B_{21} & B_{22} \end{pmatrix} = A_{11}B_{11} + A_{12}B_{12} + A_{21}B_{21} + A_{22}B_{22} \quad \text{(A.27)}$$

Therefore, in the normal/tangential coordinate system, the last term in Eq. (A.25)

which represent the wall-normal viscous stress can be evaluated as:

$$\left(\nabla\mathbf{U}+\nabla\mathbf{U}^T\right):(\hat{\mathbf{n}}\otimes\hat{\mathbf{n}})=\begin{pmatrix}2\dfrac{\partial U_n}{\partial n} & \dfrac{\partial U_n}{\partial t}+\dfrac{\partial U_t}{\partial n}\\ \dfrac{\partial U_t}{\partial n}+\dfrac{\partial U_n}{\partial t} & 2\dfrac{\partial U_t}{\partial t}\end{pmatrix}:\begin{pmatrix}1 & 0\\ 0 & 0\end{pmatrix}=2\frac{\partial U_n}{\partial n} \tag{A.28}$$

in which subscripts n and t correspond to the wall–normal and wall–tangential directions, respectively. The walls in the current study are not porous, and therefore, the wall–normal component of velocity is zero. Thus, the wall–normal momentum flux can be expressed as:

$$J^{\text{wall}}_{\text{n}-\text{mom}}=\int_{\text{face}}\left[\left(p+\frac{2}{3}\mu\nabla\cdot\mathbf{U}\right)-2\mu\frac{\partial U_n}{\partial n}\right]\,dA \tag{A.29}$$

Similarly, the tangential component of the momentum flux can be written as:

$$J_{\text{t}-\text{mom}}=\mathbf{J}_{\text{mom}}\cdot\hat{\mathbf{t}}=\int_{\text{face}}\left[\rho\tilde{U}_nU_t-\mu\left(\nabla\mathbf{U}+\nabla\mathbf{U}^T\right):\left(\hat{\mathbf{t}}\otimes\hat{\mathbf{n}}\right)\right]\,dA \tag{A.30}$$

The last term in the bracket is the viscous shear stress on the wall which can be simplified as:

$$\left(\nabla\mathbf{U}+\nabla\mathbf{U}^T\right):\left(\hat{\mathbf{t}}\otimes\hat{\mathbf{n}}\right)=\begin{pmatrix}2\dfrac{\partial U_n}{\partial n} & \dfrac{\partial U_n}{\partial t}+\dfrac{\partial U_t}{\partial n}\\ \dfrac{\partial U_t}{\partial n}+\dfrac{\partial U_n}{\partial t} & 2\dfrac{\partial U_t}{\partial t}\end{pmatrix}:\begin{pmatrix}0 & 0\\ 1 & 0\end{pmatrix}=\frac{\partial U_t}{\partial n}+\frac{\partial U_n}{\partial t} \tag{A.31}$$

As stated before, since the wall is not porous, the variation of the wall–normal component of velocity along the wall $\partial U_n/\partial t$ is zero. Therefore, the tangential momentum flux

on the wall can be expressed as:

$$J^{\text{wall}}_{\text{t-mom}} = \int_{\text{face}} -\mu \frac{\partial U_t}{\partial n}\, dA \tag{A.32}$$

Now the x and y components of the momentum flux can be evaluated using the normal and tangential components of momentum flux on each face:

$$\mathbf{J}^{\text{wall}}_{\text{mom}} = \int_{\text{face}} \left[\left(p + \frac{2}{3}\mu \nabla \cdot \mathbf{U} \right) \hat{\mathbf{n}} - 2\mu \frac{\partial U_n}{\partial n}\, \hat{\mathbf{n}} - \mu \frac{\partial U_t}{\partial n}\, \hat{\mathbf{t}} \right] dA \tag{A.33}$$

In order to discretize the momentum equation in the x and y directions, the value of each term in the above equation should be calculated at the cell face as:

$$p|^{\text{wall}}_{\text{face}} = p_1^m + \nabla p_1^{m-1} \cdot \mathbf{r}_1 \tag{A.34a}$$

$$\left.\frac{\partial U_n}{\partial n}\right|^{\text{wall}}_{\text{face}} = \frac{\partial}{\partial n}\left(\mathbf{U} \cdot \hat{\mathbf{n}}\right) = \frac{\partial}{\partial n}\left(u n_x + v n_y\right) = n_x \frac{\partial u}{\partial n} + n_y \frac{\partial v}{\partial n} = \left(\frac{\mathbf{U}_b - \mathbf{U}_1^m}{s} \right) \cdot \hat{\mathbf{n}} \tag{A.34b}$$

$$\left.\frac{\partial U_t}{\partial n}\right|^{\text{wall}}_{\text{face}} = \frac{\partial}{\partial n}\left(\mathbf{U} \cdot \hat{\mathbf{t}}\right) = \frac{\partial}{\partial n}\left(u t_x + v t_y\right) = t_x \frac{\partial u}{\partial n} + t_y \frac{\partial v}{\partial n} = \left(\frac{\mathbf{U}_b - \mathbf{U}_1^m}{s} \right) \cdot \hat{\mathbf{t}} \tag{A.34c}$$

$$\left.\frac{\partial U_t}{\partial t}\right|^{\text{wall}}_{\text{face}} = \nabla \mathbf{U}_1^{m-1} : \left(\hat{\mathbf{t}} \otimes \hat{\mathbf{t}}\right) \tag{A.34d}$$

The x and y components of the momentum flux on the wall can be calculated by substituting these relations into Eq. (A.33) as:

$$\begin{aligned} J^{\text{wall}}_{\text{x-mom}} \;=\; & n_x A_f p_1^m + \frac{4 A_f \mu_f n_x}{3s} \left(\mathbf{U}_1^m - \mathbf{U}_b\right) \cdot \hat{\mathbf{n}} + \frac{A_f \mu_f t_x}{s} \left(\mathbf{U}_1^m - \mathbf{U}_b\right) \cdot \hat{\mathbf{t}} + \\ & A_f n_x \nabla p_1^{m-1} \cdot \mathbf{r}_1 + \frac{2 A_f \mu_f n_x}{3} \nabla \mathbf{U}_1^{m-1} : \left(\hat{\mathbf{t}} \otimes \hat{\mathbf{t}}\right) \end{aligned} \tag{A.35}$$

$$J^{\text{wall}}_{\text{y-mom}} = n_y A_f p_1^m + \frac{4A_f\mu_f n_y}{3s}\left(\mathbf{U}_1^m - \mathbf{U}_b\right)\cdot\hat{\mathbf{n}} + \frac{A_f\mu_f t_y}{s}\left(\mathbf{U}_1^m - \mathbf{U}_b\right)\cdot\hat{\mathbf{t}} + A_f n_y \nabla p_1^{m-1}\cdot\mathbf{r}_1 + \frac{2A_f\mu_f n_y}{3}\nabla\mathbf{U}_1^{m-1} : \left(\hat{\mathbf{t}}\otimes\hat{\mathbf{t}}\right) \tag{A.36}$$

Inflow boundary condition

Similar to the wall boundary condition, the inlet velocity is also prescribed. The pressure on the face, however, should be extrapolated using the cell mean value. The x component of momentum flux is written as:

$$J_{\text{x-mom}} = \int_{\text{face}}\left(\rho\tilde{U}_n\right)u\,dA + \int_{\text{face}}\left(p + \frac{2}{3}\mu\nabla\cdot\mathbf{U}\right)n_x\,dA - \int_{\text{face}}\mu\left(\nabla u + \frac{\partial\mathbf{U}}{\partial x}\right)\cdot\hat{\mathbf{n}}\,dA \tag{A.37}$$

where at the inflow boundary face, the following relations can be employed:

$$u|^{\text{in}}_{\text{face}} = u_{\text{in}} \tag{A.38a}$$

$$p|^{\text{in}}_{\text{face}} = p_1^m + \nabla p_1^{m-1}\cdot\mathbf{r}_1 \tag{A.38b}$$

$$\nabla\cdot\mathbf{U}|^{\text{in}}_{\text{face}} = \frac{u_{\text{in}} - u_1^m}{s} + \left(\frac{\partial v}{\partial y}\right)^{m-1} \tag{A.38c}$$

$$\nabla u\cdot\hat{\mathbf{n}}|^{\text{in}}_{\text{face}} = \frac{u_1^m - u_{\text{in}}}{s} \tag{A.38d}$$

$$\frac{\partial\mathbf{U}}{\partial x}\cdot\hat{\mathbf{n}}\Big|^{\text{in}}_{\text{face}} = \nabla\mathbf{U}_1^{m-1} : \left(\hat{\mathbf{n}}\otimes\hat{\mathbf{i}}\right) \tag{A.38e}$$

which upon substitution in Eq. (A.37) will result in the discretized form as:

$$\begin{aligned} J^{\text{in}}_{\text{x-mom}} &= n_x A_f p_1^m + \left(\frac{A_f \mu_f}{s} + \frac{2A_f \mu_f n_x}{3s}\right) u_1^m + \\ &\left(J^{\text{in}}_{\text{vol}} - \frac{A_f \mu_f}{s} - \frac{2A_f \mu_f n_x}{3s}\right) u_{\text{in}} + A_f n_x \nabla p_1^{m-1} \cdot \mathbf{r}_1 - \\ &A_f \mu_f \nabla \mathbf{U}_1^{m-1} : \left(\hat{\mathbf{n}} \otimes \hat{\mathbf{i}}\right) + \frac{2A_f \mu_f n_x}{3} \left(\frac{\partial v}{\partial y}\right)^{m-1} \end{aligned} \tag{A.39}$$

In the same manner, the discretized form of momentum equation in the y direction for an inflow face can be expressed as:

$$\begin{aligned} J^{\text{in}}_{\text{y-mom}} &= n_y A_f p_1^m + \frac{A_f \mu_f}{s} v_1^m + \frac{2A_f \mu_f n_y}{3s} u_1^m + \\ &\left(J^{\text{in}}_{\text{vol}} - \frac{A_f \mu_f}{s}\right) v_{\text{in}} - \frac{2A_f \mu_f n_y}{3s} u_{\text{in}} + A_f n_y \nabla p_1^{m-1} \cdot \mathbf{r}_1 - \\ &A_f \mu_f \nabla \mathbf{U}_1^{m-1} : \left(\hat{\mathbf{n}} \otimes \hat{\mathbf{j}}\right) + \frac{2A_f \mu_f n_y}{3} \left(\frac{\partial v}{\partial y}\right)^{m-1} \end{aligned} \tag{A.40}$$

Outflow boundary condition

The treatment of the outflow boundary faces is similar to interior faces. A generic outflow boundary face is shown schematically in Fig. A.3. It is assumed that the pressure is prescribed at the outflow boundary as p_{out}. The x component of momentum flux is written as,

$$\begin{aligned} J_{\text{x-mom}} &= \int_{\text{face}} \left(\rho \tilde{U}_n\right) u \, dA + \\ &\int_{\text{face}} \left(p + \frac{2}{3}\mu \nabla \cdot \mathbf{U}\right) n_x \, dA - \int_{\text{face}} \mu \left(\nabla u + \frac{\partial \mathbf{U}}{\partial x}\right) \cdot \hat{\mathbf{n}} \, dA \end{aligned} \tag{A.41}$$

At the outflow boundary face, the following relations can be employed:

$$u|_{\text{face}}^{\text{out}} = u_1^m + \nabla u_1^{m-1} \cdot \mathbf{r}_1 \tag{A.42a}$$

$$p|_{\text{face}}^{\text{out}} = p_{out} \tag{A.42b}$$

$$\nabla \cdot \mathbf{U}|_{\text{face}}^{\text{out}} = \left[\left(\frac{\partial u}{\partial x} \right) + \left(\frac{\partial v}{\partial y} \right) \right]^{m-1} \tag{A.42c}$$

$$\nabla u \cdot \hat{\mathbf{n}}|_{\text{face}}^{\text{out}} = \nabla u_1^{m-1} \cdot \hat{\mathbf{n}} \tag{A.42d}$$

$$\frac{\partial \mathbf{U}}{\partial x} \cdot \hat{\mathbf{n}} \bigg|_{\text{face}}^{\text{out}} = \nabla \mathbf{U}_1^{m-1} : \left(\hat{\mathbf{n}} \otimes \hat{\mathbf{i}} \right) \tag{A.42e}$$

which upon substitution in Eq. (A.41) will result in the discretized form as,

$$\begin{aligned} J_{\text{x-mom}}^{\text{out}} &= J_{\text{vol}}^{\text{out}} u_1^m + n_x A_f p_{out} + \frac{2 A_f \mu_f n_x}{3} \left[\left(\frac{\partial u}{\partial x} \right) + \left(\frac{\partial v}{\partial y} \right) \right]^{m-1} + \\ & J_{\text{vol}}^{\text{out}} \nabla u_1^{m-1} \cdot \mathbf{r}_1 - A_f \mu_f \nabla u_1^{m-1} \cdot \hat{\mathbf{n}} - A_f \mu_f \nabla \mathbf{U}_1^{m-1} : \left(\hat{\mathbf{n}} \otimes \hat{\mathbf{i}} \right) \end{aligned} \tag{A.43}$$

In the same manner, the discretized form of momentum equation in the y direction for an outflow face can be expressed as:

$$\begin{aligned} J_{\text{y-mom}}^{\text{out}} &= J_{\text{vol}}^{\text{out}} v_1^m + n_y A_f p_{out} + \frac{2 A_f \mu_f n_y}{3} \left[\left(\frac{\partial u}{\partial x} \right) + \left(\frac{\partial v}{\partial y} \right) \right]^{m-1} + \\ & J_{\text{vol}}^{\text{out}} \nabla v_1^{m-1} \cdot \mathbf{r}_1 - A_f \mu_f \nabla v_1^{m-1} \cdot \hat{\mathbf{n}} - A_f \mu_f \nabla \mathbf{U}_1^{m-1} : \left(\hat{\mathbf{n}} \otimes \hat{\mathbf{j}} \right) \end{aligned} \tag{A.44}$$

Symmetry boundary condition

In order to discretize the momentum equation for symmetry boundary faces, the normal/tangential coordinate system is again invoked. The momentum flux in this coordinate

system is written as:

$$J_{\mathrm{n-mom}} = \int_{\mathrm{face}} \left[\left(\rho \tilde{U}_n \right) U_n + \left(p + \frac{2}{3}\mu \nabla \cdot \mathbf{U} \right) - 2\mu \frac{\partial U_n}{\partial n} \right] dA \tag{A.45}$$

$$J_{\mathrm{t-mom}} = \int_{\mathrm{face}} \left[\left(\rho \tilde{U}_n \right) U_t - \mu \left(\frac{\partial U_t}{\partial n} + \frac{\partial U_n}{\partial t} \right) \right] dA \tag{A.46}$$

The advecting velocity $\tilde{U}_n$ across the symmetry face is zero. Also, the shear stress at the symmetry boundary is by definition zero. Therefore, the momentum flux at the symmetry boundary can be written as,

$$\mathbf{J}_{\mathrm{mom}}^{\mathrm{sym}} = J_{\mathrm{n-mom}} \mathbf{n} = \int_{\mathrm{face}} \left(p + \frac{2}{3}\mu \nabla \cdot \mathbf{U} - 2\mu \frac{\partial U_n}{\partial n} \right) \mathbf{n} \, dA \tag{A.47}$$

in which,

$$p|_{\mathrm{face}}^{\mathrm{sym}} = p_1^m + \nabla p_1^{m-1} \cdot \mathbf{r}_1 \tag{A.48a}$$

$$\left. \frac{\partial U_n}{\partial n} \right|_{\mathrm{face}}^{\mathrm{sym}} = \left(n_x \frac{\partial u}{\partial n} + n_y \frac{\partial v}{\partial n} \right) = \frac{u_{\mathrm{sym}} - u_1^m}{s} n_x + \frac{v_{\mathrm{sym}} - v_1^m}{s} n_y \tag{A.48b}$$

$$\left. \frac{\partial U_t}{\partial t} \right|_{\mathrm{face}}^{\mathrm{sym}} = \nabla \mathbf{U}_1^{m-1} : \left(\hat{\mathbf{t}} \otimes \hat{\mathbf{t}} \right) \tag{A.48c}$$

Although the velocity at the symmetry boundary $\mathbf{U}_{\mathrm{sym}}$ is not known, however, by definition it is known that $\mathbf{U}_{\mathrm{sym}} \cdot \hat{\mathbf{n}} = 0$. Therefore, the momentum flux on the boundary face in the x and y directions will read as:

$$\begin{aligned} J_{\mathrm{x-mom}}^{\mathrm{sym}} \;=\; & n_x A_f p_1^m + \frac{4 A_f \mu_f n_x}{3s} \mathbf{U}_1^m \cdot \hat{\mathbf{n}} + n_x A_f \nabla p_1^{m-1} \cdot \mathbf{r}_1 + \\ & \frac{2 A_f \mu_f n_x}{3} \nabla \mathbf{U}_1^{m-1} : \left(\hat{\mathbf{t}} \otimes \hat{\mathbf{t}} \right) \end{aligned} \tag{A.49}$$

$$J^{\text{sym}}_{\text{y-mom}} = n_y A_f p_1^m + \frac{4A_f \mu_f n_y}{3s} \mathbf{U}_1^m \cdot \hat{\mathbf{n}} + n_y A_f \nabla p_1^{m-1} \cdot \mathbf{r}_1 + \frac{2A_f \mu_f n_y}{3} \nabla \mathbf{U}_1^{m-1} : \left(\hat{\mathbf{t}} \otimes \hat{\mathbf{t}}\right) \tag{A.50}$$

A.3 Discretization of the scalar field transport equation

Distribution of scalar fields such as temperature, enthalpy and concentration of different species is governed by general transport equations. The transport of a generic scalar quantity ϕ can generally be written as:

$$\nabla \cdot (\rho \mathbf{U} \phi) = \nabla \cdot (\Gamma_\phi \nabla \phi) + S_\phi \tag{A.51}$$

Integrating the above equation over each control volume and applying the Divergence theorem results in the integral form of the transport equation as:

$$\sum_{\text{faces}} \int_{\text{face}} (\rho \mathbf{U} \phi) \cdot \hat{\mathbf{n}} \, dA - \sum_{\text{faces}} \int_{\text{face}} (\Gamma_\phi \nabla \phi) \cdot \hat{\mathbf{n}} \, dA = \int_{\text{vol}} S_\phi \, dV \tag{A.52}$$

In order to discretize the above equation, the value of dependent variable ϕ and its derivatives should be approximated using the cell values. In the following sections, the discretized form of the transport equation will be presented for interior as well as boundary faces.

A.3.1 Scalar flux across interior faces

A generic interior face and the associated control volumes are shown in Fig. A.1. The scalar flux on each face can be written as:

$$J_{\text{scalar}} = \int_{\text{face}} \left(\rho \tilde{U}_n\right) \phi \, dA - \int_{\text{face}} (\Gamma_\phi \nabla \phi) \cdot \hat{\mathbf{n}} \, dA \tag{A.53}$$

in which,

$$\phi|_{\text{face}}^{\text{int}} = \phi_{\text{up}}^m + \nabla \phi_{\text{up}}^{m-1} \cdot \mathbf{r}_{\text{up}} \tag{A.54a}$$

$$\Gamma_\phi|_{\text{face}}^{\text{int}} = \frac{1}{2} \left(\Gamma_{\phi 1} + \Gamma_{\phi 2}\right)^m + \frac{1}{4} \left(\nabla \Gamma_{\phi 1} + \nabla \Gamma_{\phi 2}\right)^{m-1} \cdot (\mathbf{r}_1 + \mathbf{r}_2) \tag{A.54b}$$

$$\nabla \phi \cdot \hat{\mathbf{n}}|_{\text{face}}^{\text{int}} = \left(\frac{\phi_2 - \phi_1}{s}\right)^m \tag{A.54c}$$

Therefore, the scalar flux can be written in the discretized form as:

$$J_{\text{scalar}}^{\text{int}} = J_{\text{vol}}^{\text{int}} \, \phi_{\text{up}}^m + \frac{A_f \Gamma_{\phi,f}}{s} \left(\phi_1 - \phi_2\right)^m + J_{\text{vol}}^{\text{int}} \left(\nabla \phi_{\text{up}} \cdot \mathbf{r}_{\text{up}}\right)^{m-1} \tag{A.55}$$

A.3.2 Scalar flux across boundary faces

The scalar flux across boundary faces should be discretized depending on the type of boundary condition. In the following subsections, different boundary conditions and their corresponding scalar flux treatments will be discussed.

Constant scalar value

Constant value of scalar quantities is either specified at the inlet or on the wall. This is shown schematically in Fig. A.4.

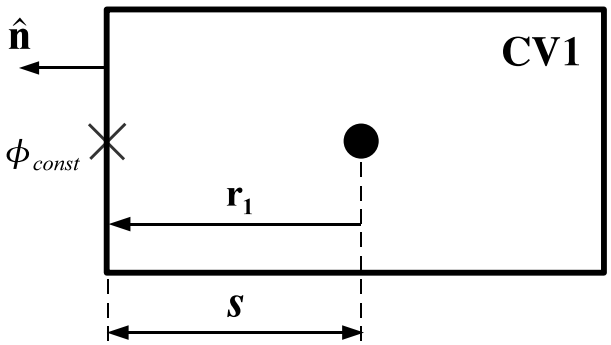

Figure A.4: Schematic of a generic boundary face with constant prescribed scalar value.

At the inlet, the value of the scalar quantity on the face will be equal to the prescribed boundary value. On the other hand, depending on the problem in hand, the value of scalar quantity on the wall boundary face might not be equal to that of physical wall condition due to jump effect (e.g. temperature jump). However, as far as numerical treatment is concerned, a prescribed value can be assumed for these faces, whether or not it is equal to that of the physical wall condition. In this study the prescribed scalar quantity value is denoted by ϕ_{const}. The scalar flux on each face can be written as:

$$J_{\text{scalar}} = \int_{\text{face}} \left(\rho \tilde{U}_n\right) \phi \, dA - \int_{\text{face}} (\Gamma_\phi \nabla \phi) \cdot \hat{\mathbf{n}} \, dA \tag{A.56}$$

in which,

$$\phi|_{\text{face}}^{\text{const}} = \phi_{\text{const}} \tag{A.57a}$$

$$\Gamma_\phi|_{\text{face}}^{\text{const}} = \Gamma_\phi^{\text{const}} \tag{A.57b}$$

$$\nabla\phi \cdot \hat{\mathbf{n}}|_{\text{face}}^{\text{const}} = \frac{\phi_{\text{const}} - \phi_1^m}{s} \tag{A.57c}$$

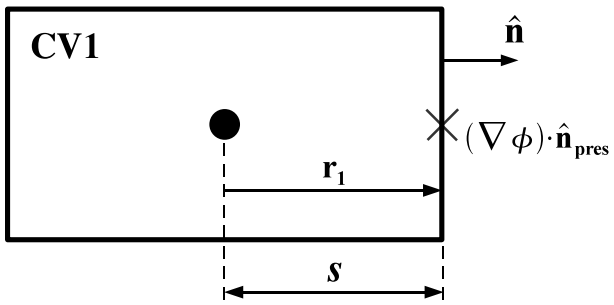

Figure A.5: Schematic of a generic face with prescribed scalar flux.

Therefore, the scalar flux can be written in the discretized form as:

$$J_{\text{scalar}}^{\text{const}} = J_{\text{vol}}^{\text{const}}\,\phi_{\text{const}} + \frac{A_f \Gamma_{\phi,f}}{s}\left(\phi_1 - \phi_{\text{const}}\right)^m \tag{A.58}$$

Prescribed scalar flux

If the flux of scalar quantity is specified on the boundary, the face value can be extrapolated using the prescribed gradient, as depicted in Fig. A.5.

The scalar flux on each face can be written as,

$$J_{\text{scalar}} = \int_{\text{face}} \left(\rho \tilde{U}_n\right) \phi \, dA - \int_{\text{face}} \left(\Gamma_\phi \nabla\phi\right) \cdot \hat{\mathbf{n}} \, dA \tag{A.59}$$

in which,

$$\phi|_{\text{face}}^{\text{pres}} = \phi_1^m + s\left(\nabla\phi \cdot \hat{\text{n}}\right)_{\text{pres}} \tag{A.60a}$$

$$\nabla\phi \cdot \hat{\mathbf{n}}|_{\text{face}}^{\text{pres}} = \left(\nabla\phi \cdot \hat{\text{n}}\right)_{\text{pres}} \tag{A.60b}$$

Therefore, the scalar flux can be written in the discretized form as:

$$J_{\text{scalar}}^{\text{pres}} = J_{\text{vol}}^{\text{pres}}\,\phi_1^m + J_{\text{vol}}^{\text{pres}}\,s\,(\nabla\phi\cdot\hat{\text{n}})_{\text{pres}} - A_f\Gamma_\phi^{m-1}\,(\nabla\phi\cdot\hat{\text{n}})_{\text{pres}} \tag{A.61}$$

References

[1] P. Aghalayam, P-A Bui, and D. G. Vlachos. The role of radical wall quenching in flame stability and the role of radical wall quenching in flame stability and wall heat flux: hydrogen-air mixtures. *Combustion Theory and Modelling*, 2:515–530, 1998.

[2] Jeongmin Ahn, Craig Eastwood, Lars Sitzki, and Paul D. Ronney. Gas-phase and catalytic combustion in heat-recirculating burners. *Proceedings of the Combustion Institute*, 30:2463–2472, 2005.

[3] C. Appel, J. Mantzaras, R. Schaeren, R. Bombach, A. Inauen, B. Kaeppeli, B. Hemmerling, and A. Stampanoni. An experimental and numerical investigation of homogeneous ignition in catalytically stabilized combustion of hydrogen/air mixtures over platinum. *Combustion and Flame*, 128(4):340–368, 2002.

[4] Errol B. Arkilic, Martin A. Schmidt, and Kenneth S. Breuer. Gaseous slip flow in long microchannels. *Journal of Microelectromechanical Systems*, 6(2):167–178, 1997.

[5] F. Behrendt, O. Deutschmann, R. Schmidt, and J. Warnatz. Ignition and extinction of hydrogen–air and methane–air mixtures over platinum and palladium. In *Heterogeneous Hydrocarbon Oxidation*, pages 48–57. ACS Symposium Series, 1996.

[6] Ali Beskok and George Em Karniadakis. Simulation of slip-flows in complex micro-geometries. In *Micromechanical Systems*, volume DSC-40, pages 355–370. ASME, 1992.

[7] Ali Beskok and George Em Karniadakis. Report: A model for flows in channels, pipes, and ducts at micro and nano-scale. *Microscale Thermophysical Engineering*, 3(1):43–77, 1999.

[8] Ali Beskok, George Em Karniadakis, and William Trimmer. Rarefaction and compressibility effects in gas microflows. *Journal of Fluids Engineering*, 118(3):448–456, 1996.

[9] Graem A. Bird. Approach to translational equilibrium in a rigid sphere gas. *Physics of Fluids*, 6:1518, 1963.

[10] Graem A. Bird. *Molecular Gas Dynamics and the Direct Simulation of Gas Flows*. Oxford University Press, New York, 1994.

[11] Robert Byron Bird, Warren E. Stewart, and Edwin N. Lightfoot. *Transport Phenomena*. John Wiley and Sons, New York, second edition, 2002.

[12] G. A. Boyarko, C. J. Sung, and S. J. Schneider. Catalyzed combustion of hydrogen–oxygen in platinum tubes for micro–propulsion applications. *Proceedings of the Combustion Institute*, 30:2481–2488, 2005.

[13] P.-A. Bui, D. G. Vlachos, and P. R. Westmoreland. Homogeneous ignition of hydrogen–air mixtures over platinum. *Symposium (International) on Combustion*, 26:1763–1770, 1996.

[14] Andrea Di Carlo, Alessandro Dell'Era, and Zaccaria Del Prete. 3D simulation of hydrogen production by ammonia decomposition in a catalytic membrane reactor. *International Journal of Hydrogen Energy*, 36:11815–11824, 2011.

[15] Sydney Chapman and T. G. Cowling. *The Mathematical Theory of Non-Uniform Gases*. Cambridge University Press, London, third edition, 1970.

[16] Rei-Yu Chein, Yen-Cho Chen, Chia-San Chang, and J. N. Chung. Numerical modeling of hydrogen production from ammonia decomposition for fuel cell applications. *International Journal of Hydrogen Energy*, 35:589–597, 2010.

[17] A. S. Chellappa, C. M. Fischer, and W. J. Thomson. Ammonia decomposition kinetics over Ni-Pt/Al_2O_3 for PEM fuel cell applications. *Applied Catalysis A: General*, 227:231–240, 2002.

[18] T. V. Choudhary and D. W. Goodman. CO-free fuel processing for fuel cell applications. *Catalysis Today*, 77:65–78, 2002.

[19] T. V. Choudhary, C. Sivadinarayana, and D.W. Goodman. Catalytic ammonia decomposition: COx-free hydrogen production for fuel cell applications. *Catalysis Letters*, 72(3-4):197–201, 2001.

[20] Michael E. Coltrin, Robert J. Kee, and Fran M. Rupley. Surface chemkin: A general formalism and software for analyzing heterogeneous chemical kinetics at gas-solid interfaces. *Int. J. of Chemical Kinetics*, 23(12):1111–1128, 1991.

[21] S. R. Deshmukh, A. B. Mhadeshwar, and D. G. Vlachos. Microreactor modeling for hydrogen production from ammonia decomposition on ruthenium. *Industrial & Engineering Chemistry Research*, 43(12):2986–2999, 2004.

[22] O. Deutschmann, R. Schmidt, and F. Behrendt. Interaction of transport and chemical kinetics in catalytic combustion of H2/O2 mixtures on pt. In *Proceedings of the 8th International Symposium on Transport Phenomena in Combustion*, pages 166–175, 1996.

[23] O. Deutschmann, R. Schmidt, F. Behrendt, and J. Warnatz. Numerical modeling of catalytic ignition. In *Twenty-Sixth Symposium (International) on Combustion/The Combustion Institute*, pages 1747–1754, 1996.

[24] URS Dogwiler, Peter Benz, and John Mantzaras. Two-dimensional modelling for catalytically stabilized combustion of a lean methane-air mixture with elementary homogeneous and heterogeneous two-dimensional modelling for catalytically stabilized combustion of a lean methane–air mixture with elementary homogeneous and heterogeneous chemical reactions. *Combustion and Flame*, 116:243–258, 1999.

[25] W. A. Ebert and E. M. Sparrow. Slip flow in rectangular and annular ducts. *Journal of Basic Engineering, Transactions of ASME*, pages 1018–1024, 1965.

[26] A. Carlos Fernandez-Pello. Micropower generation using combustion: Issues and approaches. *Proceedings of the Combustion Institute*, 29:883–899, 2002.

[27] Joel H. Ferziger and H. G. Kaper. *Mathematical Theory of Transport Processes in Gases*. North Holland Publication Co., Amsterdam-London, 1972.

[28] Jason C. Ganley, E. G. Seebauer, and Richard I. Masel. Development of a microreactor for the production of hydrogen from ammonia. *Journal of Power Sources*, 137(1):53–61, 2004.

[29] Jason C. Ganley, E. G. Seebauer, and Richard I. Masel. Porous anodic alumina microreactors for production of hydrogen from ammonia. *AIChE Journal*, 50(4):829–834, 2004.

[30] Jason C. Ganley, F. S. Thomas, E. G. Seebauer, and Richard I. Masel. A priori catalytic activity correlations: the difficult case of hydrogen production from ammonia. *Catalysis Letters*, 96(3-4):117–122, 2004.

[31] Yohannes Ghermay, John Mantzaras, and Rolf Bombach. Effects of hydrogen preconversion on the homogeneous ignition of fuel-lean $H_2/O_2/N_2/CO_2$ mixtures over platinum at moderate pressures. *Combustion and Flame*, 157:1942–1958, 2010.

[32] Yohannes Ghermay, John Mantzaras, Rolf Bombach, and K. Boulouchos. Homogeneous combustion of fuel lean $H_2/O_2/N_2$ mixtures over platinum at elevated pressures and preheats. *Combustion and Flame*, 158:1491–1506, 2011.

[33] Lotfollah Ghodoossi and Nilüfer Eğrican. Prediction of heat transfer characteristics in rectangular microchannels for slip flow regime and H1 boundary condition. *International Journal of Thermal Sciences*, 44(6):513–520, 2005.

[34] O. Gorke, P. Pfeifer, and K. Schubert. Controlled hydrogen oxidation in a microstructured mixer-reactor module. *Chemical Engineering & Technology*, 30(3):363–369, 2007.

[35] Harold Grad. On the kinetic theory of rarefied gases. *Communications on Pure and Applied Mathematics*, 2(4):331–407, 1949.

[36] John C. Harley, Yufeng Huang, Haim H. Bau, and Jay N. Zemel. Gas flow in microchannels. *Journal of Fluid Mechanics*, 284:257–274, 1995.

[37] B. Hellsing, B. Kasemo, S. Ljungstrom, A. Rosen, and T. Wahnstrom. Kinetic model and experimental results for h2o and oh production rates on pt. *Surface Science*, 189-190(2):851–860, 1987.

[38] B. Hellsing, B. Kasemoa, and V. P. Zhdanov. Kinetics of the hydrogen–oxygen reaction on platinum. *Journal of Catalysis*, 132(1):210–228, 1991.

[39] H. D. Madhawa Hettiarachchi, Mihajlo Golubovic, William M. Worek, and W.J. Minkowycz. Three-dimensional laminar slip-flow and heat transfer in a rectangular microchannel with constant wall temperature. *International Journal of Heat and Mass Transfer*, 51(21-22):5088–5096, 2008.

[40] A. C. Hindmarsh, P. N. Brown, K. E. Grant, S. L. Lee, R. Serban, D. E. Shumaker, and C. S. Woodward. SUNDIALS: Suite of nonlinear and differential/algebraic equation solvers. *ACM Transactions on Mathematical Software*, 31(3):363–396, 2005.

[41] Joseph O. Hirschfelder, Charles F. Curtiss, and R. Byron Bird. *Molecular Theory of Gases and Liquids*. John Wiley and Sons, New York, 1954.

[42] Shou-Shing Hsieh, Huang-Hsiu Tsai, Chih-Yi Lin, Ching-Feng Huang, and Cheng-Ming Chien. Gas flow in a long microchannel. *International Journal of Heat and Mass Transfer*, 47(17-18):3877–3887, 2004.

[43] Jinsong Hua, Meng Wu, and Kurichi Kumar. Numerical simulation of the combustion of hydrogen–air mixture in micro-scaled chambers. part I: Fundamental study. *Chemical Engineering Science*, 60:3497–3506, 2005.

[44] Afzal Husain and Kwang-Yong Kim. Optimization of a microchannel heat sink with temperature dependent fluid properties. *Applied Thermal Engineering*, 28(8-9):1101–1107, 2008.

[45] Symeon Karagiannidis, John Mantzaras, Gregory Jackson, and Konstantinos Boulouchos. Hetero-/homogeneous combustion and stability maps in methane-fueled catalytic microreactors. *Proceedings of the Combustion Institute*, 31:3309–3317, 2007.

[46] G. Karniadakis and A. Beskok. *Micro Flows: Fundamentals and Simulations*. Springer, New York, 2002.

[47] R. J. Kee, G. Dixon-Lewis, J. Warnatz, M. E. Coltrin, and J. A. Miller. A fortran computer package for the evaluation of gas-phase multicomponent transport properties. Technical Report SAND87-8246, Sandia, 1986.

[48] Robert J. Kee, Michael E. Coltrin, and Peter Glarborg. *Chemically Reacting Flow: Theory and Practice*. John Wiley and Sons, 2003.

[49] Earle H. Kennard. *Kinetic Theory of Gases*. McGraw-Hill, New York, 1938.

[50] N. I. Kim, S. Aizumi, T. Yokomori, S. Kato, T. Fujimori, and K. Maruta. Development and scale effects of small swiss-roll combustors. *Proceedings of the Combustion Institute*, 31:3243–3250, 2007.

[51] H. A. Kramers and J. Kistemaker. On the slip of a diffusing gas mixture along a wall. *Physica X*, 8:699–713, 1943.

[52] Lütfullah Kuddusi. Prediction of temperature distribution and nusselt number in rectangular microchannels at wall slip condition for all versions of constant wall temperature. *International Journal of Thermal Sciences*, 46(10):998–1010, 2007.

[53] Lütfullah Kuddusi and Edvin Çetegen. Prediction of temperature distribution and nusselt number in rectangular microchannels at wall slip condition for all versions

of constant heat flux. *International Journal of Heat and Fluid Flow*, 28(4):777–786, 2007.

[54] A. Kumar and S. Mazumder. Assessment of various diffusion models for the prediction of heterogeneous combustion in monolith tubes. *Computers & Chemical Engineering*, 32(7):1482–1493, 2008.

[55] T. T. Leach, C. P. Cadou, and G. S. Jackson. Effect of structural conduction and heat loss on combustion in micro-channels. *Combustion Theory and Modelling*, 10(1):85–103, 2006.

[56] J. Li, S. K. Choua, Z. W. Li, and W. M. Yang. A comparative study of H_2–air premixed flame in micro combustors with different physical and boundary conditions. *Combustion Theory and Modelling*, 12(2):325–347, 2008.

[57] J. Li, S. K. Choua, W. M. Yanga, and Z. W. Li. A numerical study on premixed micro-combustion of CH_4–air mixture: Effects of combustor size, geometry and boundary conditions on flame temperature. *Chemical Engineering Journal*, 150:213–222, 2009.

[58] J. T. Liu, X. F. Peng, and B. X. Wang. Variable-property effect on liquid flow and heat transfer in microchannels. *Chemical Engineering Journal*, 141(1-3):346–353, 2008.

[59] U. Maas and J. Warnatz. Ignition processes in hydrogen-oxygen mixtures. *Combustion and Flame*, 74:53–69, 1998.

[60] K. Maruta, K. Takeda, J. Ahn, K. Borer, L. Sitzki, P. D. Ronney, and O. Deutschmann. Extinction limits of catalytic combustion in microchannels. *Proceedings of the Combustion Institute*, 29:957–963, 2002.

[61] Kaoru Maruta. Micro and mesoscale combustion. *Proceedings of the Combustion Institute*, 33:125–150, 2011.

[62] S. Mazumder and S. A. Lowry. The treatment of reacting surfaces for finite-volume schemes on unstructured meshes. *J. of Computational Physics*, 173(2):512–526, 2001.

[63] C. D. Meinhart, S. T. Wereley, and J. G. Santiago. PIV measurements of a microchannel flow. *Experiments in Fluids*, 27(5):414–419, 1999.

[64] A. B. Mhadeshwar, J. R. Kitchin, M. A. Barteau, and D. G. Vlachos. The role of adsorbate–adsorbate interactions in the rate controlling step and the most abundant reaction intermediate of NH_3 decomposition on Ru. *Catalysis Letters*, 96(1-2):13–22, 2004.

[65] C. Miesse, R. I. Masel, M. Short, and M. A. Shannon. Experimental observations of methane–oxygen diffusion flame structure in a sub-millimetre microburner. *Combustion Theory and Modelling*, 9:77–92, 2005.

[66] Craig M. Miesse and Richard I. Masel. Submillimeter-scale combustion. *AIChE Journal*, 50(12):3206–3214, 2004.

[67] G. L. Morini and M. Spiga. Slip flow in rectangular microtubes. *Microscale Thermophysical Engineering*, 2(4):273–282, 1998.

[68] Gian Luca Morini. Single-phase convective heat transfer in microchannels: a review of experimental results. *International Journal of Thermal Sciences*, 43(7):631–651, 2004.

[69] Gian Luca Morini, M. Spiga, and P. Tartarini. The rarefaction effect on the friction factor of gas flow in microchannels. *Superlattices and Microstructures*, 35(3-6):587–599, 2004.

[70] Hamid Niazmand, Metin Renksizbulut, and Ehsan Saeedi. Developing slip-flow and heat transfer in trapezoidal microchannels. *International Journal of Heat and Mass Transfer*, 51(25-26):6126–6135, 2008.

[71] C. Nonino, S. Del Giudice, and S. Savino. Temperature dependent viscosity effects on laminar forced convection in the entrance region of straight ducts. *International Journal of Heat and Mass Transfer*, 49(23-24):4469–4481, 2006.

[72] C. Nonino, S. Del Giudice, and S. Savino. Temperature-dependent viscosity and viscous dissipation effects in simultaneously developing flows in microchannels with convective boundary conditions. *Journal of Heat Transfer*, 129(9):1187–1194, 2007.

[73] D. G. Norton and D. G. Vlachos. Combustion characteristics and flame stability at the microscale: A CFD study of premixed methane/air mixtures. *Chemical Engineering Science*, 58:4871–4882, 2003.

[74] D. G. Norton and D. G. Vlachos. Hydrogen assisted self-ignition of propane/air mixtures in catalytic microburners. *Proceedings of the Combustion Institute*, 30:2473–2480, 2003.

[75] D. G. Norton, E. D. Wetzel, and D. G. Vlachos. Fabrication of single-channel catalytic microburners: Effect of confinement on the oxidation of hydrogen/air mixtures. *Industrial & Engineering Chemistry Research*, 43:4833–4840, 2004.

[76] D. H. Papadopoulos and D. E. Rosner. Direct simulation of concentration creep in a binary gas-filled enclosure. *Physics of Fluids*, 8:3179–3193, 1996.

[77] George Papapolymerou and Vasilis Bontozoglou. Decomposition of NH3 on Pd and Ir comparison with Pt and Rh. *Journal of Molecular Catalysis A: Chemical*, 120(1-3):165–171, 1997.

[78] A. Irani Rahaghi, M. Said Saidi, M. Hassan Saidi, and M. B. Shafii. Two-dimensional numerical investigation of a micro combustor. *Scientia Iranica Transaction B: Mechanical Engineering*, 17(6):433–442, 2010.

[79] S. Raimondeau, D. G. Norton, D. G. Vlachos, and R. I. Masel. Modelling of high–temperature microburners. *Proceedings of the Combustion Institute*, 29:901–907, 2002.

[80] Robert C. Reid, John M. Prausnitz, and Thomas K. Sherwood. *The properties of Gases and Liquids*. McGraw-Hill, New York, third edition, 1977.

[81] Metin Renksizbulut, Hamid Niazmanda, and G Tercan. Slip-flow and heat transfer in rectangular microchannels with constant wall temperature. *Int. J. Therm. Sci.*, 45(9):870–881, 2006.

[82] M. C. Rhie and W. L. Chow. Numerical study of the turbulent flow past an airfoil with trailing edge separation. *AIAA Journal*, 21(11):1525–1532, 1983.

[83] M. Rinnemo, O. Deutschmann, F. Behrendt, and B. Kasemo. Experimental and numerical investigation of the catalytic ignition of mixtures of hydrogen and oxygen on platinum. *Combustion and Flame*, 111:312–326, 1997.

[84] Ali Rostami, Nader Saniei, and Arun Mujumdar. Liquid flow and heat transfer in microchannels: a review. *International Journal of Heat and Technology*, 18(2):59–68, 2001.

[85] N. Shankar and N. Glumac. Experimental investigations into the effect of temperature slip on catalytic combustion. Penn State University, 2003. Eastern States Section Meeting of the Combustion Institute.

[86] Ching Shen. *Rarefied Gas Dynamics*. Springer, Berlin, 2005.

[87] V. P. Shidlovskiy. *Introduction to Dynamics of Rarefied Gases*. Elsevier, New York, 1967.

[88] Rasmus Zink Sørensen, Lærke J. E. Nielsen, Søren Jensen, Ole Hansen, Tue Johannessen, Ulrich Quaade, and Claus Hviid Christensen. Catalytic ammonia decomposition: miniaturized production of CO_x–free hydrogen for fuel cells. *Catalysis Communications*, 6:229–232, 2005.

[89] C. M. Spadaccini, X. Zhang, C. P. Cadou, N. Miki, and I. A. Waitz. Development of a catalytic silicon micro-combustor for hydrocarbon-fueled power mems. *Proceedings of the IEEE Micro Electro Mechanical Proceedings of the IEEE Micro Electro Mechanical Systems (MEMS)*, pages 228–231, 2002.

[90] Kenneth Sutton and Peter A. Gnoffo. Multi-component diffusion with application to computational aerothermodynamics. In *7th AIAA/ASME Joint Thermophysics and Heat Transfer Conference*, 1998.

[91] W. Tsai and W. H. Weinberg. Steady-state decomposition of ammonia on the Ru(001) surface. *Journal of Physical Chemistry*, 91:5302–5307, 1987.

[92] Stephen E. Turner, Lok C. Lam, Mohammad Faghri, and Otto J. Gregory. Experimental investigation of gas flow in microchannels. *Journal of Heat Transfer*, 126(5):753–763, 2004.

[93] Francisco A. Uribe, Shimshon Gottesfeld, and Thomas A. Zawodzinski. Effect of ammonia as potential fuel impurity on proton exchange membrane fuel cell performance. *Journal of The Electrochemical Society*, 149(3):A293–A296, 2002.

[94] J. van Rij, Timothy A. Ameel, and T. Harman. The effect of viscous dissipation and rarefaction on rectangular microchannel convective heat transfer. *International Journal of Thermal Sciences*, 48:271–281, 2009.

[95] J. van Rij, Timothy A. Ameel, and T. Harman. An evaluation of secondary effects on microchannel frictional and convective heat transfer characteristics. *International Journal of Heat and Mass Transfer*, 52(11-12):2792–2801, 2009.

[96] G Veser, G. Friedrich, M. Freygang, and R. Zengerle. A micro reaction tool for heterogeneous catalytic gas phase reactions. In *Twelfth IEEE International Conference on Micro Electro Mechanical Systems*, pages 394 – 399, Orlando, FL , USA, 1999.

[97] Götz Veser. Experimental and theoretical investigation of H2 oxidation in a high–temperature catalytic microreactor. *Chemical Engineering Science*, 56(4):1265–1273, 2001.

[98] D. G. Vlachos, L. D. Schmidt, and R. Aris. Ignition and extinction of flames near surfaces: Combustion of H2 in air. *Combustion and Flame*, 95(3):313–335, 1993.

[99] Miaomiao Wang, Jianfeng Li, Li Chen, and Yong Lu. Miniature NH_3 cracker based on microfibrous entrapped Ni-CeO_2/Al_2O_3 catalyst monolith for portable fuel cell power supplies. *International Journal of Hydrogen Energy*, 34(4):1710–1716, 2009.

[100] W. Wangard, D. S. Dandy, and B. Miller. A numerically stable method for integration of the multicomponent species diffusion equations. *J. of Computational Physics*, 174(1):460–472, 2001.

[101] J. Warnatz, M. A. Allendorf, R. J. Kee, and M. E. Coltrin. A model of elementary chemistry and fluid mechanics in the combustion of hydrogen on platinum surfaces. *Combustion and Flame*, 96:393–406, 1994.

[102] Bo Xu and Yiguang Ju. Concentration slip and its impact on heterogeneous combustion in a micro-scale chemical reactor. *Chemical Engineering Science*, 60:3561–3572, 2005.

[103] Bo Xu and Yiguang Ju. Theoretical and numerical studies of non-equilibrium slip effects on a catalytic surface. *Combustion Theory and Modeling*, 10(6):961–979, 2006.

[104] S. F. Yin, B. Q. Xu, X. P. Zhou, and C. T. Au. A mini-review on ammonia decomposition catalysts for on-site generation of hydrogen for fuel cell applications. *Applied Catalysis A: General*, 277:1–9, 2004.

[105] Shiping Yu and Timothy A. Ameel. Slip-flow heat transfer in rectangular microchannels. *International Journal of Heat and Mass Transfer*, 44(22):4225–4234, 2001.

[106] Azad Qazi Zade, Amir Ahmadzadegan, and Metin Renksizbulut. A detailed comparison between Navier–Stokes and DSMC simulations of multicomponent gaseous flow in microchannels. *International Journal of Heat and Mass Transfer*, Accepted.

[107] Azad Qazi Zade, Metin Renksizbulut, and Jacob Friedman. Slip/jump boundary conditions for rarefied reacting/non-reacting multi-component gaseous flows. *Int. J. of Heat and Mass Transfer*, 51(21-22):5063–5071, 2008.

[108] Azad Qazi Zade, Metin Renksizbulut, and Jacob Friedman. Heat transfer characteristics of developing gaseous slip-flow in rectangular microchannels with variable physical properties. *International Journal of Heat and Fluid Flow*, 32:117–127, 2011.

[109] Azad Qazi Zade, Metin Renksizbulut, and Jacob Friedman. Contribution of homogeneous reactions to hydrogen oxidation in catalytic microchannels. *Combustion and Flame*, 159(2):784–792, 2012.

[110] Azad Qazi Zade, Metin Renksizbulut, and Jacob Friedman. Rarefaction effects on the catalytic oxidation of hydrogen in microchannels. *Chemical Engineering Journal*, 181-182:643–654, 2012.